

The Herschel Virgo Cluster Survey XII: FIR properties of optically-selected Virgo Cluster galaxies

R. Auld¹, S. Bianchi², M. W. L. Smith¹, J. I. Davies¹, G. J. Bendo⁴,
S. di Serego Alighieri², L. Cortese⁵, M. Baes³, D. J. Bomans¹³, M. Boquien⁷, A. Boselli⁷,
L. Ciesla⁷, M. Clemens⁹, E. Corbelli², I. De Looze³, J. Fritz³, G. Gavazzi⁸,
C. Pappalardo², M. Grossi⁶, L. K. Hunt², S. Madden¹⁰, L. Magrini², M. Pohlen¹,
J. Verstappen³, C. Vlahakis^{11,12}, E. M. Xilouris¹⁴, S. Zibetti²

¹*School of Physics and Astronomy, Cardiff University, The Parade, Cardiff, CF24 3AA, UK.*

²*INAF-Osservatorio Astrofisico di Arcetri, Largo Enrico Fermi 5, 50125 Firenze, Italy.*

³*Sterrenkundig Observatorium, Universiteit Gent, Krijgslaan 281 S9, B-9000 Gent, Belgium.*

⁴*UK ALMA Regional Centre Node, Jodrell Bank Centre for Astrophysics, School of Physics and Astronomy, University of Manchester, Oxford Road, Manchester M13 9PL, UK.*

⁵*European Southern Observatory, Karl-Schwarzschild Str. 2, 85748 Garching bei Muenchen, Germany.*

⁶*CAAUL, Observatório Astronómico de Lisboa, Universidade de Lisboa, Tapada da Ajuda, 1349-018, Lisboa, Portugal.*

⁷*Laboratoire d'Astrophysique de Marseille - LAM, Université d'Aix-Marseille & CNRS, UMR7326, 38 rue F. Joliot-Curie, 13388 Marseille Cedex 13, France*

⁸*Universita' di Milano-Bicocca, piazza della Scienza 3, 20100, Milano, Italy.*

⁹*INAF-Osservatorio Astronomico di Padova, Vicolo dell'Osservatorio 5, 35122 Padova, Italy.*

¹⁰*Laboratoire AIM, CEA/DSM- CNRS - Université Paris Diderot, Irfu/Service, Paris, France.*

¹¹*Joint ALMA Observatory, Alonso de Cordova 3107, Vitacura, Santiago, Chile*

¹²*European Southern Observatory, Alonso de Cordova 3107, Vitacura, Casilla 19001, Santiago 19, Chile*

¹³*Astronomical Institute, Ruhr-University Bochum, Universitaetsstr. 150, 44780 Bochum, Germany.*

¹⁴*Institute of Astronomy and Astrophysics, National Observatory of Athens, I. Metaxas and Vas. Pavlou, P. Penteli, GR-15236 Athens, Greece.*

¹⁵*Max-Planck-Institut fuer Astronomie, Koenigstuhl 17, D-69117 Heidelberg, Germany.*

Submitted to MNRAS 2012 February 14

ABSTRACT

The Herschel Virgo Cluster Survey (HeViCS) is the deepest, confusion-limited survey of the Virgo Cluster at far-infrared (FIR) wavelengths. The entire survey at full depth covers ~ 55 sq. deg. in 5 bands (100–500 μm), encompassing the areas around the central dominant elliptical galaxies (M87, M86 & M49) and extends as far as the NW cloud, the W cloud and the Southern extension. The survey extends beyond this region with lower sensitivity so that the total area covered is 84 sq. deg. In this paper we describe the data, the data acquisition techniques and present the detection rates of the optically selected Virgo Cluster Catalogue (VCC). We detect 254 (34%) of 750 VCC galaxies found within the survey boundary in at least one band and 171 galaxies are detected in all five bands. For the remainder of the galaxies we have measured strict upper limits for their FIR emission. The population of detected galaxies contains early- as well as late-types although the latter dominate the detection statistics. We have modelled 168 galaxies, showing no evidence of a strong synchrotron component in their FIR spectra, using a single-temperature modified blackbody spectrum with a fixed emissivity index ($\beta = 2$). A study of the χ^2 distribution indicates that this model is not appropriate in all cases, and this is supported by the FIR colours which indicate a spread in $\beta=1-2$. Statistical comparison of the dust mass and temperature distributions from 140 galaxies with $\chi^2_{\text{dof}=3} < 7.8$ (95% confidence level) shows that late-types have typically colder, more massive dust reservoirs; the early-type dust masses have a mean of $\log(\langle M \rangle / M_{\odot}) = 6.3 \pm 0.3$, while for late-types $\log(\langle M \rangle / M_{\odot}) = 7.1 \pm 0.1$. The late-type dust temperatures have a mean of $\langle T \rangle = 19.4 \pm 0.2$ K, while for the early-types, $\langle T \rangle = 21.1 \pm 0.8$ K. Late-type galaxies in the cluster exhibit slightly lower dust masses than those in the field, but the cluster environment seems to have little effect on the bulk dust properties of early-types. In future papers we will focus more on the scientific analysis of the catalogue (e.g. measuring FIR luminosity functions, dust mass functions and resolved gas and dust properties).

1 INTRODUCTION

Of the major galaxy overdensities in the nearby Universe (Virgo, Fornax, Abell 1367, Ursa Major and Coma) the Virgo Cluster remains the most widely studied. Its proximity (17 Mpc, Gavazzi et al. 1999) allows us both to probe the cluster population down to faint levels and to resolve the larger galaxies with modest instruments.

In contrast to other, more relaxed clusters, Virgo exhibits a relatively high fraction of gas-bearing galaxies. As the galaxies surrounding Virgo fall into the cluster they are subject to many interactions. Interactions with the cluster gravitational potential (Merritt 1984, Boselli & Gavazzi 2006), the hot intracluster medium (Gunn & Gott 1972, Abadi et al. 1999) and, in some cases, each other (Moore et al. 1996, Mihos 2004) are among the dominant processes affecting evolution in the cluster. They are believed to be responsible for transforming galaxies from gas-bearing, star-forming late-types into the dormant early-type galaxies that dominate the cluster core, but the details of these processes are still poorly understood.

Evidence of these interactions can be seen in the disturbed morphologies of the galaxies themselves (e.g. NGC 4438, Oosterloo & van Gorkom 2005, Vollmer et al. 2001) or in the intracluster medium (ICM), where streams such as those observed in the optical (Mihos et al. 2005) and 21cm (Gavazzi et al. 2008) show that the space between galaxies is littered with stellar and gaseous material. The other major ISM constituent, dust, is also expected to carry the signatures of these interactions. Understanding what happens to the dust component in the cluster environment is another important aspect of environmental effects on galaxy evolution, but requires a large dataset of galaxies in different environments.

Dust emission dominates the mid infrared (MIR, 1-10 μm) to far infrared and sub-mm (FIR, 10-500 μm ; sub-mm, 500-1000 μm) portion of a galaxy's spectral energy distribution (SED). In the MIR, it is a complicated mixture of thermal emission from stars and warm ($T \sim 30$ K) dust, and line emission from molecular species. The FIR and sub-mm regime, however, is dominated by thermal emission from interstellar dust grains. Studying galaxies at these wavelengths has been problematic since ground-based observations are compromised by high attenuation and bright spectral line emission from the Earth's atmosphere.

Space missions such as *IRAS*, *ISO* and most recently *Spitzer*, have been vital for expanding our understanding of interstellar dust. *IRAS* and *Spitzer* were sensitive to the warm dust (> 30 K) within dust-bearing galaxies (e.g. Devereux & Young (1990), Kennicutt et al. 2003), while *ISO* and the ground-based SCUBA allowed astronomers to probe the coldest dust within galaxies (e.g. Popescu et al. 2002, Tuffs et al. 2002, Alton et al. 1998, Dunne & Eales 2001, Dunne & Eales 2002). Unfortunately these pioneering instruments were limited in their resolution and sensitivity, and these early studies were confined to individually targeted galaxies.

The **Herschel Virgo Cluster Survey** (HeViCS, Davies et al. 2010) has observed 84 sq. deg. of the Virgo cluster with the primary goal of studying cold-dust bearing galaxies in the cluster environment. The 3.5m primary mirror of the Herschel Space Observatory, combined with the

ability to perform 5-band photometry simultaneously over a wavelength range of 100–500 μm , afford the survey unprecedented sensitivity and resolution in the FIR regime. This has enabled us to conduct the most detailed studies to-date of cold (< 30 K) dust in Virgo cluster galaxies.

In previous work, based on shallow data from the central $4^\circ \times 4^\circ$ region, we have already analysed the FIR luminosity function in the cluster core (Davies et al. 2010), studied truncated dust disks in cluster galaxies (Cortese et al. 2010), put upper limits on the dust lifetime in early-type galaxies (Clemens et al. 2010), probed the distribution of dust mass and temperature within cluster spirals (Smith et al. 2010), identified an excess at 500 μm for a sample of metal-poor, star-forming dwarfs (Grossi et al. 2010), studied non-thermal FIR emission from the dominant cluster elliptical galaxy, M87 (Baes et al. 2010), detected dust in cluster dwarf elliptical galaxies (de Looze et al. 2010).

In more recent work, based on the full survey area but limited in depth, we have presented an analysis of the brightest galaxies at 500 μm (BGS, Davies et al. 2012). We have examined the metallicity dependence of the molecular gas conversion factor, X_{CO} (Magrini et al. 2011), and probed the effect of interactions on the distribution of dust and gas in a sample of late-types (Corbelli et al. 2012; Pappalardo et al. 2012),

In this, the first paper to exploit the full dataset, we present the FIR properties of a statistically complete, optically-selected sample; the Virgo Cluster Catalogue (VCC, Binggeli et al. 1985). We concentrate on the description of the data, the data reduction, the flux measurements themselves and the recovery rates of the VCC galaxies. This will pave the way for future papers which will focus on the science that can be extracted from the data (FIR/sub-mm colour relations, luminosity functions, dust mass functions, radial/resolved FIR properties etc.).

The VCC is the largest and most reliable catalogue of cluster members; it covers 140 sq. deg. and contains almost 1300 probable cluster galaxies. Membership was based, for most part, on morphological criteria, with redshift information taking precedence as it became available. A comparison of the morphology method with redshift data proved it to be very reliable, with a success rate of over 98% (Binggeli et al. 1985, Binggeli et al. 1993).

While it is true that the cluster has been observed with more sophisticated instruments with superior imaging capabilities compared to the original Las Campanas plates (e.g. Kim et al. 2011, Côté et al. 2004), the power of the catalogue lies in the membership information itself. Applying their optical completeness limit of photographic magnitude, $m_{pg} \leq 18$, yields a population of ~ 1000 galaxies, and has provided the astronomical community with a large, statistically complete sample of Virgo Cluster galaxies. It has been used for nearly 30 years with only minor revision (e.g. Binggeli et al. 1993, Gavazzi et al. 1999) and will only be surpassed by the completion of the Next Generation Virgo Survey (Mei et al. 2010, Ferrarese 2011).

The data for our optical comparisons were taken from the GOLDMINE database (Gavazzi et al. 2003) which includes measurements at multiple wavelengths for the entire, revised VCC. It is our intention to expand the database with our FIR measurements. By augmenting these data with the HeViCS data we aim to provide the community with a

definitive legacy product that will enable the detailed study of stars and dust in the cluster environment.

In section 2 we describe the survey data acquisition, data reduction, the flux extraction method and the SED fitting. In section 3 we present the detection rates and the flux measurements at 100, 160, 250, 350 & 500 μm . In this section we also provide the results of the SED modelling and show the derived dust mass and temperature distributions for a subset of galaxies which were well fit by the single-temperature model. In section 4 we summarise our findings. The tables of fluxes and dust mass/temperature are attached as appendices in Tables B & C. The FIR SED fits are displayed in Appendix D.

2 OBSERVATIONS, DATA REDUCTION AND FLUX MEASUREMENT

2.1 Observations

The HeViCS survey region constitutes four overlapping $4^\circ \times 4^\circ$ tiles (Fig. 1) including the majority of Cloud A, centred on M87 and extending far enough to encompass the NW cloud, the W cloud and the S extension in the nomenclature of de Vaucouleurs (1961). Each tile has been observed by the Herschel PACS (Poglitsch et al. 2010) and SPIRE (Griffin et al. 2010a) instruments operating in fast-parallel mode, allowing PACS and SPIRE photometry to be performed simultaneously at a scan rate of $60''\text{s}^{-1}$. The observing strategy consists of scanning each $4^\circ \times 4^\circ$ tile in two orthogonal directions. This cross-linking allows for the application of data processing techniques that can mitigate the effects of $1/f$ noise. This enables the potential recovery of large scale structure (cirrus/intracluster dust) of up to the length of a tile (4°). This strategy is then repeated until each tile is nominally covered by eight scans, although in overlap regions this can reach as high as sixteen scans.

The PACS footprint is offset from the SPIRE footprint by $20'$, leading to slight mismatch in the area of sky surveyed. To compensate for this effect, the proposed survey target regions are automatically expanded at the observing stage, to reach full coverage with both instruments in the target field. This gives rise to extra data, outside the target region. We retain the extra data and after combining the entire set of cross-linked scans, the total sky coverage is somewhat larger than previously claimed (~ 84 sq. deg. compared to 64 sq. deg.), although the full-depth region is limited to the central 55 sq. deg.

2.2 Data Reduction

The SPIRE photometer (Griffin et al. 2010b) data were processed up to Level 1 (i.e. calibrated bolometer timelines) with a custom made pipeline adapted from the official pipeline¹. The purpose of the pipeline is to remove all instrumental artefacts such as glitches, finite bolometer time response, electronic filtering and thermal drift, as well as applying astrometry and flux calibration.

The main difference between our pipeline and the standard one is that we did not run the default *temperatureDriftCorrection* and the residual, median baseline subtraction. Instead we use a custom method called the *BRIght Galaxy ADaptive Element* (**BriGADE**, Smith et al. 2012, in prep.) to remove the temperature drift. No further baseline subtraction was necessary to bring the bolometer baselines to a common level.

BriGADE uses the information from the thermistors in each array and directly fits the thermistor data to the entire bolometer timeline (including data where the spacecraft was slewing between scans). If both thermistors exhibited instantaneous ‘jumps’ (an artefact where there is a sudden offset in the timelines), these are either corrected or the comparison switched to the slightly less sensitive Dark Pixels of the individual array. This approach is hampered slightly by the presence of bright sources in the bolometer timelines. To suppress their influence, they are automatically removed from the fitting process along with samples affected by other artefacts (‘jumps’ and glitches). When a choice of thermistors is available (i.e. for the 250 & 500 μm arrays), the one providing the best fit is used to subtract a scaled version from the bolometer timelines. This method improves the baseline subtraction significantly, especially in cases where there are large or rapid temperature variations during the observations, which cause large stripes in the final maps (Fig. 2).

The individual scans from all 32 cross-linked observations are combined into a single mosaic using the in-built naïve mapper of HIPE. The full-width half-maximum (FWHM) measurements of the beams in the final maps are $18.2''$, $25.4''$ & $36.0''$ for 250, 350 & 500 μm respectively. The beam areas used in the conversion from Jy beam⁻¹ to Jy were 423, 751 and 1587 arcsec², at 250, 350 & 500 μm respectively. This is in accordance with the SPIRE photometry guidelines². The final maps have pixel sizes of $6''.8''$ & $12''$ at 250, 350 & 500 μm respectively. One of the by-products of the HIPE data processing is a map of the instrumental noise. For the SPIRE bands this gives corresponding instrument-associated noise levels of 4.9, 4.9 & 5.7 mJy beam⁻¹ in the areas uniformly covered by 8 scans. This drops to 3.5, 3.4, & 4.0 mJy beam⁻¹, in the overlapping regions, uniformly covered by 16 scans. The values are consistent with a drop in the noise level proportional to \sqrt{t} where t is the integration time, demonstrating that the contamination by $1/f$ noise is minimal.

Deriving the global noise is not a straightforward task due to the presence of background source crowding and Galactic cirrus emission, which are both position-dependent. We selected a region in the fully-sampled southernmost tile, which had the lowest cirrus contribution. Within this region we measured pixel-pixel fluctuations and applied iterative $3\text{-}\sigma$ clipping to eliminate the contribution from bright sources. This gave noise values of 6.6, 7.3 & 8.0 mJy/beam (250, 350, & 500 μm respectively). By quadratically subtracting the instrumental noise, we derived confusion noise estimates of 4.4, 5.4 & 5.6 mJy/beam (250, 350, & 500 μm respectively). These crude estimates are slightly higher than

¹ See Griffin et al. (2010b) or Dowell et al. (2010) for a more detailed description of the official pipeline and a list of the individual modules.

² http://herschel.esac.esa.int/twiki/pub/Public/SpireCalibrationWeb/beam_release_note_v1-1.pdf

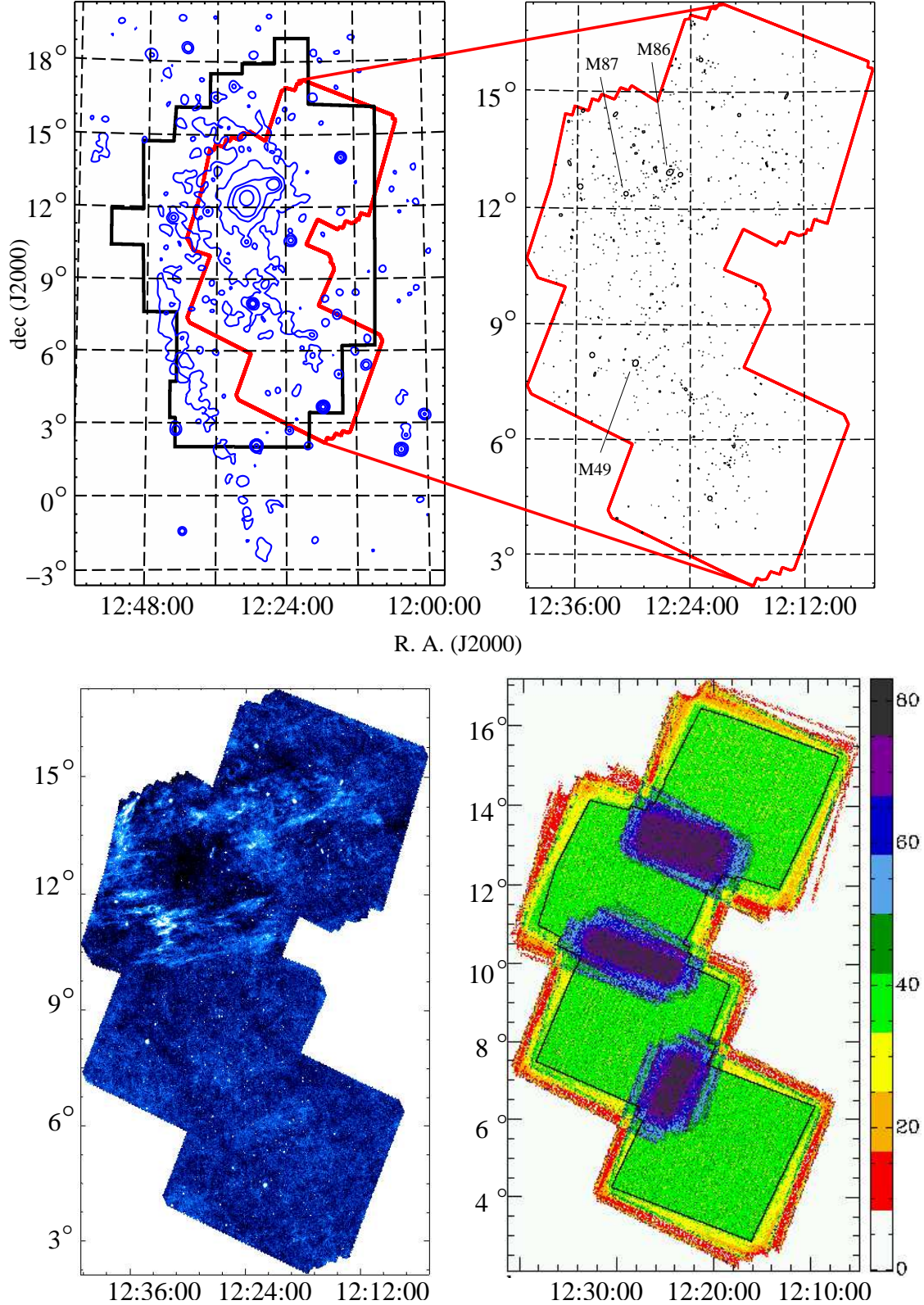


Figure 1. *Top left:* the Virgo Cluster region. X-ray contours from Boehringer et al. are shown in blue. The VCC survey region is outlined in solid black and the full extent of HeViCS is outlined in red. *Top right:* the HeViCS survey region with black ellipses representing the VCC optical discs measured to d_{25} . The dominant cluster galaxies have been labelled and their positions correspond to the peaks in X-ray emission. *Bottom left:* *Herschel-SPIRE* 250μm image of the full survey. Even in this small image it is possible to identify the VCC galaxies with the strongest FIR emission and the large swathes of Galactic dust cirrus. *Bottom right:* Survey depth, measured in samples per pixel, from the 250 μm data. The inner region, covered by 8 scans with *PACS* and *SPIRE*, is shown by the black outline. In the overlap region between tiles the coverage rises to 16 scans.

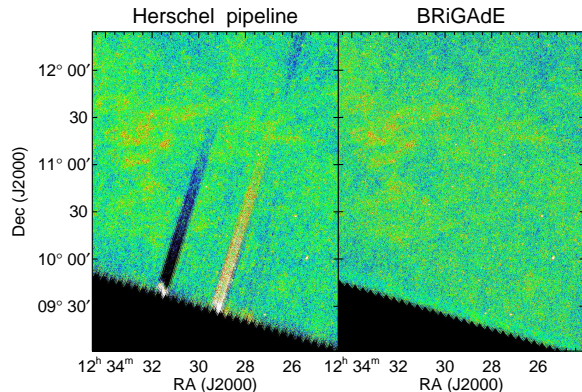


Figure 2. Instantaneous jumps in the thermistor timelines, give rise to striping in the final images, when using the standard Herschel pipeline. Use of the BRiGAdE method greatly reduces their impact.

Nguyen et al. (2010) on the Hermes fields (3.8, 4.6 & 5.2 mJy/beam respectively, employing an analogous iterative $3\text{-}\sigma$ clip), but still within twice their quoted uncertainty. The HeViCS SPIRE maps have similar contributions from confusion and instrumental noise. We repeated the analysis on regions of overlap between the tiles, which have greater coverage and found no significant reduction in the noise level, implying that the maps are close to being dominated by confusion noise.

With regard to the PACS data, we have obtained maps at 100 and 160 μm by exploiting the naive projection task *photProject* in HIPE (v7.3.0), following a similar approach as described by Ibar et al. (2010). Map making was performed in two steps: for each single scan, we first obtained maps using the standard data reduction pipeline, but with the entire VCC galaxies masked out. In these maps, the $1/f$ noise was corrected for by applying a high-pass filter with a length of 20 and 40 frames for the 100 and 160 μm map, respectively, and deglitching was performed by means of the sigma-clipping standard algorithm (*IIndLevelDeglitchTask* task in HIPE, with $\sigma = 3$). These preliminary maps were used to identify and mask bright, extended non-VCC sources, and to fine-tune the deglitching. The masks were then applied to the calibrated timelines using a flux threshold set to 2.5σ , and the minimum number of pixels above the threshold, for a source to be detected, was set to 48 and 24 for the 100 and 160 μm channels, respectively. In order to minimize the high-pass filtering over-subtraction, the masks were enlarged, by adding 4 and 2 pixels to the edges of the detected sources, for 100 and 160 μm maps, respectively.

In a second step, the data were reduced again. This time, the deglitching task was applied before high-pass filtering, with the bright sources being masked to avoid unwanted flux removal from their brightest parts. Then, the masked, deglitched timelines were high-pass filtered, with a filter length of 10 and 20 frames for 100 and 160 μm respectively. At this point the timelines for the eight scans were joined together. After this, the second-level deglitching task was run to remove glitches from the bright sources

and, finally, individual tile maps were produced with the *photProject* task.

Due to the enormous volume of data in a PACS observation, the HIPE map maker is currently only capable of combining 8 cross-scans from an individual tile into a single mosaic. The individual tiles were then combined into mosaics using the *SWarp*³ package.

The PACS beams at 100 and 160 μm are elongated along the scan direction due to onboard averaging of the PACS data. This is a necessary complication due to the limit of the rate at which data can be downloaded from the spacecraft. Averaging together the 8-scan data, taken at different observing angles, results in approximately circular beams. These are Gaussian in shape with FWHM values for the 100 & 160 μm beams of 9.4'' and 13.4'' respectively and the corresponding map pixel sizes are 2'' and 3''. The PACS instrumental error maps from the HIPE pipeline are still in the process of being optimised, so PACS errors were estimated directly from the signal maps, using apertures on blank regions of sky. The standard deviations of the background in the PACS maps are 1.9 and 1.2 mJy pixel⁻¹ for the 160 and 100 μm channels respectively in the areas covered by 8 scans. This decreases to 1.3 and 0.8 mJy pixel⁻¹ in the overlapping regions. This is consistent with a $\sqrt{t_{int}}$ decrease, where t_{int} is the integration time, indicating that the noise in the background in the PACS maps is still dominated by instrumental noise.

2.3 Flux Measurement

Of the 1076 VCC objects with $m_{pg} \leq 18$, 750 fall within the extreme boundary of the HeViCS region. Once these targets were identified, the optical parameters (position, ellipticity, position angle, and optical diameter – d_{25}) were used to overplot the optical disk on the 250 μm image. Position angles for the VCC galaxies were obtained from HyperLEDA. The d_{25} was taken from the original VCC as quoted in GOLDMINE, which has been estimated from the photographic plates. Previous studies (e.g. Pohlen et al. 2010, Cortese et al. 2010) have shown that the optical emission is fairly well traced by the FIR emission, for late-type galaxies without truncated gas-disks. Preliminary comparisons between the optical and FIR emission for HeViCS late-type galaxies revealed that the optical ellipse parameters provided a good basis for defining the FIR apertures for measuring the flux. Early-types tended to exhibit point-like emission in the FIR, and in a few particular cases irregular and extended (e.g. M86) or dominated by synchrotron radiation from the AGN jets (e.g. M87 Baes et al. 2010).

Accurate photometry had to be able to cope with several aspects inherent to the Herschel images. The SPIRE maps are dominated by Galactic cirrus and, to a lesser extent, by unresolved background sources. Some bright sources in the PACS images also suffer from negative bowls which are the result of inaccurate masking of bright sources during the high-pass filtering. Various stages of the measurement process are displayed in Fig. 3. It may aid the reader to refer to this during the description that follows.

To begin with, a 200×200 pixel sub-image centred on

³ <http://www.astromatic.net/software/swarp>

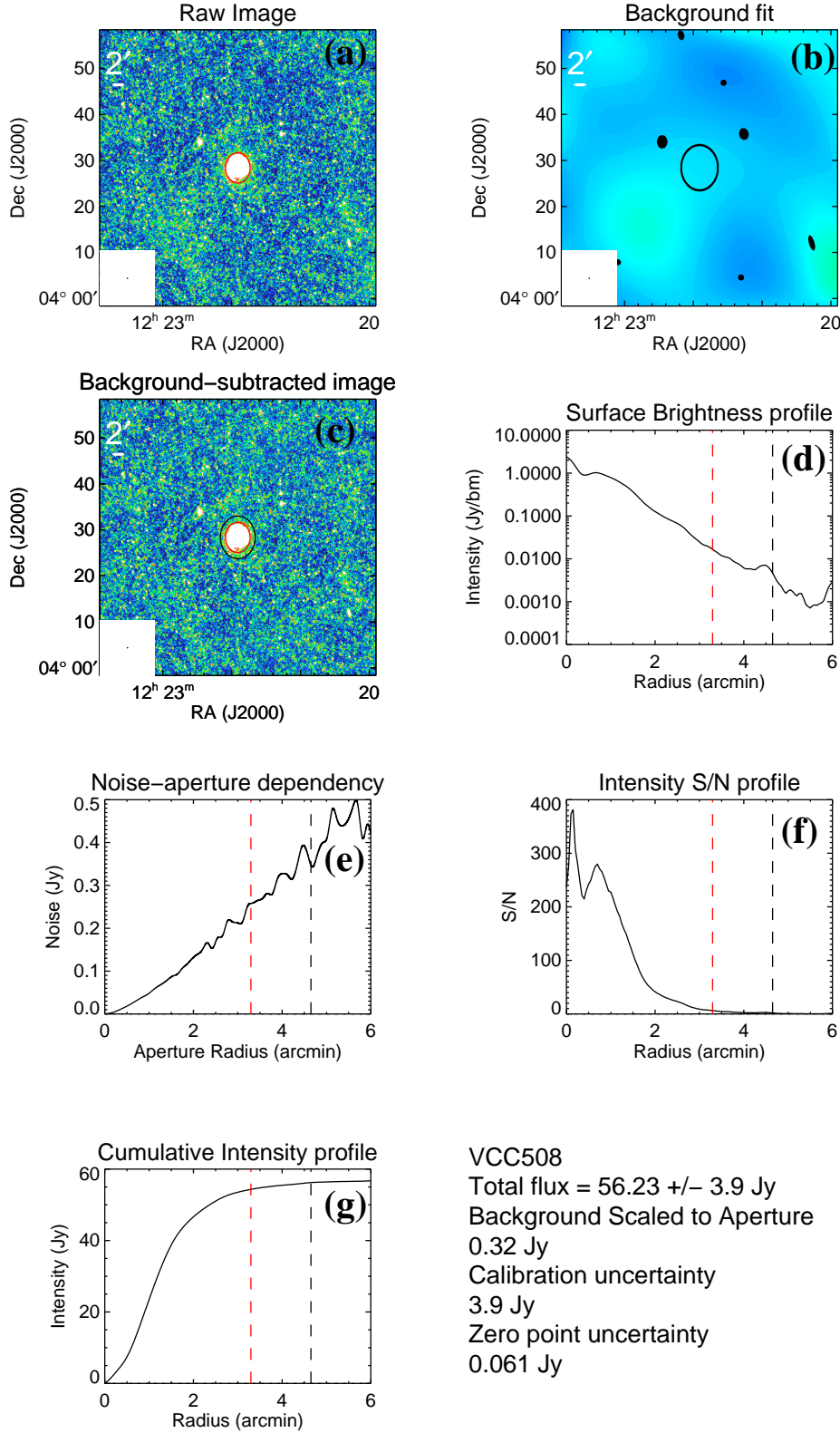


Figure 3. Example products from the fitting process for M61 (VCC508) at 250 μ m. (a) The raw sub-image extracted from the full HeViCS mosaic. The d_{25} limit is outlined in red, the 250 μ m beam is given to scale at the bottom left of the image. (b) The estimate of the background from the masked image. The ellipse is explained in the text. (c) The resultant background-subtracted sub-image on which radial plots and flux measurements are performed. (d) Radial plot of surface brightness. (e) radial dependence of the total noise in a circular aperture. (f), (g) Radial plots of S/N & cumulative intensity respectively. Optical (d_{25}) and FIR limits are indicated by the red and black dashed lines respectively.

each galaxy, was extracted from the full map (Fig. 3a). The galaxy was then masked as are all the nearby Virgo galaxies. The extent of the galaxy was defined by the $1.5 \times d_{25}$ limit. It should be noted that there can be small differences between this d_{25} measurement (estimated from photographic plates) and the equivalent measured from CCD data. The difference is not important to us, however, since the ellipticity and extent are merely used as starting points for the ellipse measuring procedure. To account for edge-on galaxies and those whose optical dimensions were smaller than the beam at any given wavelength, the optical ellipse parameters were convolved with a Gaussian beam profile of the relevant size for each band. In some cases, the optical morphology was unrepresentative of the FIR emission (e.g. for point-like or irregular sources). For bright, point-like sources, circular ellipses were employed and for M86, we used the features identified in Gomez et al. (2010) to define the extent of emission in M86. For cases where the optical extent was too large to elicit a reliable estimate of the background, the sub-image region was increased to 600 pixels for SPIRE and up to 1200 pixels for PACS maps.

The background is a combination of the foreground cirrus, bright background sources and unresolved background sources. For SPIRE images which are highly confused, the estimate of the background was achieved with a 5th order (i.e. terms up to x^5, y^5 plus all cross terms) 2-D polynomial over the entire masked sub-image. We employed the least-squares polynomial fitting IDL routine SFIT to perform the fit. To counteract the influence of bright background galaxies a 95% flux clip was imposed and the remaining pixels used to estimate the background. For PACS images which were dominated by instrumental noise, a 2nd order polynomial was adequate. An example of the background estimate is shown in Fig. 3(b). Once the background estimation was obtained, it was subtracted from the original sub-image (Fig. 3c).

We then created annuli based on the optical ellipse parameters at increasing radii around the optical centre of the galaxy. For each annulus we measured the total flux, the surface brightness, the aperture noise (described in section 2.4.2) and the S/N. The S/N was calculated as the ratio of the total flux within the annulus to the noise in an aperture with the same area as the annulus.

The S/N radial profile was then used to define a cut-off once the S/N dropped below 2. This is then used to define the edge of the galaxy (the black dashed line in Figs. 3(d), (e), (f) & (g)). The final measured uncertainty is then calculated from the quadrature sum of the aperture noise for the entire aperture, the calibration uncertainty and the zero-point error. The new estimate of the galaxy edge is used to create a new mask, replacing the old $1.5 \times d_{25}$ limit, and the process repeated. Once the procedure converged, aperture corrections were applied to the flux and the aperture noise measurements in accordance with Ibar et al. (2010) and Griffin & North (2012, in prep).

If the total aperture S/N measured less than 3, using this method, the sub-image was optimally searched again for a point source. This consisted of convolving each sub-image with the relevant Point Spread Function (PSF) for each band and measuring the peak emission within an area defined by the convolved PSF FWHM, centred on the optical position. To measure the noise in the PSF-convolved

map we plotted the histogram of the flux values and fit the negative flux values with a Gaussian function, whose width is representative of the combined instrumental and confusion noise (Marsden et al. 2009, Chapin et al. 2011 and references therein). In practice this required some tuning, the best results being achieved when fitting a Gaussian to a reduced range of histogram bins that encompassed a significant portion of the negative tail, the peak and a small number of bins on the positive side of the peak. The width of this Gaussian was then taken as our estimate of the noise, and detections were defined as those sources above 3σ . In the case of a detection, the noise from the PSF-convolved map was summed in quadrature with the calibration uncertainty and zero-point uncertainty to provide the total error. If the source was still undetected, the 3σ upper limit was measured from the histogram in the PSF-convolved map.

We recorded all of the radial data and intermediate masks during the process and, they will be publicly available online⁴ in ASCII format as well as *eps* figures outlining the different steps, such as that shown in Fig. 3.

Once the automatic flux measurements were completed each detected galaxy was analysed by-eye to confirm that the masking and cut-off radius were realistic. Optical images from GOLDMINE and the Digital Sky Survey were examined in order to make the most comprehensive judgment for discriminating between background sources and galactic features. We found that occasionally the algorithm could be deceived by nearby, bright background galaxies or by the presence of bright cirrus which was insufficiently modelled and removed. Some were obvious as in the case of VCC778 (Fig. 4); here the FIR emission consists of multiple point sources with optical background galaxies clearly visible near the centre of the emission. Some were more ambiguous as in VCC355 (Fig. 5); while this galaxy does have FIR emission within the optical extent of the galaxy, it is in a highly confused region and there is nothing to distinguish it from the immediate background. For these sorts of detections, human intervention was required to define the radial cut-off manually or to exclude the galaxy from the list of detections. This affected $\sim 10\%$ of the total number of measurements, most of which were false detections. In the event that the galaxy was excluded due to a contaminating source, the measured flux of the contaminating source at the position of the galaxy has been recorded as the upper limit and these sources are labelled with an asterisk in Table B.

Since the 250 μm data has the best combination of sensitivity and resolution, we also imposed a strict requirement that a galaxy be detected at 250 μm . This further restricts the possibility of illegitimate background sources making it into the catalogue.

The FIR emission from the interacting galaxy pair NGC4567/8 (VCC1673/6) is a confused system with overlapping contributions from both galaxies. We have adapted the method described above to model NGC4567 and hence measure the individual fluxes. This method is fully described in Appendix A.

The nominal SPIRE and PACS flux calibration schemes assume a ‘white’ point source, i.e. a compact object whose emission is flat across the filter bandpass (the K4 term). This

⁴ <http://goldmine.mib.infn.it/>

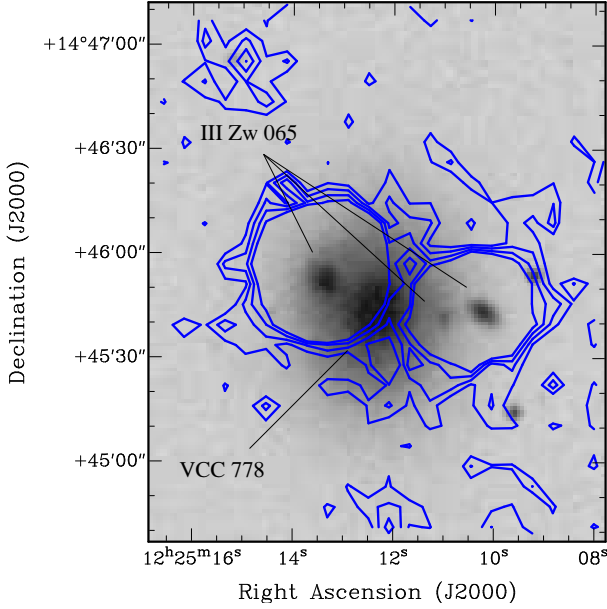


Figure 4. An example of background confusion causing an incorrect detection. A DSS greyscale image overlaid with 250 μm contours at 0.005, 0.01, 0.015, 0.02 Jy beam^{-1} . The target early type galaxy, VCC778 is sandwiched between a background triplet (listed in NED as III Zw 065). Their FIR emission dominate the total flux in this region, hence the emission from VCC778 is not well determined.

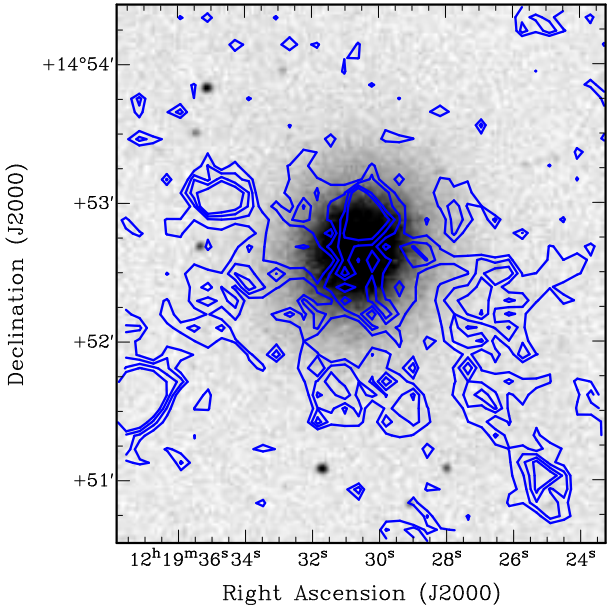


Figure 5. An example of cirrus/background contamination causing an ambiguous detection. A DSS greyscale image overlaid with 250 μm contours at 0.005, 0.01, 0.015, 0.02 Jy beam^{-1} . The optical centre of the target early type galaxy, VCC355, is offset from the peak of the 250 μm emission and the 250 μm emission is in a region of high confusion. Since the emission cannot be associated with the galaxy, it has been excluded from the catalogue.

term varies as a function of the object size and spectral index, and so must be corrected for. The fluxes presented in Table B use the nominal K4 values, allowing the reader to apply the corrections separately as described in the SPIRE Observer's Manual⁵ and the PACS Observer's manual⁶. We leave the application of the correction factors to the reader, since they require prior knowledge of the extent (which can be subjective) and colour of the source. They are also tabulated in Davies et al. (2012) for a $\beta = 2$ modified black-body.

2.4 Total uncertainty estimate

The final uncertainty measurements quoted in Table B consist of contributions from calibration uncertainty, σ_{cal} , aperture uncertainty, σ_{aper} and zero-point uncertainty, σ_{zero} . These contributions are added in quadrature thus:

$$\sigma_{total}^2 = \sigma_{cal}^2 + \sigma_{aper}^2 + \sigma_{zero}^2 \quad (1)$$

We now discuss the derivation of each of the terms in Eq'n 1 before moving on to the verification of the Herschel calibration.

2.4.1 calibration uncertainty

For SPIRE, σ_{cal} is based on scans of a single source (Neptune) and comparing it to a model of Neptune's emission. The final values for each band include a correlated 5% error from the assumed model for Neptune and a 2% random component from repeated measurements. The Observer's manual advises that as a conservative measure, these values should be added together. $SPIRE\sigma_{cal}$ is taken to be 7% for each band.

The situation is more complicated for PACS since the calibration is based on multiple sources with different models. The uncorrelated uncertainties of 3% at 100 μm 4% at 160 μm and a 2.2% correlated uncertainty are given for point sources, which were observed, reduced and analysed in a different way to the HeVICS PACS data. A recent Technical Report⁷ found that PACS 160 μm data agreed with MIPS 160 μm data to within 5-20%, but again, this was using two different map-making schemes to that presented here. We have erred on the side of caution and assumed a value of 12% for both PACS 100 and 160 μm data, including the 2.2% correlated error.

2.4.2 aperture uncertainty

We followed the method of Ibar et al. (2010) for estimating the aperture uncertainty. We recorded the total flux within random square apertures of a given size which were laid down on the entire map. The standard deviation of these totals was measured and a 3- σ cut was then applied. The standard deviation was then re-measured and a further cut applied. This was repeated until convergence and the final value of the standard deviation was taken as the aperture noise for that sized aperture. This method invariably includes a contribution from the confusion noise in the final

⁵ http://herschel.esac.esa.int/Docs/SPIRE/html/spire_om.html

⁶ http://herschel.esac.esa.int/Docs/PACS/html/pacs_om.html

⁷ PACC-NHSC-TR-034

estimate and we make no attempt to separate the confusion noise from the instrumental noise.

We combined results from individual sub-images that were used to perform the photometry, and plotted the variation of aperture noise with aperture size for each band (Fig. 6). In this plot the horizontal axis corresponds to the radii of circular apertures whose areas are equal to the square apertures described above. As a sanity check, we also performed the same analysis using the entire southern-most tile, since it has the least cirrus contamination. The entire tile was rebinned using pixels equal to the aperture size. A simple background value was subtracted based on the mean of the surrounding, re-binned pixels. Iterative sigma-clipping was then performed on the rebinned, background-subtracted image.

In all the bands, the application of aperture corrections is clearly important for objects comparable to the size of the beam. If we consider first the SPIRE data. One would expect the noise to increase $\propto n_{px}^{0.5}$ for white noise, but in fact the dependence is closer to $n_{px}^{0.75}$ for both the entire tile and the sub-images. At large radii, the noise measured from the sub-images exhibits a break after which the dependence is closer to the $n_{px}^{0.5}$ as expected.

The difference between the noise measured from the entire tile and the noise measured from sub-images probably highlights the difference between the background estimation methods; the sub-images employ a high-order polynomial whereas for the entire tile, a simple mean is taken over a comparable area. Since the noise measured in the sub-images is closer to the expected value for Gaussian noise at large radii (although admittedly, the data are noisy), this is a good indication that the background subtraction is working well at removing background variation on these scales.

The $n_{px}^{0.75}$ dependence was unexpected. At first we thought that it was probably due to the contributions from background confusion and contaminating cirrus that was poorly fit. But the same behaviour was noticed in the PACS data which has much less contamination from background sources and cirrus. Most likely, there is another source of error which is unaccounted for, perhaps from the map-making scheme itself.

2.4.3 zero-point error

Zero-point errors were estimated from the map of the background fit. The standard deviation of the background was measured over the extent of the source and then multiplied by the number of pixels in the source aperture. This only contributed to a significant proportion of the uncertainty for extended, low-surface brightness objects, which were rare.

2.5 Verification of flux measurements

The flux measurements from PACS were verified by comparing our measurements to previous measurements of Virgo galaxies from ISO 100 & 170 μm (Tuffs et al. 2002), the IRAS Point Source Catalogue and the IRAS Faint Source Catalogue (Moshir et al. 1993). We applied colour corrections to the PACS fluxes in accordance with the instrument

Table 1. Linear fit parameters to comparisons of Herschel fluxes with literature values. Uncertainties are shown in parentheses.

Wavelength (μm)	Gradient	Intercept	scatter
100 ^a	0.97 (0.02)	-0.03 (0.02)	0.08
100 ^b	1.02 (0.04)	0.16 (0.03)	0.13
100 ^c	1.11 (0.02)	-0.08 (0.02)	0.05
100 ^d	1.11 (0.02)	-0.09 (0.02)	0.08
160 ^a	1.041 (0.006)	-0.048 (0.006)	0.02
160/170 ^b	1.08 (0.04)	-0.01 (0.03)	0.13
250 ^a	1.012 (0.004)	-0.006 (0.003)	0.02
250 ^e	0.997 (0.004)	0.020 (0.003)	0.02
350 ^a	1.015 (0.006)	-0.012 (0.003)	0.02
350 ^e	0.989 (0.004)	0.017 (0.003)	0.02
500 ^a	0.994 (0.007)	0.009 (0.006)	0.03
500 ^e	0.98 (0.01)	0.028 (0.005)	0.03

^a BGS (Davies et al. 2011)

^b ISO (Tuffs et al. 2002)

^c IRAS PSC

^d IRAS FSC

^e HRS (Ciesla et al. 2012)

team recommendations⁸ in order to compare our measurements with those taken with ISO. When obtaining these correction factors, we assumed a blackbody temperature of 20K, typical for dust in these galaxies (Davies et al. 2012). No colour correction is required to compare PACS 100 μm with IRAS 100 μm data.

A cross-match of sources yielded 46 matches from Tuffs et al. (2002), 70 from the IRAS PSC and 83 from the IRAS FSC. Although instrument-independent measurements at 250, 350 and 500 μm do not exist for the Virgo galaxies we have compared our results, which are based on an automatic measuring technique, with those of the BGS and the Herschel Reference Sample (Ciesla et al. 2012) which employ alternative, manual aperture photometry. For the BGS we used the original apertures but applied them to the new datasets to account for any change in flux calibration between the old data and the data presented here.

Straight-line fit parameters (with 1σ uncertainties) to the log-log plots displayed in Fig. 7 are shown in Table 1. In most cases the fit values are consistent with a 1:1 correlation, to within the scatter in the residuals, so we have high confidence in the fluxes in our catalogue for which there are no previous measurements. There is a tendency to measure higher fluxes in PACS 100 μm compared to IRAS 100 μm data, but this tendency has already been independently identified by the instrument team and is currently under investigation. There is a notable discrepancy between our

⁸ http://herschel.esac.esa.int/twiki/pub/Public/PacsCalibrationWeb/cc_report.v1.1

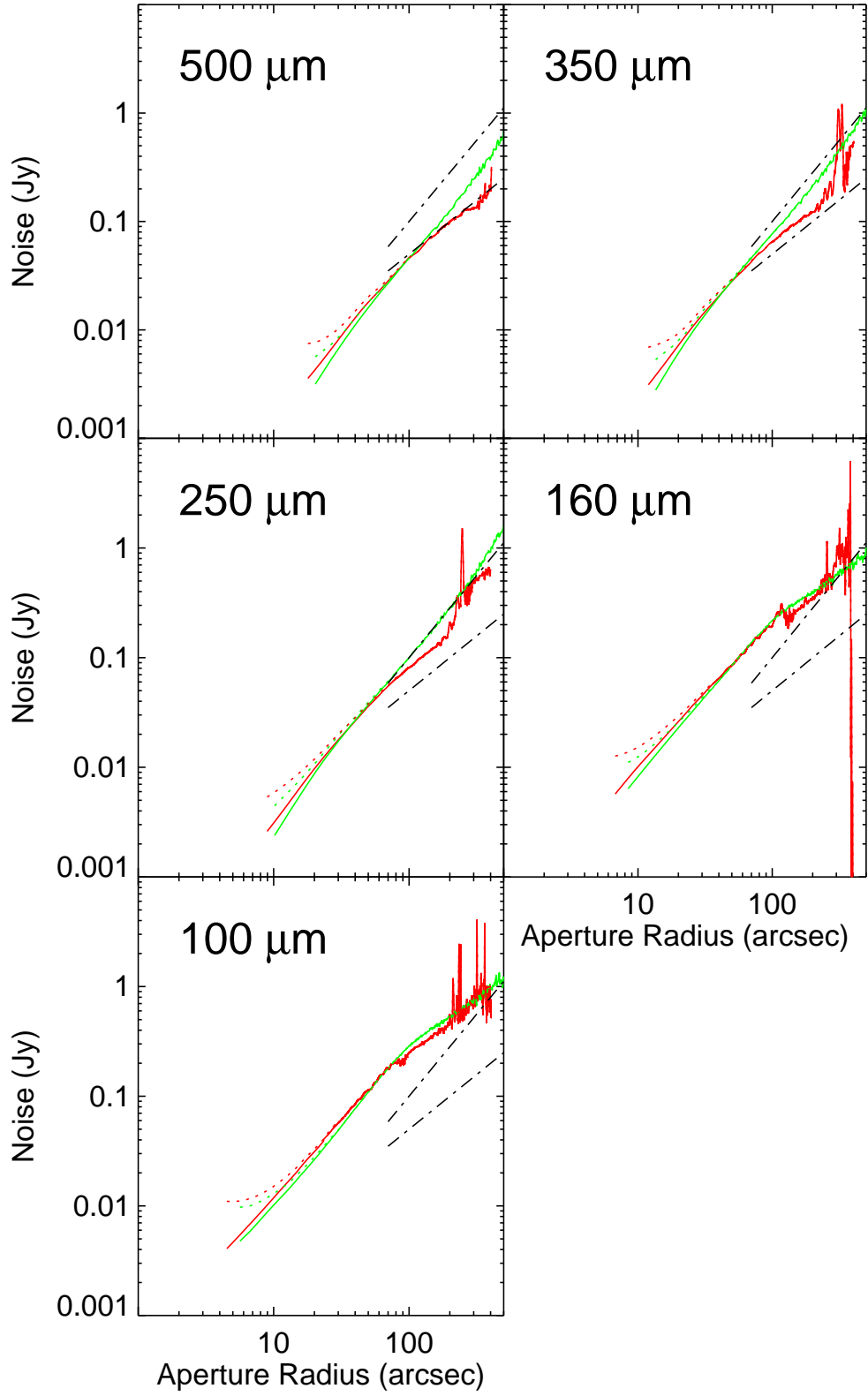


Figure 6. Variation of aperture noise with circular aperture radius. Green lines are apertures measured from the entire, full-depth region within the southern tile. Red lines show the combined results from sub-images that were extracted from the entire map to perform photometry on individual targets. Dotted lines show the same data with aperture corrections applied. Overplotted dot-dashed lines show $\sigma_{aper} \propto n_{px}^{0.5}$ and $\sigma_{aper} \propto n_{px}^{0.75}$ for comparison.

measurements and the BGS measurements of VCC785 in the 160 μm data at ~ 0.45 Jy. The immediate area surrounding the galaxy at 160 μm has significant negative flux values, and the original BGS aperture, which is based on the extent of the galaxy at 500 μm envelops these features, reducing the total flux substantially.

2.6 SED Fitting

We have attempted to fit the SED for each galaxy under the assumption that the emission is entirely from thermal dust. M87 (VCC1316), M84 (VCC763) and NGC4261 (VCC345) were omitted since these galaxies have significant synchrotron emission that could potentially contaminate the SPIRE fluxes (Baes et al. 2010, Smith et al. 2012b). We employed a single-temperature modified blackbody model with a fixed emissivity index, $\beta = 2$, to fit all the galaxies for which we had flux measurements across all bands. The dust mass-opacity coefficient used was $0.192 \text{ m}^2 \text{ kg}^{-1}$ at 350 micron (Draine 2003). We realise that adopting a single-temperature fit and a fixed $\beta = 2$ may be viewed as contentious in the light of recent results (e.g. Planck Collaboration et al. 2011, Dale et al. 2012, Boselli et al. 2012) however the BGS galaxies have been shown to be well modelled by a single-temperature, $\beta = 2$ fit (Davies et al. 2012, Magrini et al. 2011). β is still a poorly understood quantity and may not even be constant within a single galaxy (Planck Collaboration et al. 2011, Smith et al. 2012a). We have chosen the simplest approach which is probably the best we can achieve with the wavelength coverage at our disposal and will provide a benchmark for future studies, which will exploit ancillary datasets to look at the effects of adopting multi-temperature, variable β models. We also acknowledge that the range of β that exist in the literature can typically lead to a factor of a few difference in the derived dust mass. This can rise to a factor of 10 if an extreme $\beta = 1$ model is assumed (Cortese et al. 2012).

The SED-fitting algorithm works by minimising the difference between the set of measured fluxes and a set of model fluxes at the same wavelengths. The model fluxes are generated by taking a modified blackbody function and multiplying it by the Herschel filter profiles. This step requires measured fluxes that have had the original K4 scaling factor removed. A simplex technique is used to find the most likely combination of temperature and mass and several thousand Monte-Carlo simulations are then employed to derive the error distributions for the dust mass and temperature. These simulations lend a greater degree of robustness over simpler χ^2 -minimising algorithms which might assume that the error distributions are Gaussian. The method also takes into account uncorrelated calibration uncertainties for SPIRE and PACS (see section 2.2 for these values) and correlated calibration errors between SPIRE bands which are of the order of 5%. The results of the Monte-Carlo simulations indicated that the errors in dust mass and temperature are anti-correlated, but are centred on the correct values (see Smith et al. 2012a).

In order to estimate the dust mass, it was necessary to provide an estimate for the distance. We have adopted the distances provided by GOLDMINE which quote the average distance to the sub-cluster to which each individual galaxy belongs, as measured in Gavazzi et al. (1999).

Table 2. Herschel detection rates of VCC galaxies contained within the HeViCS survey limits. Results are given for the whole survey region and the inner region covered to full depth.

Wavelength (μm)	Entire Survey region (84 sq. deg.) (750 objects)	8-scan Survey region (inner 55 sq. deg.) (602 objects)
500	204 (27%)	160 (27%)
350	232 (31%)	184 (31%)
250	254 (34%)	203 (34%)
160	210 (28%)	176 (29%)
100	195 (26%)	165 (27%)

In some cases it was clear, both from the χ^2 values and from visual inspection of the fits that a single temperature fit was an inappropriate choice. We have not attempted further modelling of these galaxies since future papers will examine multi-temperature models, employing variable β , with the help of additional datasets which will provide the necessary extra wavelength coverage to better constrain the more complex models (Grossi et al. 2012, in prep.).

3 RESULTS

3.1 Detection Rates

Table 2 displays the detection rates for the entire 84 sq. deg. region and the inner 55 sq. deg. covered to optimum depth. In this table we have included all galaxies that yielded a detection at 250 μm . The breakdown of the FIR detections by m_{pg} for each wavelength are shown in Fig. 8 (top row) for the two survey regions. Surprisingly there does not appear to be any significant decrease in detection rates in the regions with less coverage. This is probably suggesting that Herschel is sensitive enough to detect all the FIR-emitting Virgo galaxies within a couple of passes. Individual fluxes for each galaxy can be found in Table B.

The difference between FIR detections (predominantly thermal dust) and optical detections is evident at low optical luminosities in Figs. 8 and 9. The galaxy cluster population is dominated by low luminosity dwarfs, in particular dwarf ellipticals (dEs), but few of these galaxies are detected in FIR. Since these galaxies are deficient in dust, it is unsurprising that their detection rates are low. This is also demonstrated in Fig. 8(b), which displays the same information but broken down by galaxy type. The other early-types also have low detection rates, as these too have little dust present in the ISM. The late-types have high detection rates in both PACS and SPIRE as one would expect since these galaxies are rich in dust.

Fig. 9 shows the morphology-magnitude plot, highlighting detected and undetected galaxies. This plot allows us to compare different galaxy morphologies at the same optical magnitude. From this it is clear that the lack of FIR detections of dEs, ellipticals (Es) and irregulars (Im/S) is not simply because they are faint at optical magnitudes - there are many FIR non-detections which have an optical magnitude greater than the faintest detection.

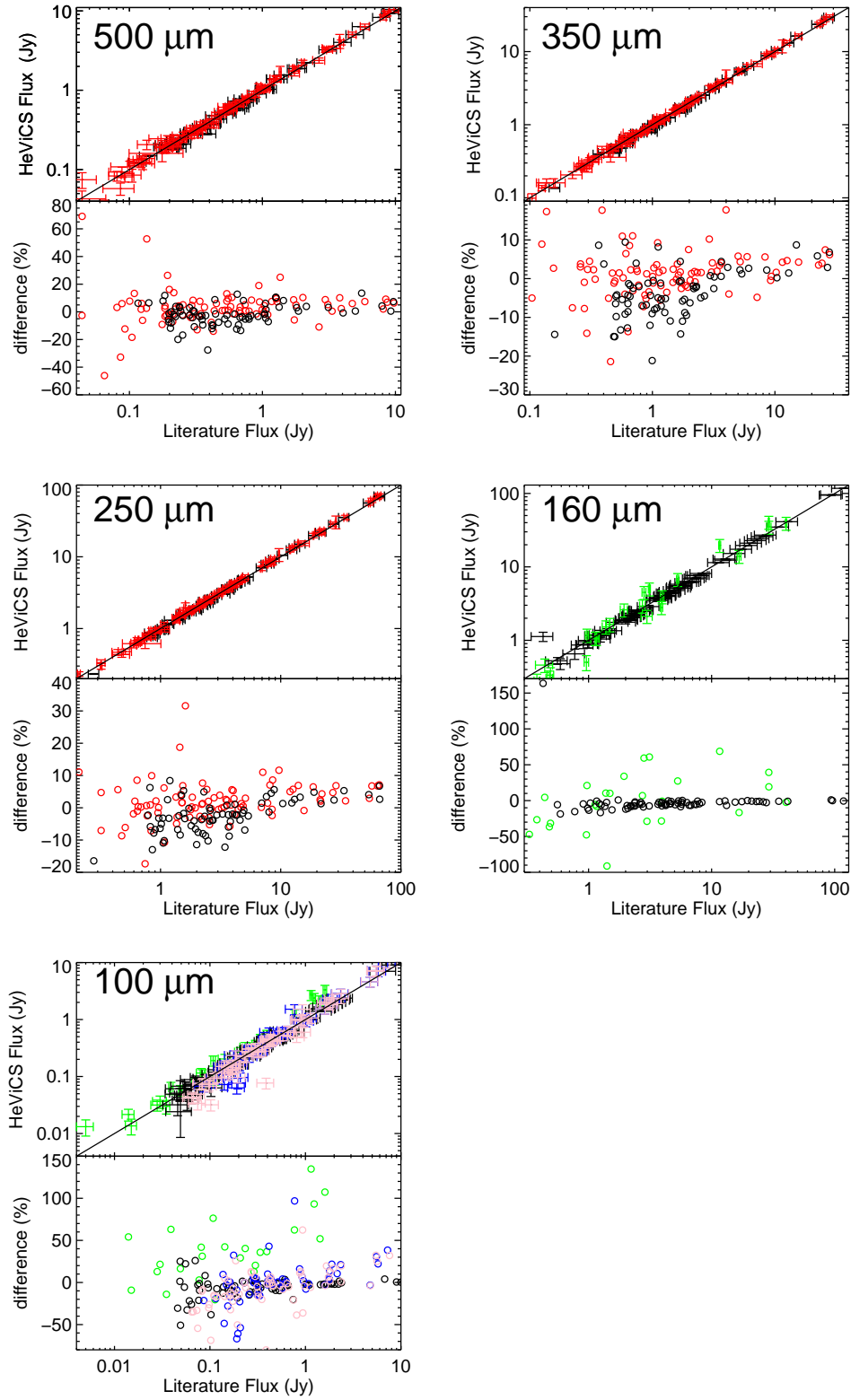
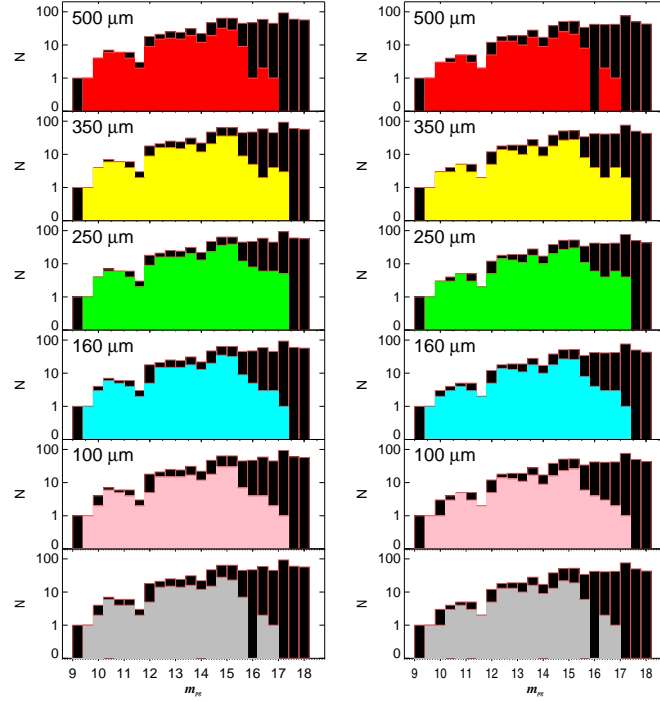
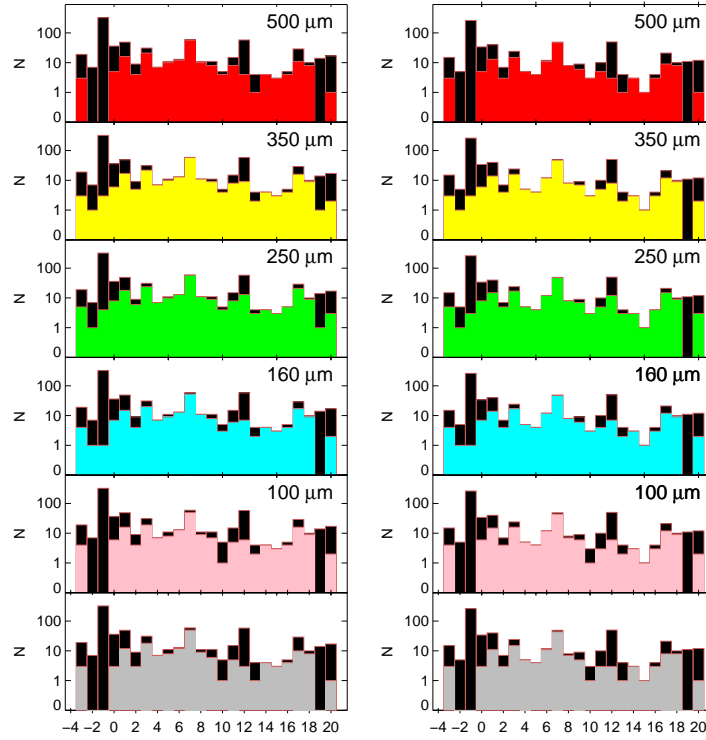


Figure 7. Herschel flux comparisons with ISO (green open circles), IRAS Point Source Catalogue (blue open circles), IRAS Faint Source Catalogue (pink open circles), the HeViCS BGS (open black circles) and the Herschel Reference Sample (open red circles). *top left:* 500 μm *top right:* 350 μm *middle left:* 250 μm *middle right:* 160 μm *bottom left:* 100 μm . The 1:1 fit lines is shown in black, see text for details of individual fits to the plots. The percentage difference between HeViCS and the literature values are given below each plot. The outlier at 160 μm is VCC785 (see text for further details).



(a) Distribution of FIR detections sorted by photographic apparent magnitude, m_{pg} .



(b) FIR detections sorted by morphological type.

Figure 8. FIR detections for the VCC galaxies. The left hand panels correspond to the entire survey region (84 sq. deg.), the right hand panels to the central 55 sq. deg. with optimum coverage. Black represents the optical detections of the VCC galaxies down to the completeness limit, $m_{pg} \leq 18$. 500 μ m, 350 μ m, 250 μ m, 160 μ m, 100 μ m & 5-band detections are represented by red, yellow, green, cyan, pink and grey histograms respectively. Galaxy morphology is as follows: **-3:** dS0, **-2:** dE/dS0, **-1:** dE (d:E), **0:** E - E/S0, **1:** S0, **2:** S0a - S0/Sa, **3:** Sa, **4:** Sab, **5:** Sb, **6:** Sbc, **7:** Sc (dSc), **8:** Scd, **9:** Sd, **10:** Sdm - Sd/Sm, **11:** Sm, **12:** Im (Im/S), **13:** Pec, **14:** S/BCD (dS/BCD dS0/BCD Sd/BCD), **15:** Sm/BCD, **16:** Im/BCD, **17:** BCD, **18:** S (dS), **19:** dIm/dE, **20:** ?

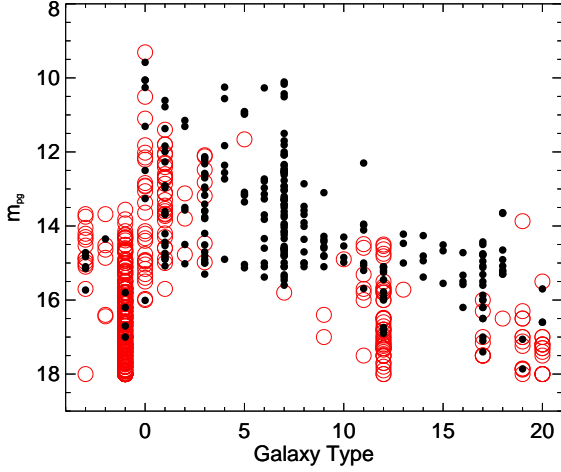


Figure 9. Morphology-magnitude plot for the VCC sample within the entire HeViCS area. Galaxies with a detection in at least one band are black solid circles, while undetected galaxies are open red circles. Galaxy morphology numbering follows that in Fig. 8.

The Magellanic-type dwarfs are notable by their lack of detection rates amongst the late-types. Although these systems are metal-poor and would not necessarily be expected to contain much dust, they are of similar metallicity to the blue compact dwarfs (BCDs), which have a higher detection rate. This suggests that the lack of Sm/Im galaxies is more than likely due to these galaxies falling below the surface brightness detection threshold.

Although the early-types are more readily detected in the optical compared to the FIR, the bins are by no means empty as one might expect of a population of dust-deficient systems. These exceptional galaxies have been the focus of previous HeViCS studies (e.g. Grossi et al. 2010, de Looze et al. 2010, Smith et al. 2012b) and will be the subject of future analyses as these new data are fully exploited (di Serego Alighieri, 2012 in prep. Grossi et al. 2012, in prep.).

3.2 Background Contamination

As explained in Section 2.3, during the formation of the catalogue, some FIR detections were rejected either because the FIR emission did not coincide with a foreground optical galaxy, or could not be distinguished from the surrounding cirrus. Despite the precautions taken to avoid contamination from background sources, there is still a possibility of accidentally reporting the flux from a background galaxy.

In order to estimate this effect, we have adopted a naïve approach. We restricted the analysis to the total population of point sources and undetected sources. Extended sources at the expected positions of Virgo galaxies can be reliably attributed to those galaxies. We then assumed that the background galaxy population is randomly distributed on the sky and worked out the probability of a chance alignment within each SPIRE beam, based on the source counts of Glenn et al. (2010). This probability is then used to predict

Flux bin (mJy)	N_a	N_r	N_p (deg ⁻²)	contamination %	N_c
250 μm					
15 – 20	8	47	1694	5.5	28
20 – 45	20	41	1824	5.9	31
45 – 100	6	6	313	1	5
100+	4	1	25	0.08	0
350 μm					
17 – 20	1	27	566	3	17
20 – 45	20	55	1209	7	38
45 – 100	6	4	154	0.9	5
100+	4	1	73	0.3	1.6
500 μm					
17 – 20	3	14	185	2	11
20 – 45	29	45	614	7	41
45 – 100	3	2	19	0.2	1
100+	2	0	1	0.01	0

Table 3. Estimates of contamination from background galaxies in the SPIRE bands. N_a is the number of sources that were accepted into the catalogue, N_r is the number of sources that were rejected as spurious, N_p is the number density of sources predicted from the number counts of Glenn et al. (2010). Contamination is the expected percentage contamination based on the source counts. N_c is the expected number of contaminating sources.

the number of possible spurious sources in the catalogue in different flux bins.

If one has chosen the rejected galaxies wisely, then one would expect that the number of spurious measurements should be approximately equal to the predicted number of contaminating background sources. In Table 3 we show the results of this test. From this table we see that at 500 μ m the number of rejections is approximately equal to the number of predicted sources. At 350 & 250 μ m we appear to have been overzealous in excising galaxies at the lowest fluxes. We attribute at least some of the increase in the number of spurious detections to peaks in the cirrus, which are expected at these low fluxes. Above 45 mJy the number of rejected sources compares well with the predictions.

The agreement between the number of spurious sources and the number of predicted background sources does not guarantee that the correct set of galaxies has been selected in the catalogue. However, the fact that the selection was made by comparing FIR emission with optical data does provide a greater degree of reliability. The combination of these points suggests it is likely that none of the catalogue has been misidentified.

3.3 FIR colours

Recently, Boselli et al. (2012) examined SPIRE colours for the HRS sample of 322 nearby galaxies. They observed a number of trends between FIR colour, metallicity, star formation history, the ionising radiation field and surface brightness. They also used the SPIRE only colours to argue that when fitting a fixed emissivity index, single-

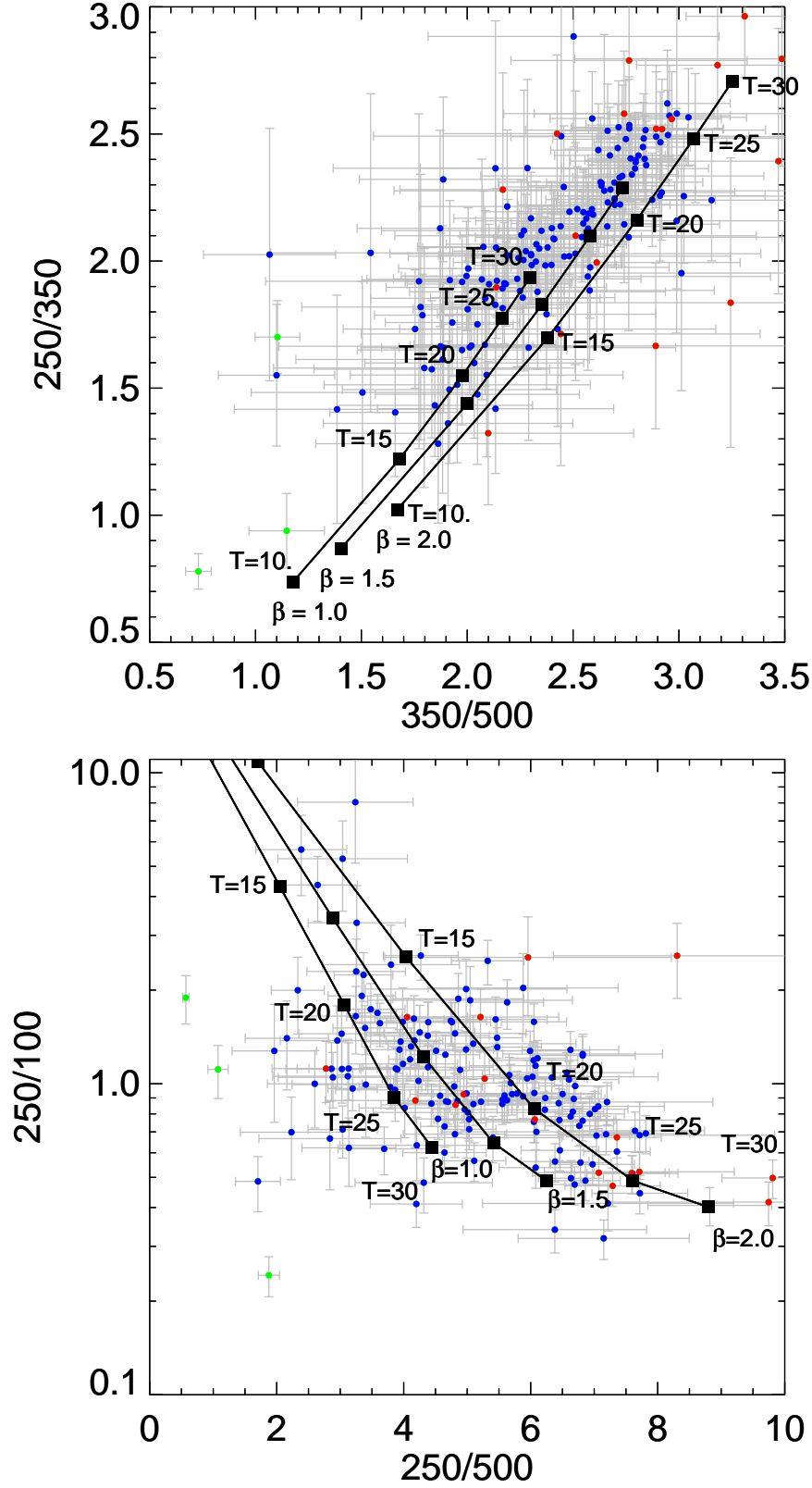


Figure 10. Colour-colour plots for the entire HeViCS catalogue detected in all bands. Blue points are late-types, red points are early-types and green points are galaxies known to harbour AGN. Loci connecting models of constant β , but variable temperature are overplotted in black, with different temperatures labelled every 5 K.

temperature modified blackbody model to the FIR SED, $\beta = 2$, is inappropriate for all but the most metal-rich, high surface brightness galaxies in the HRS. However, due to the degeneracy between temperature and β , SPIRE-only colours are not adequate to constrain β . We demonstrate this with Figures 10(a) & 10(b) which compare SPIRE only colours with SPIRE-PACS colours.

The fluxes that were used to create these figures were derived using the fluxes from Table B, and dividing out the K_4 factor. This provides us with a set of instrumental fluxes, that have been corrected for the size of the aperture, with no assumption on spectral index. We then generated a set of ideal modified blackbody functions with varying β and temperatures. These models were multiplied by the instrument filter functions to reproduce the instrumental fluxes for each band. The black filled squares in Figs 10(a) & 10(b) represent the theoretical colours derived from these model instrumental fluxes. Loci joining models of constant β but variable temperature were then overplotted (black lines).

Grey bars indicate the uncertainty in each colour. These have been derived by adding the relative flux uncertainties in quadrature for a given colour. Since colours common to one instrument are unaffected by correlated uncertainties, we have removed the 5% correlated error, when deriving the the SPIRE, $S250/S500$ colour uncertainty.

A comparison of Fig. 10(a) with Boselli et al. (2012) Fig. 9 shows that the galaxies in HeViCS exhibit similar trends in SPIRE colours to those in the HRS. There appears to be two clusters of objects around the $\beta = 1.5$ line and $\beta = 1$, but the uncertainties in the colours prevent one from disentangling the temperature- β degeneracy. So the cluster of galaxies around ($\beta = 1, T = 30$ K), could also be consistent with a ($\beta = 2, T = 17$ K) model.

The situation improves when a PACS colour is introduced (Fig. 10(b)). It is easier to distinguish between different models of β and T , and we are able to constrain the temperature with much greater accuracy. We now see that the HeViCS galaxies exhibit a range of β from 1 – 2 and the cold ($T < 15$ K) galaxies are unambiguously cold. Most of the galaxies appear to cluster around the models corresponding to $\beta = 1.5$ & $\beta = 2$ with temperatures varying between 20 – 30 K. This is very similar to the β, T distributions observed by Dunne & Eales (2001) and typical of values used in the literature (Magnelli et al. 2010, Skibba et al. 2011, Smith et al. 2012b, Dunne et al. 2011, Roseboom et al. 2012, Davies et al. 2012).

There is also a cluster of objects that are consistent with $\beta = 1$ models. Values of β as low as one are often observed in individual regions within the Milky Way (Dupac et al. 2003, Bracco et al. 2011) but are rarely seen in the SEDs of galaxies which are integrated over the whole galaxy. This region of the colour-colour plot becomes increasingly sensitive to contributions from either synchrotron or free-free emission (which would boost the 500 μm relative to the 250 μm), and warmer dust (which would boost the 100 μm relative to the 250 μm). The known AGN have the reddest colours but surprisingly we find a late-type, VCC223, in amongst them. An analysis of the SED reveals that it has a high 500 μm flux relative to the other bands. This excess could be due to free-free or synchrotron emission from recent star formation as this galaxy is classed as a BCD. However, we can't rule

out the possibility that this galaxy harbours a very cold dust component.

With such a large spread in the values of β implied by the data, it is a useful exercise to explore the validity of a single-temperature, fixed-beta modified blackbody model, which are commonly used throughout the literature.

3.4 SED fits, dust masses and temperatures

We restricted our analysis of the SEDs to 168 of the 171 galaxies which were detected in all five bands of PACS and SPIRE. M87, M84 and NGC4261 were omitted since their SEDs contain significant synchrotron emission and they, along with the other early-type VCC galaxies, will be the focus of a forthcoming paper (di Serego Alighieri et al. 2012 in prep.). The distribution of χ^2 for the 168 galaxies is shown in Fig. 11. For 140 galaxies the single-temperature model produced an adequate fit ($\chi^2_{\text{dof}=3} < 7.8$, at a confidence level of 95%) so that no further fitting was required. For the remaining 28 galaxies, the single-temperature model was unsuitable. This number of galaxies is significantly larger than the ~ 8 (5%) expected from the χ^2 distribution for 3 degrees of freedom, providing quantitative evidence that the single-temperature, $\beta = 2$ model is not appropriate for the FIR SEDs of all of these galaxies. Modelling of different dust populations will be studied in a future paper.

Out of the 429 early-type galaxies in the VCC that are located inside the HeViCS field, only 15 meet the requirement of $\chi^2_{\text{dof}=3} < 7.8$. This should be kept in mind in the following simple analysis since these galaxies are clearly unusual for their type. Dust masses and temperatures are recorded in Table C. On inspection, the upper and lower limits for the dust mass and temperature were symmetric to 1 significant figure, so we have just quoted one value. The SEDs are shown in Fig. D1. The χ^2 for each fit is recorded at the top of each plot.

In Fig. 12 we show the distributions of dust mass and temperature that were derived from our SED fits, using only the 140 galaxies with a $\chi^2 < 7.8$ from the single-temperature modified blackbody spectrum model fitting. Each plot shows the different distributions based on galaxy type; types earlier than Sa are shown in red outline, while types Sa and later are shown in blue.

The late-types exhibit a range in dust mass of $\log(M_{\text{dust}}/M_{\odot}) = 5.2\text{--}8.1$, with a mean value of $\log(\langle M_{\text{dust}} \rangle / M_{\odot}) = 7.1 \pm 0.1$. In contrast, the early-types exhibit a narrower range of masses; $\log(M_{\text{dust}}/M_{\odot}) = 5.4\text{--}7.0$, with a lower mean value of $\log(\langle M_{\text{dust}} \rangle / M_{\odot}) = 6.3 \pm 0.3$. For the temperature distributions, the late-types range from 12.9 – 26.4 K, with a mean value of $\langle T \rangle = 19.4 \pm 0.2$ K. The early-types cover a range in temperature from 16.2 – 25.9 K, with a mean value, $\langle T \rangle = 21.1 \pm 0.8$ K. A comparison of the dust properties of the late-types is consistent with those from the BGS. This isn't surprising, since the BGS consisted of the brightest FIR/sub-mm galaxies in HeViCS, which are mostly late-type galaxies.

We performed a Kolmogorov-Smirnov (K-S) two-sample test, Mann-Whitney U -test and an F-test to look for significant differences between the two sample populations and in addition, compared the two samples to their equivalent samples in the HRS (Cortese et al. 2012, Smith et al. 2012b). We note here that the HeViCS sample probes lower

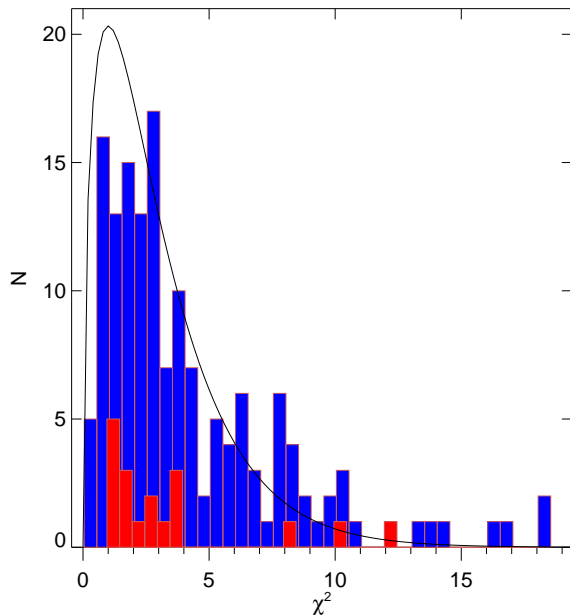


Figure 11. χ^2 distribution from single-temperature, modified blackbody model fits for 161 HeViCS galaxies with 5-band photometry. Early-type galaxies are shown in red, late-types in blue. Overplotted is the theoretical χ^2 distribution for 3 degrees of freedom, normalised to the bin value at the peak of the distribution.

mass galaxies than those in the HRS, which may slightly bias the results. The late-types comparison is limited to the mass distribution since Cortese et al. (2012) did not attempt to estimate dust temperatures for their sample.

The results of the tests are displayed in Table 4, and show that there is a clear distinction between the dust masses and temperatures of cluster late-types and cluster early-types: Virgo late-type galaxies have typically cooler, and more massive dust reservoirs than Virgo early-types. The tests also imply that late-types in the field have a significantly different mass distribution to those in the cluster. The effect of the cluster environment on the bulk dust properties of the early-types is much less pronounced, with the tests revealing a fairly high probability that the cluster and field samples were drawn from the same distribution. Since the early types are dominated by S0 galaxies in both samples, this is suggesting that the bulk dust properties of S0s are the same inside and outside the cluster. However, as noted in Cortese et al. (2012), differences in the dust properties may be more noticeable if the samples are defined on a property that is more indicative of a galaxy undergoing an interaction with the cluster, (e.g. HI-deficiency) rather than cluster membership alone.

One aspect of recent Herschel galactic studies that has provoked keen interest in the wider community is the existence of galaxies that seem to possess an excess of emission at 500 μm (e.g. Dale et al. 2012, Galametz et al. 2011, Grossi et al. 2010) so it would seem pertinent to comment on their presence in the catalogue. Such galaxies are interesting because there is still disagreement on the origin of the excess. The excess could be due to an as yet undiscovered very cold dust component, thermal free-free emission, syn-

chrotron emission or something more exotic (e.g. spinning dust Bot et al. 2010).

We have defined the excess as those galaxies whose 500 μm flux is at least 2σ above the model fit. This yields six candidates (VCC120, VCC223, VCC562, VCC848, VCC971 & VCC1673) with an excess at 500 μm . VCC1673 is discounted because of the contamination from VCC1676. VCC971 (NGC4423) is an Sd; VCC223, VCC562 & VCC848 are BCDs and VCC120 is classed as an Scd. We prefer not to speculate, at this point, as to the source of this excess, merely to highlight these objects as interesting. This is partly because six galaxies is about the amount of galaxies expected to be $2\text{-}\sigma$ outliers, but even if the deviations have non-statistical origins, we don't have sufficient wavelength coverage in this dataset to be able to constrain more complex SEDs which might account for the excess.

There is currently a HeViCS observing program with PACS at 70 μm which should help constrain the SED at the shorter wavelengths for a substantial sample of the Virgo galaxies displayed here. In addition to this, the recent work of Bendo et al. (2012) will provide Spitzer-MIPS photometry (24, 70 & 160 μm) for a significant fraction of the VCC galaxies. The combination of these two datasets will constrain the warmer (> 30 K) dust component, while ongoing millimetre observations and archived radio observations of the emerging population showing 500 μm excess, should be able to provide the necessary spectral coverage to constrain the longer wavelengths and ascertain the origin of the excess.

4 SUMMARY

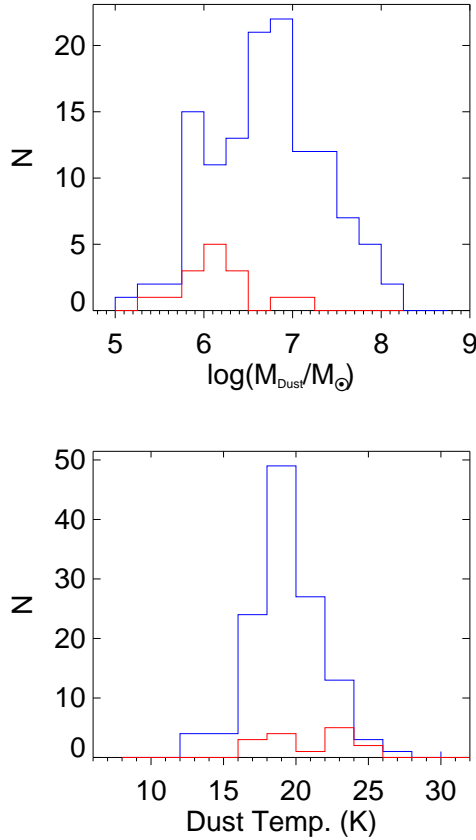
We have undertaken the largest and deepest survey of the Virgo Cluster at FIR wavelengths with the Herschel Space Observatory, utilising both PACS and SPIRE instruments. The survey, which is now complete in 5 FIR bands, covers 84 sq. deg. of the Virgo Cluster encompassing 750 VCC galaxies brighter than the optical completeness limit. We recover 254 (34%) of the VCC population in at least one wavelength and have 5-band FIR photometry for 171 galaxies. The photometry compares well with previous surveys showing typically less than a 10% variation across all bands.

FIR colours from PACS and SPIRE have been compared to model single-temperature modified blackbody spectra incorporating a fixed emissivity index. The distribution of colours is consistent with a range of $\beta=1\text{--}2$. This is supported by a study of the χ^2 distribution from $\beta=2$ model fits to the galaxies with 5-band photometry. The amount of galaxies not well fit by the model, is too large to be explained by random fluctuations. Further modelling is required to explore variable beta and/or different dust temperature populations, although this will likely require more measurements at FIR/MIR and submm wavelengths to be properly constrained.

A preliminary analysis of different morphological types indicates that dust in Virgo early-types has the same temperature and mass distribution as early-types in the field, suggesting that the environment has little impact on their bulk dust properties. Since the early-types are dominated by S0s, it suggests that the processes responsible for creating S0s has taken place before they enter the cluster. In

Table 4. Virgo cluster and field comparisons of the dust mass and temperature distributions of early- and late-type galaxies

Comparison samples		μ_1	σ_1	μ_2	σ_2	K-S test		MW U -test		F -test	
1	2					Value	p_{value}	Value	p_{value}	Value	p_{value}
Dust Mass ($\log(M_{dust}/M_{\odot})$)											
Cluster late	Cluster early	7.1	1.6	6.3	1.2	0.52	0.0007	-3.48	0.0002	64.27	10^{-10}
Cluster late	Field late	7.1	1.6	7.3	1.6	0.33	9×10^{-7}	4.82	7×10^{-7}	2.58	10^{-7}
Cluster early	Field early	6.3	1.2	6.6	1.2	0.29	0.45	0.67	0.25	2.61	0.08
Dust Temperature (K)											
Cluster late	Cluster early	19.4	2.5	21.1	3.2	0.34	0.06	1.82	0.035	1.7	0.14
Cluster early	Field early	21.1	3.2	23.5	4.6	0.31	0.37	1.50	0.07	2.06	0.18

**Figure 12.** Temperature and mass distributions split by galaxy type. Blue columns represent types Sa and later, red represents types earlier than Sa. Only galaxies whose model fits have $\chi^2 < 7.8$ are included.

contrast, the late-types have significantly different mass and temperatures to those in the field.

As well as providing a table of flux measurements and images of FIR SEDs with this manuscript, we will be providing the community with a legacy product which consists not only of the final 84 sq. deg. maps but also detailed data products such as cut-outs of the fully-processed images for each galaxy, the intermediate products that were used in the measurement process and the resulting radial profiles in each band. These will ensure the legacy value of the Herschel Virgo Cluster Survey.

ACKNOWLEDGMENTS

We would like to thank the anonymous referee for his/her helpful comments and suggestions for improving this manuscript.

SPIRE has been developed by a consortium of institutes led by Cardiff University (UK) and including Univ. Lethbridge (Canada); NAOC (China); CEA, LAM (France); IFSI, Univ. Padua (Italy); IAC (Spain); Stockholm Observatory (Sweden); Imperial College London, RAL, UCL-MSSL, UKATC, Univ. Sussex (UK); and Caltech, JPL, NHSC, Univ. Colorado (USA). This development has been supported by national funding agencies: CSA (Canada); NAOC (China); CEA, CNES, CNRS (France); ASI (Italy); MCINN (Spain); SNSB (Sweden); STFC (UK); and NASA (USA). HIPE is a joint development (are joint developments) by the Herschel Science Ground Segment Consortium, consisting of ESA, the NASA Herschel Science Center, and the HIFI, PACS and SPIRE consortia.

This research has made use of the GOLDMine Database, operated by the Università degli Studi di Milano-Bicocca

The research leading to these results has received funding from the European Community's Seventh Framework Programme (/FP7/2007–2013/) under grant agreement No. 229517.

REFERENCES

- Abadi M. G., Moore B., Bower R. G., 1999, *MNRAS*, 308, 947
- Alton P. B., et al., 1998, *A & A*, 335, 807
- Baes M., et al., 2010, *A & A*, 518, L53
- Bendo G. J., Galliano F., Madden S. C., 2012, *MNRAS*, 423, 197
- Binggeli B., Popescu C. C., Tammann G. A., 1993, *A & AS*, 98, 275
- Binggeli B., Sandage A., Tammann G. A., 1985, *AJ*, 90, 1681
- Boselli A., et al., 2012, *A & A*, 540, A54
- Boselli A., Gavazzi G., 2006, *PASP*, 118, 517
- Bot C., Ysard N., Paradis D., Bernard J. P., Lagache G., Israel F. P., Wall W. F., 2010, *A & A*, 523, A20
- Bracco A., et al., 2011, *MNRAS*, 412, 1151
- Chapin E. L., et al., 2011, *MNRAS*, 411, 505
- Ciesla L., et al., 2012, *ArXiv:1204.4726*
- Clemens M. S., et al., 2010, *A & A*, 518, L50

- Corbelli E., et al., 2012, *A & A*, 542, A32
- Cortese L., et al., 2010, *A & A*, 518, L49
- Cortese L., et al., 2012, *A & A*, 540, A52
- Côté P., Blakeslee J. P., Ferrarese L., Jordán A., Mei S., Merritt D., Milosavljević M., Peng E. W., Tonry J. L., West M. J., 2004, *ApJS*, 153, 223
- Dale D. A., et al., 2012, *ApJ*, 745, 95
- Davies J. I., et al., 2010, *A & A*, 518, L48
- Davies J. I., et al., 2012, *MNRAS*, 419, 3505
- de Looze I., et al., 2010, *A & A*, 518, L54
- de Vaucouleurs G., 1961, *ApJS*, 6, 213
- Devereux N. A., Young J. S., 1990, *ApJ*, 359, 42
- Dowell C. D., et al., 2010, in *SPIE Conference Series Vol. 7731 of SPIE Conference Series, Status of the SPIRE photometer data processing pipelines during the early phases of the Herschel Mission*
- Draine B. T., 2003, *ARA & A*, 41, 241
- Dunne L., Eales S. A., 2001, *MNRAS*, 327, 697
- Dunne L., Eales S. A., 2002, *A & SSci.*, 281, 321
- Dunne L., et al., 2011, *MNRAS*, 417, 1510
- Dupac X., Bernard J.-P., Boudet N., Giard M., Lamarre J.-M., Mény C., Pajot F., Ristorcelli I., Serra G., Stepnik B., Torre J.-P., 2003, *A & A*, 404, L11
- Ferrarese L., 2011, in *Fornax, Virgo, Coma et al., Stellar Systems in High Density Environments*, ESO Garching, Germany. Results from the NGVS
- Galamez M., Madden S. C., Galliano F., Honig S., Bendo G. J., Sauvage M., 2011, *A & A*, 532, A56
- Gavazzi G., Boselli A., Donati A., Franzetti P., Scodreggio M., 2003, *A & A*, 400, 451
- Gavazzi G., Boselli A., Scodreggio M., Pierini D., Belsole E., 1999, *MNRAS*, 304, 595
- Gavazzi G., et al., 2008, *A & A*, 482, 43
- Glenn J., et al., 2010, *MNRAS*, 409, 109
- Gomez H. L., et al., 2010, *A & A*, 518, L45
- Griffin M. J., et al., 2010a, *A & A*, 518, L3
- Griffin M. J., et al., 2010b, *A & A*, 518, L3
- Grossi M., et al., 2010, *A & A*, 518, L52
- Gunn J. E., Gott III J. R., 1972, *ApJ*, 176, 1
- Ibar E., et al., 2010, *MNRAS*, 409, 38
- Kennicutt Jr. R. C., et al., 2003, *PASP*, 115, 928
- Kim S., Rey S.-C., Sung E.-C., Yi W., Lisker T., 2011, in M. Koleva, P. Prugniel, & I. Vauglin ed., *EAS Publications Series Vol. 48 of EAS Publications Series, New Catalog and Ultraviolet Properties of Dwarf Galaxies in the Virgo Cluster*. pp 71–72
- Magnelli B., et al., 2010, *A & A*, 518, L28
- Magrini L., et al., 2011, *A & A*, 535, A13
- Marsden G., et al., 2009, *ApJ*, 707, 1729
- Mei S., et al., 2010, in *American Astronomical Society Meeting Abstracts 215 Vol. 42 of baas, The Next Generation Virgo Cluster Survey*. p. 470.05
- Merritt D., 1984, *ApJ*, 276, 26
- Mihos J. C., 2004, *Clusters of Galaxies: Probes of Cosmological Structure and Galaxy Evolution*, p. 277
- Mihos J. C., et al., 2005, *ApJL*, 631, L41
- Moore B., Katz N., Lake G., Dressler A., Oemler A., 1996, *Nature*, 379, 613
- Moshir M., et al., 1993, *VizieR Online Data Catalog*, 2156, 0
- Nguyen H. T., et al., 2010, *aa*, 518, L5
- Oosterloo T., van Gorkom J., 2005, *A & A*, 437, L19
- Pappalardo C., et al., 2012, *ArXiv: 1207.5051*
- Planck Collaboration Ade P. A. R., et al., 2011, *A & A*, 536, A17
- Poglitsch A., et al., 2010, *A & A*, 518, L2
- Pohlen M., et al., 2010, *A & A*, 518, L72
- Popescu C. C., et al., 2002, *ApJ*, 567, 221
- Roseboom I. G., et al., 2012, *MNRAS*, 419, 2758
- Skibba R. A., et al., 2011, *ApJ*, 738, 89
- Smith M. W. L., et al., 2010, *A & A*, 518, L51
- Smith M. W. L., et al., 2012a, *ApJ*, 756, 40
- Smith M. W. L., et al., 2012b, *ApJ*, 748, 123
- Tuffs R. J., et al., 2002, *ApJS*, 139, 37
- Vollmer B., Cayatte V., Balkowski C., Duschl W. J., 2001, *ApJ*, 561, 708

APPENDIX A: MODELLING THE GALAXY PAIR NGC4567/8 (VCC1673/6)

The interaction between NGC4567 and NGC4568 gives rise to a region of FIR emission consisting of contributions from each galaxy. Fig. A1a shows the 250 micron map of the region with the d_{25} ellipses outlined. A mask was constructed from the 250 μm data to isolate the emission from only NGC4567 (Fig. A1b). This galaxy was chosen because it is the fainter of the two. Since it is fainter, any error in the NGC4567 model will have less impact on the flux estimate in the overlapping region than attempting to model NGC4568.

The ellipse fitting procedure described in Section 2.2 was applied to the masked 250 μm image. The procedure was manually limited to an extent of $2'$ - the minimum distance to cover the overlapping region. The model was then constructed in two parts; for the region containing emission from only NGC4567, the original map data were used, for the overlap region, the surface brightness values from the ellipse fitting were used (Fig. A1c).

The model was then subtracted from the original map, to produce a map with only the estimated flux from NGC4568. An aperture was defined to encompass both galaxies in the original map to enable us to measure the total flux for both galaxies combined. Care was also taken to exclude bright background galaxies from this aperture. The same aperture was then used to measure the estimated flux of NGC4568 in the model-subtracted map (Fig. A1d).

The estimate of the flux in NGC4567 was then simply taken as the difference of the two measurements. The procedure was then repeated using the 250 μm mask and aperture as the templates for the other bands. The resulting fluxes are very similar to the BGS values which employed a simple spatial cut between galaxies to define the extent of each. This is probably because the emission in the overlap region is dominated by NGC4568. We have adopted a conservative estimate for the flux measurement uncertainty of 20% across all bands.

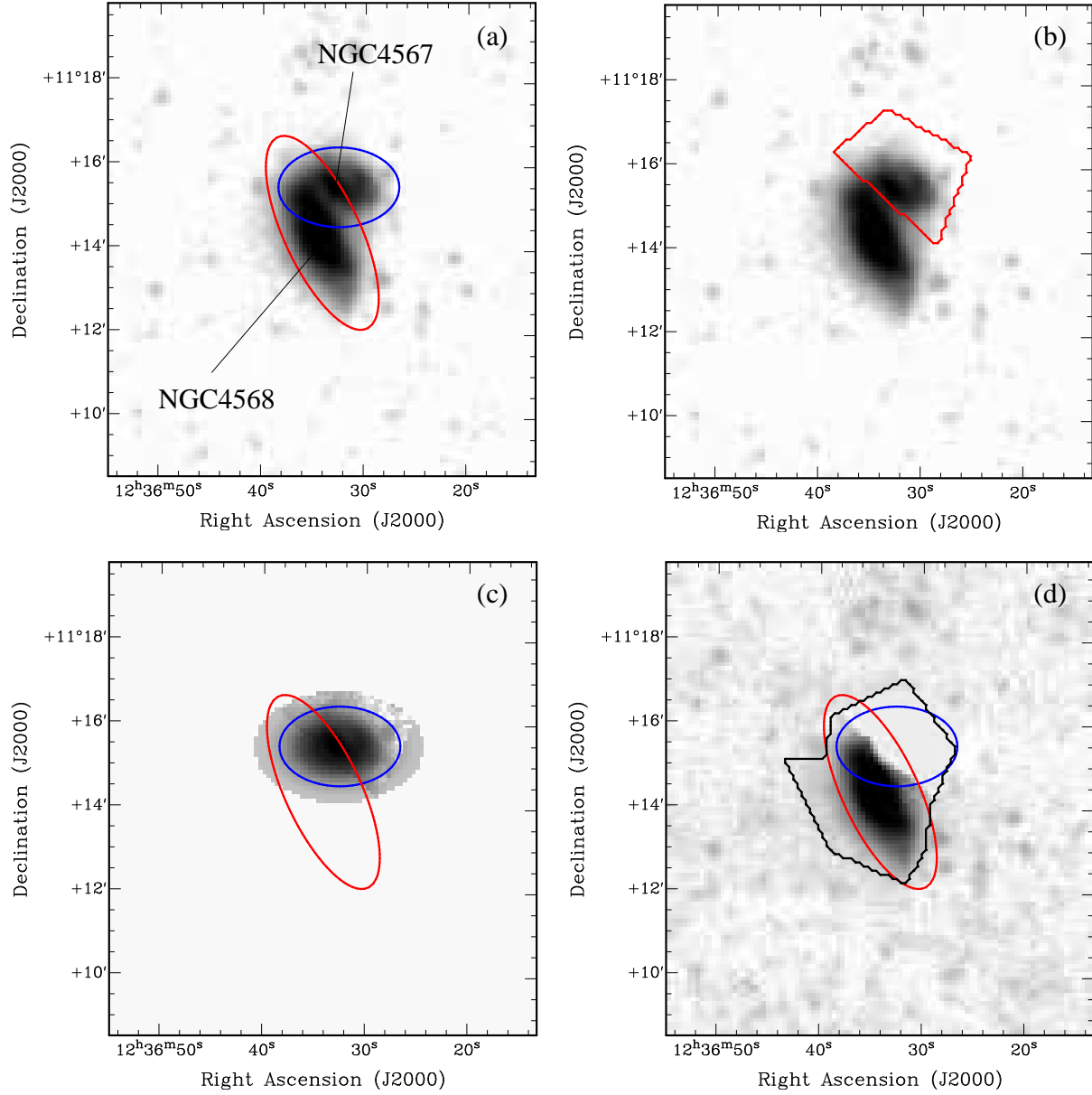


Figure A1. Images of the modelling process for galaxy pair NGC4567/8. Log flux scales have been employed to enhance the bright and dim features. (a) 250 μm grayscale image showing the two galaxies and their optical extent measured to d_{25} . (b) Isolated emission from NGC4567 (red outline) was used to create a mask. (c) the model of NGC4567. (d) The model-subtracted image showing only the emission from NGC4568. The aperture that was used to measure the total flux of the system is shown outlined in black.

APPENDIX B: TABLE OF FIR FLUXES AND UPPER LIMITS FOR 750 VCC GALAXIES IN THE HEVICS FIELD

OBJECT	RA h:m:s (J2000)	dec. d:m:s (J2000)	Type	S_{500} (σS_{500}) (Jy)	S_{350} (σS_{350}) (Jy)	S_{250} (σS_{250}) (Jy)	S_{160} (σS_{160}) (Jy)	S_{100} (σS_{100}) (Jy)
VCC1	12:08:20.30	+13:41:02.0	BCD	< (0.021)	0.029 (0.005)	0.088 (0.008)	0.179 (0.033)	0.198 (0.031)
VCC4	12:08:31.60	+15:05:42.0	Im (Im/S)	< (0.025)	< (0.024)	< (0.011)	< (0.011)	< (0.011)
VCC9	12:09:22.30	+13:59:33.0	dE (d:E)	< (0.027)	< (0.017)	< (0.011)	< (0.015)	< (0.010)
VCC10	12:09:24.90	+13:34:28.0	BCD	0.065 (0.019)	0.161 (0.021)	0.326 (0.032)	0.417 (0.065)	0.398 (0.058)
VCC11	12:09:35.80	+06:44:36.0	dE (d:E)	< (0.012)*	< (0.019)	< (0.012)	—	—
VCC12	12:09:44.30	+12:07:32.0	Sa	0.042 (0.009)	0.054 (0.008)	0.115 (0.015)	—	—
VCC15	12:09:54.60	+13:03:00.0	Sa	0.034 (0.008)	0.061 (0.014)	0.111 (0.020)	0.020 (0.006)	0.014 (0.004)
VCC17	12:10:01.80	+14:22:00.0	Im (Im/S)	< (0.026)*	0.041 (0.013)	0.050 (0.014)	< (0.014)	< (0.012)
VCC20	12:10:18.90	12:19:48.00	?	< (0.020)	< (0.016)*	< (0.018)*	< (0.029)	< (0.019)
VCC22	12:10:24.40	+13:10:14.0	BCD	< (0.022)	< (0.017)	0.024 (0.005)	0.014 (0.005)	< (0.011)
VCC24	12:10:35.60	+11:45:39.0	BCD	< (0.024)	0.031 (0.010)	0.072 (0.009)	0.089 (0.028)	< (0.028)
VCC25	12:10:37.50	+16:01:59.0	Sc	0.845 (0.070)	2.218 (0.165)	5.420 (0.386)	9.574 (1.153)	9.529 (1.157)
VCC26	12:10:40.90	+14:38:48.0	Im (Im/S)	< (0.023)	< (0.020)	< (0.011)	< (0.013)	< (0.008)
VCC28	12:10:45.60	+15:51:55.0	Sc	0.030 (0.009)	0.065 (0.014)	0.154 (0.021)	0.126 (0.034)	0.082 (0.020)
VCC29	12:10:48.90	+15:15:09.0	dE (d:E)	< (0.026)*	< (0.032)*	< (0.028)*	< (0.014)	< (0.010)
VCC30	12:10:54.50	+15:56:45.0	?	< (0.020)	< (0.020)	< (0.018)	< (0.023)	< (0.012)
VCC32	12:11:02.70	+12:06:14.0	E - E/S0	< (0.018)	< (0.022)	< (0.014)	< (0.022)	< (0.019)
VCC33	12:11:07.70	+14:16:30.0	dE (d:E)	< (0.022)	< (0.018)	< (0.013)	< (0.016)	< (0.013)
VCC34	12:11:10.00	+13:35:15.0	Sc	0.044 (0.014)	0.090 (0.019)	0.150 (0.023)	0.124 (0.024)	< (0.012)
VCC40	12:12:03.20	+14:54:17.0	Sbc	< (0.026)	0.068 (0.014)	0.145 (0.021)	0.239 (0.041)	0.019 (0.005)
VCC41	12:12:04.40	12:44:08.00	Im (Im/S)	< (0.023)	< (0.020)*	< (0.015)	< (0.016)	< (0.009)
VCC46	12:12:11.10	+12:53:35.0	dE (d:E)	< (0.022)	< (0.020)	< (0.013)	< (0.014)	< (0.013)
VCC47	12:12:11.80	+13:14:48.0	Sa	0.165 (0.023)	0.411 (0.043)	0.904 (0.075)	0.918 (0.122)	0.555 (0.089)
VCC48	12:12:15.10	+12:29:18.0	Sdm - Sd/Sm	0.087 (0.019)	0.166 (0.027)	0.285 (0.037)	0.213 (0.051)	< (0.011)*
VCC49	12:12:17.30	+13:12:19.0	E - E/S0	< (0.020)	< (0.013)	< (0.019)	< (0.016)	< (0.009)
VCC50	12:12:18.90	+15:28:59.0	dE (d:E)	< (0.022)	< (0.017)*	< (0.015)	< (0.015)	< (0.010)
VCC52	12:12:22.70	+06:58:47.0	Im (Im/S)	< (0.018)	< (0.021)	< (0.020)	< (0.036)	< (0.021)
VCC58	12:12:32.30	+12:07:26.0	Sb	0.445 (0.046)	0.974 (0.080)	1.865 (0.141)	2.379 (0.298)	1.338 (0.197)
VCC61	12:12:36.40	+06:30:07.0	dE (d:E)	< (0.027)*	< (0.020)*	< (0.010)	< (0.017)	< (0.011)
VCC65	12:12:43.20	12:07:19.00	dE (d:E)	< (0.019)	< (0.015)	< (0.015)	< (0.017)	< (0.010)
VCC67	12:12:48.50	+13:58:35.0	Sc	0.100 (0.021)	0.197 (0.030)	0.326 (0.039)	0.130 (0.029)	0.098 (0.029)
VCC68	12:12:49.10	+13:20:50.0	dE (d:E)	< (0.022)*	< (0.021)*	< (0.011)*	< (0.013)	< (0.010)
VCC70	12:12:56.30	13:04:07.00	dE (d:E)	< (0.034)	< (0.030)*	< (0.033)*	< (0.016)	< (0.011)
VCC73	12:13:03.00	+07:02:20.0	Sb	0.646 (0.051)	1.758 (0.127)	4.454 (0.314)	8.710 (1.052)	9.019 (1.086)
VCC74	12:13:04.60	+15:53:34.0	BCD	< (0.020)	< (0.017)*	< (0.021)*	< (0.016)	< (0.010)
VCC81	12:13:26.20	+14:46:20.0	Sc	0.050 (0.014)	0.088 (0.023)	0.134 (0.025)	< (0.019)	< (0.011)
VCC83	12:13:33.70	+14:28:49.0	Im (Im/S)	0.023 (0.007)	0.060 (0.014)	0.137 (0.020)	0.078 (0.023)	0.128 (0.029)
VCC85	12:13:36.50	+13:02:01.0	?	< (0.019)	< (0.019)	< (0.011)	< (0.025)	< (0.010)
VCC87	12:13:41.30	+15:27:13.0	Sm	0.120 (0.017)	0.200 (0.028)	0.282 (0.037)	0.302 (0.054)	0.139 (0.034)
VCC89	12:13:47.30	+13:25:29.0	Sc	1.047 (0.083)	2.986 (0.218)	7.117 (0.503)	11.246 (1.356)	9.609 (1.159)
VCC91	12:13:48.30	6:21:43.00	dE (d:E)	< (0.021)	< (0.011)	< (0.012)	< (0.016)	< (0.012)
VCC92	12:13:48.30	+14:54:01.0	Sb	4.944 (0.365)	12.857 (0.933)	28.135 (1.997)	39.938 (4.800)	26.075 (3.142)
VCC93	12:13:48.30	+12:41:26.0	dE (d:E)	< (0.017)	< (0.017)	< (0.015)	< (0.011)	< (0.009)
VCC94	12:13:50.40	+07:12:03.0	S0a - S0/Sa	0.040 (0.009)	0.161 (0.022)	0.354 (0.035)	—	—
VCC97	12:13:53.60	+13:10:22.0	Sc	0.742 (0.069)	1.769 (0.139)	3.641 (0.264)	5.472 (0.669)	3.249 (0.397)
VCC99	12:14:02.10	+06:43:23.0	Sa	0.062 (0.012)	0.160 (0.021)	0.302 (0.029)	0.320 (0.049)	0.159 (0.029)
VCC106	12:14:08.30	11:57:28.00	dE (d:E)	< (0.019)	< (0.015)	< (0.012)	< (0.016)	< (0.010)
VCC108	12:14:11.60	+15:57:54.0	dE (d:E)	< (0.024)*	< (0.021)*	< (0.024)*	< (0.016)	< (0.010)
VCC109	12:14:14.40	+13:32:35.0	dE (d:E)	< (0.018)*	< (0.020)	< (0.014)*	< (0.017)	< (0.012)
VCC113	12:14:32.90	+12:06:12.0	?	< (0.019)	< (0.016)	< (0.011)	< (0.016)	< (0.014)
VCC114	12:14:35.20	+05:40:36.0	Im (Im/S)	< (0.019)	< (0.014)	< (0.013)*	< (0.014)	< (0.013)
VCC115	12:14:34.70	+11:51:35.0	dE (d:E)	< (0.022)	< (0.017)	< (0.011)	< (0.016)	< (0.011)
VCC119	12:14:36.90	+12:48:43.0	Sc	0.030 (0.006)	0.042 (0.011)	0.065 (0.016)	0.019 (0.005)	< (0.012)
VCC120	12:14:38.50	+05:48:21.0	Scd	0.770 (0.062)	1.749 (0.131)	3.514 (0.253)	5.276 (0.637)	4.504 (0.548)
VCC122	12:14:44.20	+12:10:51.0	S0	< (0.020)	< (0.023)	< (0.012)	< (0.013)	< (0.010)

OBJECT	RA h:m:s (J2000)	dec. d:m:s (J2000)	Type	S_{500} (σS_{500}) (Jy)	S_{350} (σS_{350}) (Jy)	S_{250} (σS_{250}) (Jy)	S_{160} (σS_{160}) (Jy)	S_{100} (σS_{100}) (Jy)
VCC126	12:14:55.00	+13:27:38.0	Sd	0.055 (0.014)	0.142 (0.029)	0.210 (0.034)	< (0.016)*	< (0.011)
VCC127	12:14:58.60	+11:51:50.0	dE (d:E)	< (0.025)	< (0.015)	< (0.011)	< (0.019)	< (0.014)
VCC131	12:15:04.50	+14:01:44.0	Sc	0.347 (0.035)	0.780 (0.067)	1.574 (0.122)	1.873 (0.231)	1.219 (0.158)
VCC132	12:15:03.90	+13:01:55.0	Sd	< (0.020)	< (0.014)	< (0.010)	< (0.019)	< (0.012)
VCC135	12:15:06.70	+12:01:00.0	S/BCD	0.082 (0.015)	0.187 (0.025)	0.443 (0.041)	0.725 (0.100)	0.652 (0.093)
VCC137	12:15:08.60	+14:58:19.0	?	< (0.019)*	< (0.019)	< (0.015)	< (0.016)	< (0.009)
VCC140	12:15:12.50	+14:25:58.0	S0	< (0.021)	< (0.018)	< (0.016)	< (0.015)	< (0.011)
VCC143	12:15:16.10	+13:28:29.0	Sc	0.052 (0.015)	0.102 (0.017)	0.154 (0.020)	0.117 (0.028)	0.111 (0.029)
VCC144	12:15:18.30	+05:45:39.0	BCD	0.036 (0.008)	0.098 (0.013)	0.230 (0.022)	0.505 (0.066)	0.668 (0.084)
VCC145	12:15:16.80	+13:01:26.0	Sc	1.096 (0.087)	2.250 (0.166)	3.950 (0.290)	4.025 (0.496)	2.310 (0.297)
VCC155	12:15:35.70	+13:37:11.0	dS0	< (0.017)	< (0.013)	< (0.012)	< (0.015)	< (0.011)
VCC157	12:15:39.30	+13:54:05.0	Sc	1.896 (0.141)	5.385 (0.384)	13.403 (0.941)	23.015 (2.766)	19.442 (2.341)
VCC158	12:15:40.10	+15:00:20.0	dE (d:E)	< (0.021)	< (0.022)*	< (0.013)*	< (0.015)	< (0.015)
VCC165	12:15:53.30	+13:12:57.0	S0	0.022 (0.005)	0.078 (0.015)	0.187 (0.022)	0.215 (0.038)	0.072 (0.018)
VCC166	12:15:54.50	+06:24:04.0	S0	< (0.017)	< (0.011)	< (0.016)	< (0.015)	< (0.009)
VCC167	12:15:54.40	+13:08:58.0	Sb	3.970 (0.290)	10.230 (0.728)	21.820 (1.540)	27.700 (3.328)	15.342 (1.858)
VCC168	12:15:53.80	+14:01:31.0	Im (Im/S)	< (0.025)	< (0.039)*	< (0.055)*	< (0.022)*	< (0.019)*
VCC170	12:15:56.30	+14:26:00.0	Sd	< (0.022)	0.052 (0.008)	0.116 (0.016)	0.130 (0.026)	0.018 (0.004)
VCC172	12:16:00.40	+04:39:03.0	BCD	0.035 (0.006)	0.073 (0.015)	0.141 (0.020)	0.168 (0.033)	0.120 (0.025)
VCC178	12:16:09.00	+12:41:29.0	dE (d:E)	< (0.019)*	< (0.025)*	< (0.026)*	< (0.016)	< (0.012)
VCC181	12:16:14.60	+13:35:12.0	dE (d:E)	< (0.018)	< (0.016)	< (0.010)*	< (0.013)	< (0.011)
VCC187	12:16:22.50	+13:18:25.0	Scd	0.798 (0.065)	1.732 (0.128)	3.286 (0.235)	3.862 (0.471)	2.711 (0.343)
VCC199	12:16:33.70	+07:27:44.0	Sa	0.291 (0.029)	0.716 (0.074)	1.644 (0.120)	1.653 (0.217)	0.889 (0.148)
VCC200	12:16:33.70	+13:01:54.0	dE (d:E)	< (0.018)	< (0.012)	< (0.013)	< (0.020)	< (0.012)
VCC201	12:16:35.60	7:02:32.00	?	< (0.021)	< (0.021)	< (0.010)	< (0.013)	< (0.011)
VCC209	12:16:52.40	+14:30:55.0	dS0	0.045 (0.010)	0.117 (0.017)	0.233 (0.023)	0.214 (0.033)	0.141 (0.029)
VCC211	12:16:56.80	+04:03:26.0	dE (d:E)	< (0.020)	< (0.018)	< (0.012)	< (0.048)	< (0.013)
VCC213	12:16:56.00	+13:37:32.0	S/BCD	0.096 (0.013)	0.296 (0.028)	0.737 (0.059)	1.224 (0.154)	1.031 (0.129)
VCC216	12:17:01.10	+09:24:27.0	dE (d:E)	< (0.019)	< (0.014)	< (0.013)*	< (0.028)	< (0.016)
VCC217	12:17:04.40	+10:00:19.0	Im (Im/S)	< (0.016)*	< (0.012)*	< (0.017)	—	—
VCC218	12:17:05.30	+12:17:21.0	dS0	< (0.023)*	< (0.024)*	< (0.042)*	< (0.020)*	< (0.010)
VCC220	12:17:07.70	+07:37:28.0	S0	0.039 (0.008)	0.077 (0.008)	0.155 (0.012)	—	—
VCC221	12:17:09.10	+03:40:59.0	Sc	0.361 (0.033)	0.952 (0.075)	2.202 (0.159)	3.775 (0.462)	4.050 (0.494)
VCC222	12:17:09.90	+07:11:30.0	Sa	0.108 (0.016)	0.315 (0.033)	0.713 (0.060)	0.828 (0.112)	0.649 (0.088)
VCC223	12:17:10.70	+06:25:55.0	BCD	0.040 (0.008)	0.044 (0.007)	0.068 (0.006)	0.116 (0.023)	0.140 (0.025)
VCC224	12:17:09.30	+12:27:15.0	Scd	0.144 (0.020)	0.279 (0.031)	0.492 (0.042)	0.469 (0.071)	0.322 (0.051)
VCC226	12:17:11.40	+15:19:26.0	Sc	1.143 (0.089)	3.241 (0.233)	7.956 (0.562)	12.869 (1.549)	9.834 (1.183)
VCC227	12:17:14.50	+08:56:32.0	Sdm - Sd/Sm	< (0.023)	< (0.017)	< (0.016)*	—	—
VCC230	12:17:19.60	+11:56:36.0	dE (d:E)	< (0.020)	< (0.016)	< (0.010)	< (0.027)	< (0.016)
VCC234	12:17:25.80	+06:41:24.0	Sa	0.278 (0.037)	0.579 (0.058)	1.193 (0.095)	1.413 (0.187)	0.457 (0.067)
VCC235	12:17:26.50	+13:44:13.0	dE (d:E)	< (0.019)	< (0.013)	< (0.019)*	< (0.015)	< (0.011)
VCC236	12:17:28.90	+08:31:58.0	dE (d:E)	< (0.024)	< (0.019)	< (0.017)	—	—
VCC237	12:17:29.50	14:53:10.00	?	< (0.027)*	< (0.041)*	< (0.054)*	< (0.013)	< (0.007)
VCC241	12:17:33.70	+12:23:17.0	Sd	0.045 (0.011)	0.108 (0.020)	0.188 (0.027)	0.200 (0.045)	0.293 (0.053)
VCC244	12:17:39.90	5:20:32.00	dE (d:E)	< (0.017)	< (0.018)	< (0.014)*	< (0.016)	< (0.011)
VCC247	12:17:40.80	8:23:08.00	?	< (0.022)	< (0.016)	< (0.020)	? (0.000)	—
VCC252	12:17:45.90	+05:26:56.0	dE (d:E)	< (0.020)	< (0.018)	< (0.013)*	< (0.016)*	< (0.015)
VCC256	12:17:47.30	+04:28:43.0	S (dS)	0.025 (0.005)	0.056 (0.013)	0.119 (0.016)	0.227 (0.037)	0.081 (0.018)
VCC260	12:17:52.80	+05:01:37.0	Im (Im/S)	< (0.018)	< (0.019)	< (0.012)	< (0.018)	< (0.010)
VCC261	12:17:52.70	+13:10:36.0	dE (d:E)	< (0.017)	< (0.011)	< (0.012)	< (0.012)	< (0.009)
VCC262	12:17:55.80	+05:52:11.0	Sc	0.046 (0.010)	0.127 (0.021)	0.267 (0.026)	0.407 (0.060)	0.283 (0.043)
VCC266	12:17:59.40	+05:35:55.0	S0	< (0.023)	< (0.016)	< (0.015)*	< (0.012)	< (0.013)
VCC267	12:17:59.90	+06:39:15.0	Sbc	0.294 (0.042)	0.614 (0.063)	1.028 (0.093)	1.144 (0.169)	0.585 (0.110)
VCC270	12:18:06.80	+05:41:04.0	S0a - S0/Sa	< (0.021)	0.061 (0.012)	0.138 (0.016)	0.229 (0.037)	0.135 (0.024)
VCC273	12:18:09.60	+14:41:39.0	dE (d:E)	< (0.025)	< (0.016)	< (0.010)	< (0.015)	< (0.013)
VCC274	12:18:07.20	+05:55:50.0	BCD	< (0.018)	< (0.017)	< (0.015)	< (0.015)	< (0.013)
VCC275	12:18:11.00	+09:29:59.0	Im (Im/S)	< (0.022)	< (0.016)	< (0.011)	< (0.020)	< (0.012)
VCC278	12:18:14.40	+06:36:13.0	dS0	< (0.021)	< (0.020)	0.022 (0.004)	< (0.016)	0.017 (0.004)

OBJECT	RA h:m:s (J2000)	dec. d:m:s (J2000)	Type	S_{500} (σS_{500}) (Jy)	S_{350} (σS_{350}) (Jy)	S_{250} (σS_{250}) (Jy)	S_{160} (σS_{160}) (Jy)	S_{100} (σS_{100}) (Jy)
VCC281	12:18:15.30	+13:44:57.0	S/BCD	0.031 (0.007)	0.058 (0.007)	0.083 (0.008)	0.047 (0.007)	0.019 (0.004)
VCC282	12:18:17.90	+04:23:49.0	dE (d:E)	< (0.016)	< (0.017)	< (0.011)	< (0.015)	< (0.012)
VCC286	12:18:28.10	+05:36:57.0	Im (Im/S)	< (0.022)	< (0.019)	0.027 (0.004)	0.015 (0.005)	0.015 (0.004)
VCC287	12:18:28.50	+06:24:21.0	dE (d:E)	< (0.030)	< (0.039)	< (0.031)	< (0.022)	< (0.012)
VCC289	12:18:30.90	+05:33:34.0	Sc	0.110 (0.020)	0.209 (0.027)	0.347 (0.039)	0.350 (0.062)	0.307 (0.054)
VCC292	12:18:31.70	+05:50:59.0	dE (d:E)	< (0.025)	0.023 (0.005)	0.023 (0.004)	< (0.017)	< (0.010)
VCC293	12:18:31.90	+13:11:28.0	dE (d:E)	< (0.017)	< (0.018)	< (0.012)	< (0.012)	< (0.009)
VCC294	12:18:35.00	6:29:45.00	dE (d:E)	< (0.019)	< (0.015)	< (0.014)	< (0.015)	< (0.013)
VCC297	12:18:38.60	+06:42:30.0	Sc	0.028 (0.008)	0.070 (0.013)	0.142 (0.017)	0.146 (0.025)	0.105 (0.021)
VCC299	12:18:39.90	+13:35:54.0	dE (d:E)	< (0.020)	< (0.012)	< (0.012)	< (0.011)	< (0.010)
VCC303	12:18:42.90	+05:47:20.0	dE (d:E)	< (0.021)	< (0.016)	< (0.016)	< (0.018)	< (0.011)
VCC304	12:18:43.90	+12:23:09.0	dE (d:E)	< (0.018)	< (0.014)	< (0.017)	< (0.011)	< (0.008)
VCC307	12:18:49.60	+14:24:59.0	Sc	9.111 (0.648)	26.921 (1.911)	67.355 (4.738)	124.777 (14.977)	110.002 (13.204)
VCC308	12:18:50.90	+07:51:43.0	dS0	< (0.018)	< (0.015)	< (0.012)	—	—
VCC309	12:18:51.30	+12:35:52.0	Im/BCD	< (0.018)	< (0.016)	0.019 (0.004)	< (0.012)	< (0.006)
VCC312	12:18:56.20	+04:47:09.0	S0	< (0.021)	0.022 (0.006)	0.045 (0.010)	0.058 (0.017)	0.014 (0.005)
VCC315	12:19:00.50	+06:05:40.0	Sa	< (0.018)	< (0.016)	< (0.016)	< (0.024)	< (0.011)
VCC317	12:19:03.30	5:05:51.00	dE (d:E)	< (0.018)	< (0.015)	< (0.014)	< (0.013)	< (0.012)
VCC318	12:19:02.90	+08:51:22.0	Scd	0.114 (0.021)	0.270 (0.037)	0.485 (0.055)	0.527 (0.081)	0.328 (0.062)
VCC319	12:19:01.70	+13:58:56.0	dE (d:E)	< (0.022)	< (0.023)	< (0.017)	< (0.016)	< (0.011)
VCC320	12:19:05.70	+04:39:33.0	S (dS)	< (0.018)	< (0.012)	< (0.019)	< (0.017)	< (0.013)
VCC321	12:19:05.60	5:44:27.00	dE (d:E)	< (0.022)	< (0.016)	< (0.012)	< (0.017)	< (0.015)
VCC322	12:19:05.10	+13:58:50.0	Im (Im/S)	< (0.021)	0.026 (0.008)	0.036 (0.007)	0.020 (0.004)	0.015 (0.004)
VCC323	12:19:06.50	+05:43:33.0	Sa	0.096 (0.016)	0.252 (0.026)	0.584 (0.046)	0.890 (0.114)	0.505 (0.066)
VCC324	12:19:09.90	+03:51:21.0	BCD	0.094 (0.015)	0.213 (0.028)	0.396 (0.038)	0.785 (0.103)	0.954 (0.121)
VCC327	12:19:12.40	+06:22:53.0	S0	0.024 (0.006)	0.060 (0.013)	0.126 (0.021)	0.125 (0.026)	0.120 (0.023)
VCC328	12:19:11.30	+12:53:01.0	Im (Im/S)	< (0.029)	< (0.019)	0.021 (0.004)	< (0.014)	< (0.007)
VCC329	12:19:13.80	+05:59:09.0	Im (Im/S)	< (0.020)	< (0.019)	< (0.013)	< (0.016)	< (0.012)
VCC330	12:19:12.40	+12:51:07.0	dE (d:E)	< (0.020)	< (0.020)	< (0.011)	< (0.012)	< (0.008)
VCC331	12:19:15.50	+06:17:39.0	Pec	< (0.015)	< (0.016)	0.019 (0.004)	< (0.019)	< (0.009)
VCC332	12:19:15.30	+06:18:26.0	S0	< (0.018)	< (0.017)	< (0.011)	< (0.016)	< (0.012)
VCC334	12:19:14.20	+13:52:56.0	BCD	< (0.021)	0.033 (0.008)	0.070 (0.007)	0.157 (0.029)	0.136 (0.025)
VCC335	12:19:16.10	+15:23:39.0	dE (d:E)	< (0.016)	< (0.018)	< (0.013)	< (0.018)	< (0.010)
VCC336	12:19:17.60	+05:52:33.0	dE (d:E)	< (0.019)	< (0.014)	< (0.011)	< (0.016)	< (0.014)
VCC338	12:19:20.20	+05:28:01.0	dE (d:E)	< (0.020)	< (0.020)	< (0.016)	< (0.014)	< (0.010)
VCC340	12:19:22.10	+05:54:38.0	BCD	0.075 (0.013)	0.143 (0.020)	0.277 (0.029)	0.405 (0.057)	0.443 (0.062)
VCC341	12:19:22.20	+06:05:55.0	Sa	0.220 (0.031)	0.471 (0.050)	0.969 (0.079)	1.028 (0.138)	0.607 (0.084)
VCC342	12:19:22.20	+05:22:35.0	S0	< (0.023)	< (0.017)	< (0.009)	< (0.017)	< (0.011)
VCC343	12:19:21.70	+07:52:14.0	Sd	0.056 (0.013)	0.069 (0.014)	0.142 (0.020)	0.112 (0.035)	< (0.018)
VCC344	12:19:23.10	+05:47:41.0	E - E/S0	< (0.022)	< (0.018)	< (0.014)	< (0.019)	< (0.013)
VCC345	12:19:23.20	+05:49:31.0	E - E/S0	0.235 (0.027)	0.270 (0.034)	0.254 (0.030)	0.245 (0.038)	0.226 (0.035)
VCC346	12:19:23.80	+06:13:59.0	dE (d:E)	< (0.020)	< (0.016)	< (0.010)	< (0.016)	< (0.010)
VCC350	12:19:25.90	+13:18:39.0	Im (Im/S)	< (0.018)	< (0.013)	< (0.012)	< (0.013)	< (0.009)
VCC351	12:19:27.80	+05:02:51.0	E - E/S0	< (0.022)	< (0.028)	< (0.024)	< (0.016)	< (0.009)
VCC355	12:19:30.60	+14:52:40.0	S0	< (0.026)	< (0.030)	< (0.042)	< (0.016)	< (0.013)
VCC358	12:19:35.70	+05:50:48.0	Sa	< (0.020)	< (0.016)	0.024 (0.004)	0.014 (0.005)	< (0.009)
VCC361	12:19:36.90	+15:09:41.0	dE (d:E)	< (0.027)	< (0.030)	< (0.028)	< (0.016)	< (0.011)
VCC362	12:19:42.30	+05:32:17.0	Sa	0.210 (0.024)	0.586 (0.049)	1.390 (0.102)	2.158 (0.265)	1.332 (0.164)
VCC364	12:19:44.00	+12:16:45.0	Im (Im/S)	< (0.021)	< (0.014)	< (0.014)	< (0.012)	< (0.010)
VCC366	12:19:45.30	+06:00:21.0	S0	< (0.017)	< (0.013)	< (0.013)	< (0.017)	< (0.012)
VCC367	12:19:45.80	+05:27:27.0	Im (Im/S)	< (0.021)	< (0.024)	< (0.032)	< (0.017)	< (0.015)
VCC369	12:19:45.30	+12:47:54.0	S0	< (0.020)	< (0.023)	< (0.019)	< (0.013)	< (0.007)
VCC371	12:19:47.20	+05:17:01.0	S0	< (0.016)	< (0.013)	< (0.012)	< (0.014)	< (0.015)
VCC372	12:19:47.30	14:42:15.00	dE (d:E)	< (0.026)	< (0.019)	< (0.019)	< (0.014)	< (0.009)
VCC373	12:19:49.20	+06:00:54.0	S0	< (0.017)	< (0.013)	< (0.013)	< (0.016)	< (0.013)
VCC375	12:19:49.40	+05:27:48.0	S0	< (0.026)	< (0.042)	< (0.019)	< (0.013)	< (0.011)
VCC379	12:19:51.80	+05:59:57.0	?	< (0.021)	< (0.017)	< (0.018)	< (0.017)	< (0.013)
VCC381	12:19:54.10	+06:39:57.0	Im (Im/S)	< (0.019)	< (0.017)	< (0.013)	< (0.012)	< (0.012)

OBJECT	RA h:m:s (J2000)	dec. d:m:s (J2000)	Type	S_{500} (σS_{500}) (Jy)	S_{350} (σS_{350}) (Jy)	S_{250} (σS_{250}) (Jy)	S_{160} (σS_{160}) (Jy)	S_{100} (σS_{100}) (Jy)
VCC382	12:19:56.00	+05:20:36.0	Sc	1.572 (0.124)	4.196 (0.308)	10.572 (0.744)	21.339 (2.563)	22.036 (2.651)
VCC386	12:20:03.70	+05:20:28.0	Sa	< (0.025)*	< (0.030)*	< (0.025)*	< (0.018)	< (0.015)
VCC388	12:20:03.50	+06:00:39.0	dE (d:E)	< (0.020)	< (0.017)	< (0.011)	< (0.018)	< (0.010)
VCC389	12:20:03.30	+14:57:41.0	dS0	< (0.026)	< (0.017)	< (0.011)	< (0.015)	< (0.013)
VCC390	12:20:04.00	+05:24:53.0	dE (d:E)	< (0.027)*	< (0.016)*	< (0.014)*	< (0.017)	< (0.016)
VCC393	12:20:07.50	+07:41:31.0	Sc	0.281 (0.032)	0.724 (0.065)	1.586 (0.123)	2.321 (0.295)	1.772 (0.235)
VCC394	12:20:08.60	+09:28:05.0	dE (d:E)	< (0.017)	< (0.017)	< (0.017)	< (0.016)	< (0.010)
VCC397	12:20:12.20	+06:37:23.0	dE (d:E)	< (0.020)	< (0.023)*	< (0.019)*	< (0.015)	< (0.011)
VCC403	12:20:17.10	10:19:09.00	dE (d:E)	< (0.031)	< (0.018)	< (0.017)	< (0.009)	< (0.046)
VCC404	12:20:17.30	+04:12:06.0	Scd	0.219 (0.024)	0.506 (0.046)	1.026 (0.079)	1.185 (0.152)	0.818 (0.109)
VCC406	12:20:18.70	+08:31:59.0	Sbc	0.065 (0.014)	0.136 (0.021)	0.253 (0.031)	0.353 (0.062)	0.262 (0.044)
VCC407	12:20:18.80	+09:32:43.0	dE/dS0	< (0.016)	< (0.017)	< (0.014)	< (0.015)	< (0.010)
VCC408	12:20:21.50	+05:23:11.0	S0	0.092 (0.017)	0.254 (0.028)	0.710 (0.066)	1.284 (0.159)	1.347 (0.165)
VCC409	12:20:23.10	6:08:06.00	dE (d:E)	< (0.022)	< (0.017)	< (0.011)	< (0.019)	< (0.008)
VCC410	12:20:21.70	+12:11:14.0	BCD	< (0.022)	< (0.015)	0.015 (0.005)	< (0.014)	< (0.010)*
VCC411	12:20:24.30	+05:34:22.0	S0	0.044 (0.007)	0.096 (0.018)	0.220 (0.024)	0.269 (0.041)	0.235 (0.037)
VCC413	12:20:23.20	13:53:51.00	Im (Im/S)	< (0.029)	< (0.019)	< (0.015)	< (0.015)	< (0.013)
VCC414	12:20:24.50	+14:41:39.0	dIm/dE	< (0.022)	< (0.033)*	< (0.032)*	< (0.011)	< (0.012)
VCC415	12:20:25.20	+06:54:32.0	Sd	0.077 (0.015)	0.157 (0.024)	0.233 (0.030)	0.330 (0.052)	0.159 (0.036)
VCC418	12:20:26.30	+14:47:09.0	dE (d:E)	< (0.026)	< (0.020)	< (0.011)	< (0.014)	< (0.010)
VCC419	12:20:29.50	+10:14:42.0	Sb	0.065 (0.010)	0.150 (0.012)	0.326 (0.024)	0.828 (0.180)	0.346 (0.129)
VCC421	12:20:30.00	+13:31:09.0	dE (d:E)	< (0.024)*	< (0.019)	< (0.017)	< (0.015)	< (0.009)
VCC423	12:20:34.00	+02:58:09.0	Im (Im/S)	< (0.018)	< (0.016)	< (0.014)	< (0.033)	< (0.021)
VCC425	12:20:35.90	+08:12:09.0	Im (Im/S)	< (0.022)	< (0.022)*	< (0.018)*	< (0.016)	< (0.011)
VCC428	12:20:40.20	+13:53:20.0	BCD	< (0.020)	< (0.022)*	< (0.016)	< (0.013)	< (0.009)
VCC429	12:20:43.80	+14:37:51.0	?	< (0.020)	< (0.031)*	< (0.025)	< (0.018)	< (0.009)
VCC434	12:20:48.50	+05:38:23.0	S (dS)	0.109 (0.016)	0.298 (0.030)	0.642 (0.052)	1.034 (0.132)	0.697 (0.088)
VCC436	12:20:48.90	+06:43:25.0	dE (d:E)	< (0.029)*	< (0.023)*	< (0.011)*	< (0.018)	< (0.012)
VCC439	12:20:51.20	+07:03:33.0	dE (d:E)	< (0.018)	< (0.019)	< (0.014)	< (0.013)	< (0.009)
VCC440	12:20:51.80	+05:13:57.0	dE (d:E)	< (0.023)	< (0.020)*	< (0.017)*	< (0.017)	< (0.011)
VCC444	12:20:54.40	+14:59:34.0	dE (d:E)	< (0.020)*	< (0.017)*	< (0.013)	< (0.017)	< (0.011)
VCC446	12:20:57.90	+06:20:21.0	Im/BCD	0.017 (0.005)	0.030 (0.009)	0.058 (0.011)	0.043 (0.012)	0.057 (0.015)
VCC448	12:21:00.20	+12:43:33.0	Im (Im/S)	< (0.018)	< (0.014)	< (0.014)	< (0.011)	< (0.009)
VCC449	12:21:02.30	+03:43:19.0	Sbc	0.522 (0.046)	1.177 (0.090)	2.220 (0.166)	2.784 (0.342)	2.148 (0.264)
VCC450	12:21:03.70	+07:04:40.0	S0	0.045 (0.010)	0.131 (0.021)	0.219 (0.028)	0.311 (0.047)	0.253 (0.035)
VCC452	12:21:04.80	+11:45:17.0	dE (d:E)	< (0.021)	< (0.016)	< (0.012)	< (0.018)	< (0.010)
VCC453	12:21:06.00	+11:35:43.0	Sm	< (0.018)	< (0.016)	< (0.020)*	< (0.019)	< (0.012)
VCC454	12:21:05.40	+15:43:13.0	dE (d:E)	< (0.022)	< (0.031)*	< (0.035)*	< (0.015)	< (0.011)
VCC458	12:21:12.70	+08:57:47.0	dE (d:E)	< (0.022)	< (0.017)	< (0.008)	< (0.014)	< (0.012)
VCC461	12:21:15.00	+13:20:48.0	dE (d:E)	< (0.015)	< (0.020)	< (0.017)	< (0.009)	< (0.008)
VCC462	12:21:16.40	+04:35:44.0	S0a - S0/Sa	0.100 (0.020)	0.244 (0.028)	0.612 (0.053)	0.950 (0.123)	0.789 (0.103)
VCC464	12:21:17.00	+05:20:40.0	BCD	< (0.020)	< (0.019)	< (0.014)	< (0.014)	< (0.010)
VCC465	12:21:17.80	+11:30:38.0	Sc	0.925 (0.074)	2.154 (0.160)	4.315 (0.308)	6.751 (0.820)	5.850 (0.710)
VCC467	12:21:19.50	+03:47:16.0	Im (Im/S)	< (0.016)	< (0.014)	< (0.011)	< (0.013)	< (0.011)
VCC468	12:21:18.60	+04:04:34.0	BCD	< (0.019)	< (0.024)*	< (0.038)*	< (0.022)*	< (0.012)
VCC472	12:21:24.10	+15:37:07.0	dIm/dE	< (0.021)	< (0.018)	< (0.012)	< (0.014)	< (0.010)
VCC476	12:21:28.40	+10:29:04.0	Im (Im/S)	< (0.022)	< (0.018)	< (0.012)	< (0.027)	< (0.017)
VCC477	12:21:27.90	+15:01:28.0	Im (Im/S)	< (0.017)	< (0.017)	< (0.015)*	< (0.016)	< (0.013)
VCC479	12:21:29.00	+08:09:03.0	?	0.037 (0.009)	0.068 (0.013)	0.088 (0.015)	0.051 (0.015)	0.015 (0.004)
VCC482	12:21:34.10	+04:46:46.0	S0a - S0/Sa	< (0.019)*	< (0.019)*	< (0.021)*	< (0.017)	< (0.013)
VCC483	12:21:32.80	+14:36:22.0	Sc	1.891 (0.139)	5.299 (0.375)	12.692 (0.891)	19.905 (2.393)	14.038 (1.687)
VCC486	12:21:37.00	+05:45:56.0	S0a - S0/Sa	< (0.015)	< (0.019)	0.017 (0.004)	< (0.015)	< (0.012)
VCC488	12:21:39.30	+07:15:13.0	?	< (0.021)	< (0.016)	< (0.013)*	< (0.013)	< (0.007)
VCC489	12:21:39.90	+04:23:34.0	dE (d:E)	< (0.036)*	< (0.018)*	< (0.015)	< (0.018)	< (0.013)
VCC490	12:21:38.80	+15:44:43.0	dS0	< (0.023)	< (0.019)	< (0.017)	< (0.011)	< (0.012)
VCC491	12:21:40.90	+11:30:12.0	Scd	0.513 (0.048)	1.235 (0.103)	2.635 (0.196)	4.345 (0.528)	4.607 (0.560)
VCC492	12:21:41.50	+05:23:05.0	Sa	0.096 (0.022)	0.277 (0.028)	0.691 (0.058)	0.980 (0.125)	0.783 (0.101)
VCC494	12:21:41.60	+15:04:30.0	dE (d:E)	< (0.020)	< (0.019)	< (0.011)	< (0.019)	< (0.010)

OBJECT	RA h:m:s (J2000)	dec. d:m:s (J2000)	Type	S_{500} (σS_{500}) (Jy)	S_{350} (σS_{350}) (Jy)	S_{250} (σS_{250}) (Jy)	S_{160} (σS_{160}) (Jy)	S_{100} (σS_{100}) (Jy)
VCC497	12:21:42.50	+14:35:52.0	Sc	3.229 (0.234)	8.661 (0.618)	19.812 (1.406)	26.417 (3.173)	16.214 (1.949)
VCC499	12:21:45.40	+09:14:16.0	dE (d:E)	< (0.018)	< (0.014)	< (0.012)	< (0.020)	< (0.011)
VCC501	12:21:48.00	+12:49:36.0	dE (d:E)	< (0.018)	< (0.014)*	< (0.014)	< (0.011)	< (0.007)
VCC503	12:21:50.30	+08:32:30.0	dE (d:E)	< (0.019)	< (0.015)	< (0.011)	< (0.013)	< (0.012)
VCC504	12:21:50.10	+09:44:21.0	dE (d:E)	< (0.020)*	< (0.017)	< (0.012)*	< (0.015)	< (0.011)
VCC508	12:21:54.90	+04:28:25.0	Sc	8.103 (0.577)	22.809 (1.617)	55.231 (3.879)	106.859 (12.828)	97.873 (11.751)
VCC509	12:21:55.50	+06:27:06.0	Sdm - Sd/Sm	0.059 (0.015)	0.112 (0.022)	0.153 (0.024)	0.141 (0.030)	0.151 (0.035)
VCC510	12:21:53.70	+15:38:46.0	dE (d:E)	< (0.022)	< (0.015)	< (0.016)	< (0.012)	< (0.012)
VCC512	12:21:55.60	+11:58:01.0	Sm	0.024 (0.006)	0.043 (0.013)	0.035 (0.010)	< (0.018)	< (0.011)
VCC514	12:21:57.50	+08:40:30.0	Sc	< (0.024)*	0.074 (0.018)	0.137 (0.026)	0.135 (0.036)	< (0.011)
VCC517	12:22:01.30	+05:06:00.0	Sab	0.096 (0.013)	0.302 (0.030)	0.678 (0.055)	0.906 (0.116)	0.792 (0.102)
VCC520	12:22:01.70	+08:14:25.0	Im (Im/S)	< (0.013)	< (0.016)	< (0.012)	< (0.016)	< (0.012)
VCC522	12:22:03.60	+12:44:27.0	Sa	< (0.016)	< (0.020)	< (0.013)	< (0.008)	< (0.009)
VCC523	12:22:04.10	+12:47:15.0	dS0	< (0.018)	< (0.019)	< (0.013)*	< (0.013)	< (0.009)
VCC524	12:22:05.60	+09:02:37.0	Sbc	0.716 (0.057)	1.952 (0.141)	4.556 (0.322)	6.332 (0.764)	4.302 (0.519)
VCC525	12:22:06.50	+06:46:58.0	dE (d:E)	< (0.017)	< (0.017)	< (0.013)	< (0.011)	< (0.008)
VCC530	12:22:07.60	+15:47:57.0	Im (Im/S)	< (0.020)	< (0.019)	< (0.014)	< (0.014)	< (0.010)
VCC531	12:22:10.90	+04:57:06.0	Sa	< (0.020)	0.029 (0.009)	0.109 (0.020)	0.100 (0.031)	0.085 (0.018)
VCC534	12:22:12.40	+07:08:39.0	Sa	0.259 (0.034)	0.670 (0.063)	1.327 (0.106)	1.634 (0.200)	1.524 (0.186)
VCC535	12:22:12.10	+16:26:52.0	dE (d:E)	< (0.021)	< (0.020)	< (0.013)	< (0.024)	< (0.013)
VCC538	12:22:14.70	+07:10:02.0	E - E/S0	< (0.020)	< (0.017)	< (0.013)	< (0.013)	< (0.008)
VCC539	12:22:14.70	+14:08:30.0	dE (d:E)	< (0.024)	< (0.023)	< (0.020)	< (0.014)	< (0.013)
VCC542	12:22:19.50	+06:55:40.0	dE (d:E)	< (0.020)	< (0.018)	< (0.013)	< (0.013)	< (0.009)
VCC543	12:22:19.50	+14:45:38.0	dE (d:E)	< (0.018)	< (0.021)	< (0.015)	< (0.016)	< (0.011)
VCC545	12:22:19.60	+15:44:01.0	dE (d:E)	< (0.026)	< (0.014)	< (0.016)*	< (0.016)	< (0.010)
VCC546	12:22:21.60	+10:36:07.0	dE (d:E)	< (0.016)	< (0.020)	< (0.016)	< (0.019)	< (0.013)
VCC549	12:22:22.30	+05:40:43.0	?	< (0.024)	0.026 (0.006)	0.054 (0.009)	0.016 (0.005)	0.014 (0.003)
VCC552	12:22:27.20	+04:33:59.0	Sc	0.239 (0.040)	0.504 (0.054)	0.965 (0.091)	1.260 (0.155)	1.141 (0.199)
VCC554	12:22:24.30	+15:28:15.0	dE (d:E)	< (0.024)	< (0.015)	< (0.011)	< (0.016)	< (0.010)
VCC558	12:22:31.30	+07:07:08.0	dE (d:E)	< (0.022)	< (0.018)	< (0.014)	< (0.011)	< (0.006)
VCC559	12:22:31.30	+15:32:17.0	Sab	0.558 (0.049)	1.702 (0.126)	4.377 (0.312)	7.479 (0.901)	6.249 (0.754)
VCC560	12:22:31.60	+11:48:09.0	dE (d:E)	< (0.032)*	< (0.023)*	< (0.031)*	< (0.018)	< (0.014)
VCC561	12:22:36.30	8:48:55.00	dE (d:E)	< (0.020)	< (0.017)	< (0.015)	< (0.016)	< (0.014)
VCC562	12:22:35.90	+12:09:27.0	BCD	0.041 (0.012)	0.063 (0.013)	0.093 (0.021)	0.122 (0.027)	0.131 (0.026)
VCC563	12:22:35.50	+16:20:58.0	dE (d:E)	< (0.017)	< (0.022)	< (0.016)*	< (0.024)*	< (0.015)
VCC565	12:22:38.50	+06:00:55.0	Im (Im/S)	< (0.017)	< (0.011)	< (0.013)	< (0.014)	< (0.009)
VCC566	12:22:37.80	+08:17:46.0	Sm	< (0.026)	< (0.018)	< (0.015)	< (0.017)	< (0.013)
VCC567	12:22:39.10	+06:40:42.0	Scd	0.224 (0.027)	0.487 (0.045)	0.886 (0.076)	0.857 (0.111)	0.680 (0.092)
VCC568	12:22:39.70	+06:13:34.0	S (dS)	0.033 (0.010)	0.086 (0.014)	0.168 (0.020)	0.136 (0.023)	0.082 (0.018)
VCC570	12:22:38.50	+11:48:03.0	Sab	0.629 (0.052)	1.762 (0.132)	4.234 (0.311)	6.052 (0.733)	4.254 (0.515)
VCC571	12:22:41.10	+07:57:01.0	S0	0.019 (0.006)	0.061 (0.016)	0.111 (0.021)	0.107 (0.020)	0.043 (0.013)
VCC575	12:22:43.30	+08:11:54.0	E - E/S0	< (0.021)	< (0.018)	< (0.016)	< (0.016)	< (0.011)
VCC576	12:22:42.20	+09:19:57.0	Sbc	0.798 (0.062)	2.157 (0.158)	4.857 (0.344)	7.659 (0.925)	5.140 (0.620)
VCC583	12:22:45.10	+15:30:08.0	Im (Im/S)	< (0.022)	< (0.014)	< (0.011)	< (0.016)	< (0.010)
VCC584	12:22:48.60	+07:54:49.0	Im (Im/S)	< (0.023)	< (0.020)	< (0.009)	< (0.011)	< (0.010)
VCC585	12:22:47.50	+11:20:58.0	Im (Im/S)	< (0.021)	< (0.015)	< (0.012)	< (0.017)	< (0.011)
VCC587	12:22:48.00	+07:05:00.0	dE (d:E)	< (0.020)	< (0.021)	< (0.014)	< (0.009)	< (0.007)
VCC592	12:22:50.80	+13:35:34.0	dE (d:E)	< (0.020)	< (0.016)	< (0.013)	< (0.012)	< (0.009)
VCC593	12:22:52.80	+06:40:47.0	S (dS)	0.076 (0.017)	0.146 (0.023)	0.218 (0.029)	0.200 (0.034)	0.193 (0.032)
VCC594	12:22:51.10	+15:16:31.0	dE (d:E)	< (0.018)	< (0.016)	< (0.014)	< (0.015)	< (0.009)
VCC596	12:22:54.90	+15:49:21.0	Sc	10.144 (0.733)	28.853 (2.044)	69.484 (4.879)	112.618 (13.518)	90.336 (10.848)
VCC600	12:22:55.50	15:33:34.00	dE (d:E)	< (0.018)	< (0.023)	< (0.014)	< (0.020)	< (0.010)
VCC608	12:23:01.70	+15:54:20.0	dE (d:E)	< (0.020)	< (0.020)	< (0.016)	< (0.019)	< (0.014)
VCC611	12:23:04.80	+08:19:59.0	dE (d:E)	< (0.021)*	< (0.016)	< (0.012)	< (0.014)	< (0.010)
VCC612	12:23:05.70	+04:07:52.0	?	< (0.021)*	< (0.020)*	< (0.013)*	< (0.018)	< (0.011)
VCC613	12:23:06.20	+05:15:02.0	Sa	0.297 (0.033)	0.802 (0.068)	1.802 (0.137)	2.374 (0.300)	1.498 (0.189)
VCC615	12:23:06.00	+12:00:40.0	dE (d:E)	< (0.018)	< (0.018)	< (0.011)	< (0.013)	< (0.015)
VCC618	12:23:07.40	+13:44:40.0	Im (Im/S)	< (0.024)	< (0.020)	< (0.011)	< (0.013)	< (0.009)

OBJECT	RA h:m:s (J2000)	dec. d:m:s (J2000)	Type	S_{500} (σS_{500}) (Jy)	S_{350} (σS_{350}) (Jy)	S_{250} (σS_{250}) (Jy)	S_{160} (σS_{160}) (Jy)	S_{100} (σS_{100}) (Jy)
VCC620	12:23:09.60	+11:43:34.0	Sm	0.038 (0.007)	0.026 (0.007)	0.044 (0.012)	0.021 (0.007)	< (0.012)
VCC622	12:23:10.86	+09:01:43.8	dE (d:E)	< (0.022)	0.036 (0.007)	0.041 (0.005)	0.013 (0.004)	< (0.012)
VCC630	12:23:17.20	+11:22:05.0	Sd	0.730 (0.061)	1.719 (0.131)	3.653 (0.273)	4.610 (0.559)	2.801 (0.344)
VCC632	12:23:20.30	+07:03:58.0	dE (d:E)	< (0.017)	< (0.014)	< (0.011)	< (0.012)	< (0.007)
VCC633	12:23:20.90	7:35:34.00	dE (d:E)	< (0.018)	< (0.021)*	< (0.022)*	< (0.011)	< (0.010)
VCC634	12:23:20.00	+15:49:14.0	dE (d:E)	< (0.028)	< (0.018)	< (0.013)*	< (0.023)	< (0.018)
VCC636	12:23:21.10	+15:52:05.0	dE/dS0	< (0.018)	< (0.021)	< (0.014)	< (0.033)	< (0.012)
VCC641	12:23:28.40	+05:48:59.0	BCD	0.024 (0.005)	0.034 (0.006)	0.045 (0.011)	< (0.021)	< (0.010)
VCC648	12:23:34.90	+06:04:54.0	S0	< (0.020)	< (0.016)	< (0.014)	< (0.012)	< (0.009)
VCC651	12:23:34.60	+09:30:54.0	dE (d:E)	< (0.021)	< (0.016)	< (0.014)	< (0.013)	< (0.010)
VCC653	12:23:36.50	+07:35:47.0	dE (d:E)	< (0.016)	< (0.017)	< (0.017)	< (0.010)	< (0.009)
VCC654	12:23:35.30	+16:43:20.0	S0	< (0.024)	< (0.022)	< (0.017)	—	—
VCC656	12:23:38.70	+06:57:15.0	Sb	0.668 (0.059)	1.686 (0.126)	3.727 (0.266)	5.414 (0.653)	4.146 (0.500)
VCC657	12:23:39.00	+07:03:14.0	S0	< (0.018)	< (0.012)	< (0.010)	< (0.013)	< (0.010)*
VCC662	12:23:41.50	+02:57:40.0	Sc	0.166 (0.019)	0.396 (0.034)	0.800 (0.061)	—	—
VCC664	12:23:44.50	+12:28:42.0	Sc	0.199 (0.027)	0.425 (0.047)	0.780 (0.071)	1.074 (0.140)	0.693 (0.092)
VCC666	12:23:46.10	+16:47:29.0	Im (Im/S)	< (0.024)	< (0.018)	< (0.020)*	—	—
VCC667	12:23:48.50	+07:11:13.0	Sc	0.207 (0.025)	0.498 (0.048)	0.992 (0.078)	1.216 (0.160)	0.621 (0.082)
VCC668	12:23:47.10	+15:07:29.0	dE (d:E)	< (0.017)	< (0.014)	< (0.018)*	< (0.018)	< (0.011)
VCC669	12:23:49.90	+06:03:35.0	dE (d:E)	< (0.013)	< (0.011)	< (0.017)	< (0.011)	< (0.010)
VCC671	12:23:52.90	5:45:23.00	dE (d:E)	< (0.020)	< (0.016)	< (0.013)	< (0.016)	< (0.012)
VCC672	12:23:53.50	+07:06:26.0	S0	0.029 (0.007)	0.062 (0.006)	0.118 (0.009)	0.180 (0.027)	0.071 (0.009)
VCC674	12:23:52.70	13:52:57.00	dE (d:E)	< (0.022)	< (0.025)	< (0.017)	< (0.017)	< (0.008)
VCC675	12:23:54.20	+03:05:06.0	Sa	< (0.013)*	< (0.023)	0.027 (0.005)	—	—
VCC679	12:23:54.60	+11:29:25.0	?	< (0.023)	< (0.018)	0.016 (0.005)	< (0.014)	< (0.012)
VCC684	12:23:57.70	+12:53:14.0	dE (d:E)	< (0.023)	< (0.015)	< (0.011)	< (0.013)	< (0.008)
VCC685	12:23:57.80	+16:41:36.0	S0	0.040 (0.008)	0.119 (0.018)	0.346 (0.031)	—	—
VCC688	12:24:00.10	+07:47:06.0	Sc	0.101 (0.018)	0.306 (0.033)	0.691 (0.057)	0.937 (0.121)	0.548 (0.074)
VCC690	12:24:02.20	+05:18:45.0	S (dS)	0.070 (0.011)	0.163 (0.018)	0.338 (0.028)	0.486 (0.063)	0.485 (0.065)
VCC692	12:24:01.50	+12:12:17.0	Sc	0.294 (0.034)	0.783 (0.072)	1.677 (0.129)	2.440 (0.302)	1.649 (0.209)
VCC693	12:24:03.20	+05:10:51.0	Sm	0.027 (0.006)	0.082 (0.016)	0.161 (0.023)	0.220 (0.045)	0.078 (0.020)
VCC695	12:24:05.30	+10:04:04.0	dE (d:E)	< (0.018)	< (0.013)	< (0.010)	< (0.017)	< (0.009)
VCC697	12:24:05.50	+07:02:29.0	Sc	0.133 (0.020)	0.359 (0.037)	0.799 (0.064)	1.051 (0.136)	0.619 (0.084)
VCC698	12:24:05.00	+11:13:05.0	S0	< (0.020)	< (0.018)*	< (0.011)	< (0.014)	< (0.013)
VCC699	12:24:07.40	+06:36:27.0	Pec	0.173 (0.023)	0.395 (0.040)	0.808 (0.067)	1.259 (0.158)	1.330 (0.164)
VCC705	12:24:11.09	+11:56:47.5	dE (d:E)	< (0.021)*	< (0.018)*	< (0.029)*	< (0.015)	< (0.012)
VCC706	12:24:12.50	+11:31:46.0	dE (d:E)	< (0.021)	< (0.016)	< (0.013)	< (0.015)	< (0.012)
VCC710	12:24:14.50	+04:13:33.0	dS0	0.041 (0.012)	0.087 (0.016)	0.115 (0.015)	0.111 (0.022)	0.101 (0.018)
VCC711	12:24:13.80	+07:10:30.0	dE (d:E)	< (0.019)	< (0.019)	< (0.012)	< (0.011)	< (0.008)
VCC713	12:24:14.50	+08:32:09.0	Sc	0.219 (0.025)	0.599 (0.052)	1.369 (0.101)	1.905 (0.234)	1.503 (0.190)
VCC723	12:24:22.00	+13:01:47.0	dS0	< (0.018)	< (0.015)	< (0.017)	< (0.009)	< (0.011)
VCC725	12:24:24.60	+15:04:33.0	dE (d:E)	< (0.024)	< (0.014)	< (0.011)	< (0.015)	< (0.012)
VCC731	12:24:28.20	+07:19:03.0	E - E/S0	< (0.023)*	< (0.051)*	< (0.075)*	< (0.013)	< (0.010)
VCC734	12:24:33.60	+06:42:44.0	Sbc	0.067 (0.019)	0.124 (0.017)	0.196 (0.024)	0.253 (0.040)	0.184 (0.030)
VCC737	12:24:39.40	+03:59:44.0	S/BCD	0.055 (0.014)	0.114 (0.020)	0.178 (0.023)	0.205 (0.038)	0.107 (0.022)
VCC739	12:24:40.00	+03:18:10.0	Sd	0.117 (0.025)	0.250 (0.040)	0.355 (0.038)	0.641 (0.116)	0.315 (0.062)
VCC740	12:24:40.20	+08:30:18.0	Sm	< (0.019)	< (0.019)	< (0.019)*	< (0.019)	< (0.010)
VCC741	12:24:41.30	+03:43:17.0	BCD	0.023 (0.008)	0.041 (0.009)	0.065 (0.014)	0.089 (0.023)	0.097 (0.023)
VCC745	12:24:47.00	+07:21:11.0	dE (d:E)	< (0.015)	< (0.020)*	< (0.029)*	< (0.022)*	< (0.007)
VCC746	12:24:47.70	+08:26:17.0	dE (d:E)	< (0.017)	< (0.018)	< (0.015)	< (0.019)	< (0.012)
VCC747	12:24:47.80	+08:59:29.0	dE (d:E)	< (0.018)	< (0.026)*	< (0.020)*	< (0.017)	< (0.011)
VCC748	12:24:47.50	+14:34:34.0	dE (d:E)	< (0.034)	< (0.020)	< (0.026)*	< (0.019)	< (0.013)
VCC750	12:24:49.50	+06:45:34.0	dE (d:E)	< (0.017)	< (0.016)	< (0.013)	< (0.011)	< (0.008)
VCC755	12:24:54.10	+07:33:24.0	dE (d:E)	< (0.018)	< (0.021)	< (0.014)	< (0.013)	< (0.010)
VCC756	12:24:53.10	+09:29:37.0	dE (d:E)	< (0.015)	< (0.017)	< (0.011)	< (0.011)	< (0.007)
VCC758	12:24:54.90	+07:26:40.0	S0	0.279 (0.026)	0.815 (0.063)	2.059 (0.148)	3.452 (0.415)	3.027 (0.366)
VCC759	12:24:55.40	+11:42:15.0	S0	< (0.016)	< (0.019)	< (0.019)	< (0.015)	< (0.016)*
VCC760	12:24:56.10	+11:49:55.0	dE (d:E)	< (0.020)*	< (0.028)*	< (0.020)*	< (0.016)	< (0.010)

OBJECT	RA h:m:s (J2000)	dec. d:m:s (J2000)	Type	S_{500} (σS_{500}) (Jy)	S_{350} (σS_{350}) (Jy)	S_{250} (σS_{250}) (Jy)	S_{160} (σS_{160}) (Jy)	S_{100} (σS_{100}) (Jy)
VCC762	12:25:03.00	+07:30:14.0	dE (d:E)	< (0.016)	< (0.016)	< (0.012)	< (0.011)	< (0.010)
VCC763	12:25:03.70	+12:53:13.0	E - E/S0	0.123 (0.011)	0.136 (0.011)	0.233 (0.017)	0.737 (0.098)	0.950 (0.121)
VCC764	12:25:05.60	+05:19:45.0	S0	< (0.016)	0.030 (0.008)	0.064 (0.012)	0.124 (0.029)	0.063 (0.013)
VCC765	12:25:03.50	+13:14:41.0	dE (d:E)	< (0.022)	< (0.019)	< (0.014)	< (0.012)	< (0.008)
VCC769	12:25:05.40	+15:42:35.0	dE (d:E)	< (0.023)	< (0.027)	< (0.019)	< (0.039)	< (0.030)
VCC771	12:25:07.80	6:05:47.00	dE (d:E)	< (0.017)	< (0.015)	< (0.012)	< (0.015)	< (0.008)
VCC772	12:25:08.70	+04:24:51.0	BCD	< (0.020)	< (0.019)	< (0.016)*	< (0.021)*	< (0.010)
VCC777	12:25:11.30	14:26:29.00	dE (d:E)	< (0.019)	< (0.018)*	< (0.017)*	< (0.015)	< (0.012)
VCC778	12:25:12.30	+14:45:44.0	S0	< (0.056)*	< (0.130)*	< (0.272)*	< (0.131)*	< (0.029)*
VCC779	12:25:13.10	+13:01:32.0	dE (d:E)	< (0.013)	< (0.022)	< (0.014)	< (0.011)	< (0.007)
VCC781	12:25:15.20	+12:42:53.0	dS0	0.019 (0.005)	0.045 (0.012)	0.078 (0.014)	0.115 (0.022)	0.087 (0.021)
VCC784	12:25:14.70	+15:36:27.0	S0	< (0.023)	< (0.018)	< (0.012)	< (0.059)	< (0.027)
VCC785	12:25:18.10	+04:55:30.0	Sa	0.566 (0.059)	1.442 (0.117)	3.029 (0.226)	2.998 (0.384)	1.205 (0.176)
VCC786	12:25:14.50	+11:50:59.0	dE (d:E)	< (0.015)	< (0.018)	< (0.015)	< (0.015)	< (0.013)
VCC787	12:25:18.00	+05:44:28.0	Scd	0.233 (0.025)	0.562 (0.049)	1.178 (0.090)	1.689 (0.207)	1.514 (0.193)
VCC788	12:25:16.80	+11:36:20.0	dE (d:E)	< (0.018)	0.018 (0.005)	0.019 (0.005)	< (0.013)	< (0.011)
VCC790	12:25:17.60	+14:10:23.0	dE (d:E)	< (0.060)	< (0.015)	< (0.015)	< (0.016)	< (0.008)
VCC791	12:25:22.70	+06:42:41.0	dE (d:E)	< (0.019)	< (0.014)	< (0.009)	< (0.010)	< (0.007)
VCC792	12:25:22.20	+10:01:01.0	Sab	0.815 (0.068)	2.223 (0.165)	4.953 (0.353)	6.104 (0.739)	3.096 (0.381)
VCC793	12:25:21.30	+13:04:14.0	Im (Im/S)	< (0.026)	< (0.016)	0.016 (0.004)	< (0.012)	< (0.008)
VCC795	12:25:23.10	14:48:11.00	dE (d:E)	< (0.018)	< (0.018)	< (0.015)	< (0.021)	< (0.014)
VCC802	12:25:28.70	+13:29:50.0	BCD	< (0.024)	0.025 (0.006)	0.031 (0.005)	< (0.012)	< (0.007)
VCC803	12:25:29.80	12:29:41.00	dE (d:E)	< (0.015)	< (0.013)	< (0.009)	< (0.014)	< (0.013)
VCC809	12:25:33.10	+12:15:37.0	Sc	0.178 (0.023)	0.360 (0.034)	0.602 (0.050)	0.583 (0.082)	0.266 (0.042)
VCC810	12:25:33.60	+13:13:37.0	dE (d:E)	< (0.019)	< (0.024)	< (0.016)	< (0.011)	< (0.007)
VCC811	12:25:36.00	+10:15:05.0	dIm/dE	< (0.018)	< (0.018)	< (0.014)	< (0.009)	< (0.007)
VCC812	12:25:34.80	+15:11:39.0	dE (d:E)	< (0.023)	< (0.012)	< (0.015)	< (0.041)	< (0.029)
VCC815	12:25:37.10	+13:08:36.0	dE (d:E)	< (0.034)*	< (0.032)*	< (0.032)*	< (0.011)	< (0.007)
VCC816	12:25:36.10	+15:50:51.0	dE (d:E)	< (0.026)*	< (0.023)*	< (0.017)*	—	—
VCC817	12:25:36.40	+15:49:47.0	dE (d:E)	< (0.025)	< (0.017)	< (0.011)	—	—
VCC820	12:25:38.80	+07:43:56.0	dE (d:E)	< (0.021)	< (0.014)	< (0.010)	< (0.017)	< (0.010)
VCC823	12:25:38.90	+12:18:50.0	dE (d:E)	< (0.022)*	< (0.027)*	< (0.024)*	< (0.016)	< (0.016)
VCC824	12:25:39.10	14:08:54.00	dE (d:E)	< (0.038)*	< (0.042)*	< (0.029)*	< (0.016)	< (0.010)
VCC825	12:25:39.30	+10:35:02.0	Im (Im/S)	< (0.019)	0.020 (0.005)	0.034 (0.005)	< (0.015)	< (0.011)
VCC827	12:25:42.60	+07:13:00.0	Sc	1.044 (0.082)	2.412 (0.174)	4.798 (0.342)	7.057 (0.851)	5.183 (0.627)
VCC828	12:25:41.70	+12:48:38.0	E - E/S0	< (0.018)	< (0.014)	< (0.011)	< (0.014)	< (0.009)
VCC833	12:25:44.60	+13:01:20.0	dE (d:E)	< (0.023)	< (0.019)	< (0.012)	< (0.015)	< (0.008)
VCC834	12:25:46.70	+04:30:35.0	Sc	0.160 (0.022)	0.320 (0.032)	0.623 (0.054)	0.745 (0.099)	0.550 (0.077)
VCC836	12:25:46.70	+12:39:44.0	Sab	1.400 (0.107)	3.635 (0.260)	9.334 (0.665)	17.325 (2.081)	18.565 (2.233)
VCC839	12:25:47.50	+10:05:35.0	dE (d:E)	< (0.017)	< (0.016)	< (0.011)	< (0.012)	< (0.008)
VCC841	12:25:47.40	+14:57:09.0	BCD	0.020 (0.006)	0.061 (0.011)	0.132 (0.017)	0.191 (0.041)	0.171 (0.039)
VCC846	12:25:50.30	+13:11:52.0	dE (d:E)	< (0.020)	< (0.022)	< (0.016)	< (0.010)	< (0.008)
VCC848	12:25:52.50	+05:48:36.0	Im/BCD	0.032 (0.005)	0.049 (0.013)	0.099 (0.017)	0.099 (0.024)	0.158 (0.028)
VCC849	12:25:50.70	+10:27:33.0	Sbc	0.401 (0.040)	0.926 (0.078)	1.882 (0.142)	2.483 (0.305)	2.118 (0.261)
VCC851	12:25:54.10	+07:33:17.0	Sc	0.372 (0.034)	0.872 (0.068)	1.791 (0.131)	2.521 (0.308)	1.806 (0.223)
VCC854	12:25:55.70	+12:46:11.0	dE (d:E)	< (0.019)	< (0.017)	< (0.014)	< (0.012)	< (0.010)
VCC855	12:25:56.20	+07:14:05.0	dE (d:E)	< (0.019)	< (0.021)	< (0.013)	< (0.012)	< (0.009)
VCC856	12:25:57.90	+10:03:14.0	dE (d:E)	< (0.016)	< (0.018)	< (0.012)	< (0.010)	< (0.007)
VCC859	12:25:58.30	+03:25:49.0	Sc	0.605 (0.052)	1.297 (0.097)	2.500 (0.179)	2.869 (0.360)	1.876 (0.240)
VCC861	12:25:58.90	+15:16:38.0	dE (d:E)	< (0.026)*	< (0.048)*	< (0.046)*	< (0.053)*	< (0.028)*
VCC862	12:26:00.40	7:27:24.00	dE (d:E)	< (0.020)	< (0.015)	< (0.015)	< (0.013)	< (0.009)
VCC863	12:25:59.70	14:02:22.00	dE (d:E)	< (0.025)	< (0.024)	< (0.017)	< (0.013)	< (0.008)
VCC865	12:25:58.80	+15:40:17.0	Sc	0.886 (0.071)	2.026 (0.150)	3.559 (0.255)	—	—
VCC869	12:26:05.90	+08:58:03.0	dIm/dE	< (0.021)	< (0.020)	< (0.013)	< (0.026)	< (0.010)
VCC871	12:26:05.60	+12:33:35.0	dE (d:E)	< (0.017)	< (0.014)	< (0.010)	< (0.013)	< (0.009)
VCC872	12:26:06.70	+12:51:39.0	dE (d:E)	< (0.023)*	< (0.031)*	< (0.014)	< (0.016)	< (0.009)
VCC873	12:26:07.50	+13:06:46.0	Sc	2.242 (0.163)	6.229 (0.440)	15.011 (1.057)	24.233 (2.912)	18.245 (2.192)
VCC877	12:26:09.60	+13:40:24.0	dE (d:E)	< (0.035)*	< (0.019)	< (0.016)	< (0.009)	< (0.008)

OBJECT	RA h:m:s (J2000)	dec. d:m:s (J2000)	Type	S_{500} (σS_{500}) (Jy)	S_{350} (σS_{350}) (Jy)	S_{250} (σS_{250}) (Jy)	S_{160} (σS_{160}) (Jy)	S_{100} (σS_{100}) (Jy)
VCC878	12:26:10.00	+14:55:45.0	dE (d:E)	< (0.020)	< (0.019)	< (0.014)	< (0.049)	< (0.029)
VCC881N	12:26:12.13	+12:57:45.5	E - E/S0	0.027 (0.008)	0.034 (0.009)	0.034 (0.010)	< (0.014)	< (0.009)
VCC881SE+off	12:26:12.51	+12:55:41.8	E - E/S0	0.163 (0.040)	0.360 (0.052)	0.625 (0.091)	0.503 (0.103)	< (0.008)
VCC882	12:26:15.00	+12:57:51.0	dE (d:E)	< (0.020)*	< (0.020)	< (0.012)*	< (0.015)	< (0.008)
VCC888	12:26:18.50	+08:20:59.0	Im (Im/S)	0.044 (0.012)	0.061 (0.015)	0.086 (0.019)	0.065 (0.023)	0.067 (0.023)
VCC890	12:26:21.50	+06:40:10.0	BCD	< (0.019)	0.021 (0.005)	0.024 (0.005)	0.049 (0.014)	0.042 (0.010)
VCC896	12:26:22.50	+12:47:00.0	dE (d:E)	< (0.020)	< (0.012)	< (0.014)	< (0.020)	< (0.009)
VCC905	12:26:30.10	+08:52:20.0	Sc	0.300 (0.043)	0.604 (0.065)	1.193 (0.108)	1.395 (0.188)	0.863 (0.126)
VCC912	12:26:32.20	+12:36:40.0	Sbc	0.453 (0.042)	1.176 (0.090)	2.598 (0.191)	3.801 (0.461)	2.773 (0.342)
VCC916	12:26:33.20	+12:44:35.0	dE (d:E)	< (0.020)	< (0.015)	< (0.014)	< (0.016)	< (0.010)
VCC917	12:26:32.40	+13:34:43.0	dE (d:E)	< (0.018)	< (0.015)	< (0.011)	< (0.014)	< (0.008)
VCC920	12:26:34.80	+09:58:54.0	dE (d:E)	< (0.019)	< (0.018)*	< (0.014)	< (0.010)	< (0.008)
VCC921	12:26:36.10	+03:57:53.0	Sbc	0.390 (0.036)	1.155 (0.088)	2.978 (0.213)	5.730 (0.689)	5.719 (0.692)
VCC926	12:26:39.10	+09:29:48.0	dE (d:E)	< (0.017)	< (0.014)	< (0.013)	< (0.012)	< (0.008)
VCC928	12:26:39.60	+12:30:48.0	dE (d:E)	< (0.017)	< (0.017)	< (0.014)	< (0.017)	< (0.012)
VCC929	12:26:40.50	+08:26:08.0	dE (d:E)	< (0.019)	< (0.017)	< (0.013)	< (0.014)	< (0.013)
VCC930	12:26:40.40	12:50:36.00	dE (d:E)	< (0.019)	< (0.010)	< (0.009)	< (0.014)	< (0.007)
VCC931	12:26:44.00	+10:54:17.0	dE (d:E)	< (0.022)*	< (0.015)	< (0.013)	< (0.012)	< (0.009)
VCC933	12:26:44.30	+08:49:25.0	dE (d:E)	< (0.023)*	< (0.020)*	< (0.017)*	< (0.018)	< (0.010)
VCC936	12:26:44.40	+11:22:47.0	dE (d:E)	< (0.036)*	< (0.033)*	< (0.023)	< (0.019)	< (0.010)
VCC938	12:26:46.70	+07:55:08.0	Sc	0.390 (0.038)	1.123 (0.090)	2.524 (0.184)	3.700 (0.452)	2.880 (0.360)
VCC939	12:26:47.20	+08:53:05.0	Sc	0.618 (0.069)	1.239 (0.120)	2.250 (0.184)	2.232 (0.288)	1.420 (0.194)
VCC940	12:26:47.10	+12:27:14.0	dE (d:E)	< (0.027)*	< (0.029)*	< (0.018)*	< (0.017)	< (0.012)
VCC944	12:26:50.60	+09:35:03.0	S0	< (0.020)	< (0.020)*	< (0.032)*	< (0.015)*	< (0.011)*
VCC945	12:26:51.10	+13:10:33.0	Sm	< (0.022)	< (0.016)*	< (0.013)	< (0.010)	< (0.008)
VCC949	12:26:54.50	+10:39:57.0	dE (d:E)	< (0.018)	< (0.016)*	< (0.018)*	< (0.010)	< (0.008)
VCC950	12:26:50.50	+11:33:33.0	Sm	< (0.034)	< (0.025)	< (0.018)	< (0.016)	< (0.011)
VCC951	12:26:54.30	+11:39:50.0	dE/dS0	< (0.022)	0.043 (0.011)	0.089 (0.016)	0.081 (0.020)	< (0.015)
VCC952	12:26:55.70	+09:52:56.0	Im (Im/S)	< (0.017)	< (0.015)	< (0.010)	< (0.010)	< (0.007)
VCC953	12:26:54.60	+13:33:57.0	dE (d:E)	< (0.022)	< (0.020)	< (0.014)	< (0.013)	< (0.008)
VCC954	12:26:56.90	+05:58:12.0	dE (d:E)	< (0.019)	< (0.013)*	< (0.010)*	< (0.014)	< (0.009)
VCC958	12:26:56.40	+15:02:51.0	Sa	1.074 (0.079)	3.433 (0.244)	8.283 (0.582)	—	—
VCC962	12:26:59.70	+12:30:00.0	dE (d:E)	< (0.020)	< (0.013)	< (0.009)	< (0.022)	< (0.010)
VCC963	12:26:59.00	+14:46:56.0	Im (Im/S)	< (0.025)	< (0.018)	< (0.020)	—	—
VCC965	12:27:03.10	+12:33:39.0	dE (d:E)	< (0.020)	< (0.015)	< (0.010)	< (0.020)	< (0.013)
VCC971	12:27:09.00	+05:52:49.0	Sd	0.316 (0.037)	0.566 (0.048)	1.015 (0.078)	1.313 (0.167)	1.039 (0.136)
VCC974	12:27:09.90	+08:23:23.0	dE (d:E)	< (0.017)	< (0.015)	< (0.012)	< (0.012)	< (0.012)
VCC975	12:27:11.10	+07:15:47.0	Scd	0.433 (0.052)	0.769 (0.077)	1.121 (0.102)	1.093 (0.178)	< (0.015)
VCC977	12:27:11.10	+12:02:18.0	dE (d:E)	< (0.020)	< (0.017)	< (0.017)	< (0.013)	< (0.012)
VCC979	12:27:11.60	+09:25:14.0	Sa	0.350 (0.033)	1.034 (0.081)	2.716 (0.198)	5.048 (0.610)	6.038 (0.734)
VCC983	12:27:14.40	9:37:12.00	dE (d:E)	< (0.020)	< (0.016)	< (0.007)	< (0.012)	< (0.009)
VCC984	12:27:13.30	+12:44:05.0	Sa	< (0.018)	< (0.014)	< (0.008)	< (0.011)	< (0.010)
VCC985	12:27:15.80	+04:15:48.0	BCD	< (0.018)	< (0.016)	0.029 (0.004)	0.019 (0.006)	0.015 (0.003)
VCC989	12:27:17.40	+07:40:12.0	Sc	< (0.020)	< (0.014)	< (0.016)*	< (0.017)	< (0.013)
VCC991	12:27:17.70	+14:08:49.0	dE (d:E)	< (0.018)	< (0.015)	< (0.016)	< (0.017)	< (0.012)
VCC992	12:27:18.60	+08:12:45.0	dE (d:E)	< (0.026)*	< (0.018)	< (0.015)	< (0.022)	< (0.013)
VCC995	12:27:22.20	+10:52:00.0	Sc	0.039 (0.010)	0.089 (0.016)	0.148 (0.021)	0.111 (0.027)	0.061 (0.019)
VCC997	12:27:22.50	+12:04:00.0	dE (d:E)	< (0.021)	< (0.020)*	< (0.019)*	< (0.017)	< (0.010)
VCC1001	12:27:24.50	+13:42:58.0	Im (Im/S)	< (0.028)*	< (0.025)*	< (0.020)*	< (0.014)	< (0.009)
VCC1002	12:27:26.40	+06:15:46.0	Sc	0.689 (0.060)	1.838 (0.139)	4.111 (0.293)	6.014 (0.731)	3.906 (0.481)
VCC1003	12:27:26.50	+11:06:27.0	S0a - S0/Sa	0.225 (0.017)	0.747 (0.058)	2.220 (0.166)	4.399 (0.530)	4.409 (0.534)
VCC1005	12:27:25.40	+13:45:02.0	dE (d:E)	< (0.021)	< (0.025)	< (0.022)*	< (0.021)*	< (0.008)
VCC1010	12:27:27.30	+12:17:25.0	dS0	< (0.020)	< (0.014)	< (0.013)	< (0.017)	< (0.011)
VCC1011	12:27:29.20	+07:38:38.0	Sdm - Sd/Sm	0.059 (0.011)	0.139 (0.023)	0.213 (0.028)	0.118 (0.032)	< (0.012)
VCC1013	12:27:30.20	+09:20:28.0	Im (Im/S)	< (0.023)*	< (0.025)*	< (0.019)*	< (0.014)	< (0.009)
VCC1017	12:27:31.50	+09:36:05.0	Im (Im/S)	< (0.019)	< (0.016)	< (0.013)	< (0.015)	< (0.009)
VCC1020	12:27:32.00	+11:36:55.0	dIm/dE	< (0.024)	< (0.016)*	< (0.012)	< (0.019)	< (0.010)
VCC1021	12:27:33.40	+10:00:14.0	Im (Im/S)	< (0.018)	< (0.017)	0.030 (0.005)	0.011 (0.004)	< (0.007)

OBJECT	RA h:m:s (J2000)	dec. d:m:s (J2000)	Type	S_{500} (σS_{500}) (Jy)	S_{350} (σS_{350}) (Jy)	S_{250} (σS_{250}) (Jy)	S_{160} (σS_{160}) (Jy)	S_{100} (σS_{100}) (Jy)
VCC1025	12:27:36.70	+08:09:16.0	E - E/S0	< (0.020)	< (0.019)	< (0.013)	< (0.016)	< (0.010)
VCC1028	12:27:37.30	+14:27:22.0	dS0	< (0.014)	< (0.020)*	< (0.015)*	< (0.050)	< (0.033)
VCC1030	12:27:40.50	+13:04:44.0	S0	0.273 (0.027)	0.792 (0.068)	2.002 (0.150)	3.709 (0.448)	4.215 (0.508)
VCC1035	12:27:42.10	+12:05:22.0	E - E/S0	< (0.017)	< (0.018)	< (0.018)*	< (0.020)	< (0.010)
VCC1036	12:27:41.20	+12:18:57.0	dE/dS0	< (0.021)	< (0.015)	< (0.013)	< (0.013)	< (0.013)
VCC1039	12:27:44.30	+11:12:52.0	dE (d:E)	< (0.024)	< (0.021)	< (0.018)	< (0.016)	< (0.011)
VCC1040	12:27:44.50	+12:58:55.0	dE (d:E)	< (0.094)*	< (0.102)*	< (0.096)*	< (0.011)	< (0.012)
VCC1043	12:27:45.60	+13:00:32.0	Sb	1.388 (0.127)	3.748 (0.285)	8.677 (0.630)	13.133 (1.583)	10.396 (1.250)
VCC1044	12:27:46.00	+11:26:07.0	dE (d:E)	< (0.022)	< (0.017)	< (0.016)	< (0.015)	< (0.011)
VCC1047	12:27:53.60	+12:17:36.0	Sa	< (0.019)	< (0.017)	< (0.013)	< (0.013)	< (0.012)
VCC1048	12:27:55.40	+05:43:16.0	Scd	0.156 (0.020)	0.371 (0.034)	0.737 (0.058)	1.084 (0.137)	0.833 (0.108)
VCC1049	12:27:54.80	+08:05:26.0	S0	< (0.020)	< (0.017)	< (0.022)*	< (0.018)	< (0.013)
VCC1052	12:27:55.40	+12:22:07.0	dE (d:E)	< (0.018)	< (0.015)	< (0.014)	< (0.016)	< (0.010)
VCC1059	12:28:00.40	11:56:59.00	dE (d:E)	< (0.020)	< (0.016)	< (0.018)	< (0.021)	< (0.010)
VCC1058	12:28:01.40	+04:17:29.0	S (dS)	< (0.021)	0.063 (0.011)	0.122 (0.015)	0.196 (0.031)	0.139 (0.024)
VCC1062	12:28:03.90	+09:48:13.0	S0	< (0.026)	< (0.017)*	< (0.012)	< (0.012)	< (0.010)
VCC1064	12:28:04.90	+13:36:43.0	dE (d:E)	< (0.024)	< (0.019)	< (0.015)	< (0.131)	< (0.010)
VCC1065	12:28:04.80	+13:34:42.0	dE (d:E)	< (0.018)	< (0.016)	< (0.016)	< (0.026)	< (0.010)
VCC1069	12:28:06.50	+12:53:53.0	dE (d:E)	< (0.021)	< (0.022)	< (0.015)	< (0.014)	< (0.011)
VCC1073	12:28:08.60	+12:05:36.0	dE (d:E)	< (0.018)	< (0.017)	< (0.013)*	< (0.015)	< (0.013)
VCC1075	12:28:12.30	+10:17:52.0	dE (d:E)	< (0.023)	< (0.016)	< (0.012)	< (0.011)	< (0.008)
VCC1076	12:28:12.80	+10:31:34.0	dE (d:E)	< (0.021)	< (0.024)	< (0.017)	< (0.008)	< (0.009)
VCC1078	12:28:11.30	+09:45:37.0	dE (d:E)	< (0.026)	< (0.020)*	< (0.018)*	< (0.013)	< (0.011)
VCC1079	12:28:12.00	+10:21:55.0	dE (d:E)	< (0.024)	< (0.017)	< (0.013)	< (0.014)	< (0.009)
VCC1086	12:28:15.90	+09:26:11.0	S (dS)	0.213 (0.024)	0.624 (0.050)	1.420 (0.104)	1.989 (0.243)	1.092 (0.136)
VCC1087	12:28:14.90	+11:47:23.0	dE (d:E)	< (0.018)	< (0.017)	< (0.016)	< (0.016)	< (0.012)
VCC1089	12:28:16.60	+10:52:07.0	dE (d:E)	< (0.023)	< (0.015)	< (0.013)	< (0.013)	< (0.010)
VCC1091	12:28:18.80	+08:43:46.0	Sbc	0.150 (0.020)	0.329 (0.033)	0.667 (0.055)	0.912 (0.120)	0.764 (0.101)
VCC1092	12:28:19.90	+09:10:07.0	dE (d:E)	< (0.019)	< (0.019)	< (0.016)	< (0.016)	< (0.009)
VCC1093	12:28:18.70	+11:42:01.0	dE (d:E)	< (0.020)	< (0.020)	< (0.017)	< (0.017)	< (0.010)
VCC1094	12:28:20.90	+06:11:43.0	?	< (0.020)	< (0.015)	< (0.011)	< (0.017)	< (0.010)
VCC1095	12:28:21.20	+08:00:43.0	dE (d:E)	< (0.024)	< (0.014)	< (0.011)	< (0.016)	< (0.012)
VCC1099	12:28:24.00	+11:25:14.0	dE (d:E)	< (0.017)	< (0.017)	< (0.014)	< (0.017)	< (0.014)
VCC1101	12:28:23.70	+13:11:45.0	dE (d:E)	< (0.021)	< (0.020)	< (0.012)*	< (0.014)	< (0.011)
VCC1102	12:28:27.20	+06:56:46.0	Im (Im/S)	< (0.022)	< (0.017)	< (0.010)	< (0.017)	< (0.012)
VCC1104	12:28:28.00	+12:49:25.0	dE (d:E)	< (0.020)	< (0.019)	< (0.013)	< (0.014)	< (0.011)
VCC1105	12:28:27.20	+14:09:21.0	dE (d:E)	< (0.019)	< (0.019)	< (0.017)	< (0.020)	< (0.011)
VCC1107	12:28:30.50	+07:19:30.0	dE (d:E)	< (0.021)	< (0.018)	< (0.012)	< (0.017)	< (0.010)
VCC1114	12:28:33.80	+08:38:23.0	Im (Im/S)	< (0.019)	< (0.017)	< (0.020)*	< (0.018)	< (0.015)
VCC1115	12:28:33.30	+11:44:37.0	dE (d:E)	< (0.022)*	< (0.021)	< (0.017)	< (0.016)	< (0.014)
VCC1118	12:28:40.50	+09:15:32.0	Sc	0.339 (0.032)	0.941 (0.075)	2.378 (0.171)	4.300 (0.519)	4.270 (0.515)
VCC1120	12:28:42.20	+07:48:19.0	dE (d:E)	< (0.017)	< (0.013)	< (0.012)	< (0.012)	< (0.010)
VCC1121	12:28:41.80	+11:07:55.0	Im (Im/S)	< (0.020)	< (0.016)	< (0.016)	< (0.019)	< (0.010)
VCC1122	12:28:41.70	+12:54:57.0	dE (d:E)	< (0.021)	< (0.017)	< (0.015)*	< (0.017)	< (0.012)
VCC1123	12:28:42.60	+12:32:59.0	dE (d:E)	< (0.020)	< (0.017)	< (0.013)	< (0.014)	< (0.011)
VCC1124	12:28:43.60	+10:51:37.0	dE (d:E)	< (0.023)	< (0.015)	< (0.012)	< (0.010)	< (0.008)
VCC1125	12:28:43.30	+11:45:18.0	S0	< (0.021)*	< (0.018)	< (0.014)	< (0.021)	< (0.016)
VCC1128	12:28:45.00	+09:03:19.0	Im (Im/S)	< (0.014)	< (0.013)	< (0.012)	< (0.014)	< (0.010)
VCC1129	12:28:44.90	+12:48:35.0	dE (d:E)	< (0.017)	< (0.017)	< (0.015)*	< (0.014)	< (0.011)
VCC1137	12:28:50.90	+14:09:25.0	dE (d:E)	< (0.019)	< (0.015)	< (0.013)	< (0.014)	< (0.012)
VCC1141	12:28:54.90	+09:25:16.0	BCD	< (0.018)	< (0.026)*	0.049 (0.015)	0.022 (0.005)	0.017 (0.004)
VCC1145	12:28:59.00	+03:34:14.0	Sb	< (0.024)	< (0.815)	< (1.809)	—	—
VCC1146	12:28:57.50	+13:14:31.0	E - E/S0	< (0.021)	< (0.016)	< (0.010)	< (0.015)	< (0.013)
VCC1148	12:28:58.10	+12:39:42.0	E - E/S0	< (0.023)*	< (0.031)*	< (0.028)*	< (0.015)*	< (0.011)
VCC1149	12:28:59.00	+12:54:28.0	dE (d:E)	< (0.016)	< (0.013)	< (0.011)	< (0.015)	< (0.010)
VCC1151	12:28:59.70	+07:31:37.0	dE (d:E)	< (0.020)	< (0.021)	< (0.012)	< (0.016)	< (0.012)
VCC1153	12:28:59.80	+12:38:55.0	dE (d:E)	< (0.015)	< (0.011)	< (0.012)	< (0.013)	< (0.011)
VCC1154	12:29:00.00	+13:58:43.0	S0	0.205 (0.022)	0.655 (0.058)	1.818 (0.132)	3.753 (0.455)	4.424 (0.535)

OBJECT	RA h:m:s (J2000)	dec. d:m:s (J2000)	Type	S_{500} (σS_{500}) (Jy)	S_{350} (σS_{350}) (Jy)	S_{250} (σS_{250}) (Jy)	S_{160} (σS_{160}) (Jy)	S_{100} (σS_{100}) (Jy)
VCC1158	12:29:03.00	+13:11:02.0	Sa	< (0.021)	< (0.018)	< (0.011)	< (0.014)	< (0.012)
VCC1163	12:29:06.40	+14:00:15.0	dE (d:E)	< (0.019)	< (0.019)	< (0.017)	< (0.018)	< (0.014)
VCC1164	12:29:08.10	+09:26:38.0	dE (d:E)	< (0.021)*	< (0.018)*	< (0.014)*	< (0.020)	< (0.010)
VCC1165	12:29:10.20	+09:16:01.0	dIm/dE	< (0.022)	< (0.020)	< (0.015)	< (0.015)	< (0.011)
VCC1167	12:29:12.20	+07:52:43.0	dE (d:E)	< (0.021)	< (0.018)	< (0.014)	< (0.015)	< (0.013)
VCC1172	12:29:15.30	+08:48:52.0	dE (d:E)	< (0.018)	< (0.014)	< (0.014)*	< (0.018)	< (0.011)
VCC1173	12:29:14.80	+12:58:42.0	dE (d:E)	< (0.018)	< (0.017)	< (0.011)	< (0.018)	< (0.009)
VCC1175	12:29:18.20	+10:08:09.0	E - E/S0	< (0.021)	< (0.019)	0.031 (0.009)	0.015 (0.004)	0.016 (0.003)
VCC1178	12:29:21.30	+08:09:24.0	E - E/S0	< (0.021)	< (0.022)	< (0.015)	< (0.013)	< (0.012)
VCC1179	12:29:22.60	+09:59:21.0	Im/BCD	0.027 (0.007)	0.029 (0.005)	0.059 (0.011)	0.052 (0.012)	0.042 (0.011)
VCC1183	12:29:22.50	+11:26:02.0	dS0	< (0.025)	< (0.016)	< (0.013)	< (0.015)	< (0.012)
VCC1185	12:29:23.50	+12:27:02.0	dE (d:E)	< (0.019)	< (0.012)	< (0.012)	< (0.013)	< (0.012)*
VCC1189	12:29:28.80	+06:46:18.0	Sc	0.187 (0.023)	0.408 (0.040)	0.782 (0.082)	0.947 (0.129)	0.477 (0.073)
VCC1190	12:29:28.00	+08:45:00.0	Sa	0.300 (0.031)	0.875 (0.068)	2.165 (0.158)	3.615 (0.438)	3.110 (0.377)
VCC1191	12:29:28.70	+12:29:47.0	dE (d:E)	< (0.022)	< (0.014)	< (0.013)	< (0.015)	< (0.011)
VCC1192	12:29:30.20	+07:59:34.0	E - E/S0	< (0.016)	< (0.018)	< (0.012)	< (0.018)	< (0.010)
VCC1193	12:29:30.60	+07:41:48.0	Sc	0.227 (0.029)	0.450 (0.039)	0.866 (0.067)	1.172 (0.148)	0.877 (0.112)
VCC1196	12:29:30.90	+14:02:57.0	S0a - S0/Sa	< (0.015)	< (0.025)	< (0.015)	< (0.014)	< (0.013)
VCC1198	12:29:31.90	+13:30:36.0	dE (d:E)	< (0.017)	< (0.016)	< (0.013)*	< (0.017)	< (0.012)
VCC1199	12:29:35.00	+08:03:29.0	E - E/S0	< (0.022)	< (0.029)*	< (0.042)*	< (0.015)	< (0.013)
VCC1200	12:29:35.20	+10:47:35.0	Im (Im/S)	0.021 (0.006)	0.040 (0.010)	0.064 (0.013)	0.039 (0.012)	0.012 (0.003)
VCC1203	12:29:37.10	+07:55:58.0	S0	< (0.020)	< (0.024)*	< (0.025)*	< (0.017)	< (0.009)
VCC1204	12:29:38.00	+07:06:23.0	dE (d:E)	< (0.019)	< (0.025)	< (0.010)	< (0.015)	< (0.014)
VCC1205	12:29:37.80	+07:49:27.0	Sc	0.405 (0.038)	1.085 (0.084)	2.627 (0.190)	4.570 (0.553)	4.250 (0.515)
VCC1207	12:29:37.70	+09:31:13.0	dE (d:E)	< (0.015)*	< (0.018)	< (0.011)	< (0.016)	< (0.011)
VCC1209	12:29:40.60	+10:23:06.0	dE (d:E)	< (0.019)	< (0.021)	< (0.017)	< (0.011)	< (0.008)
VCC1210	12:29:38.50	+11:17:56.0	dE (d:E)	< (0.023)	< (0.033)	< (0.022)	< (0.016)	< (0.011)
VCC1212	12:29:39.20	+11:37:50.0	dE (d:E)	< (0.025)	< (0.022)	< (0.022)	< (0.019)	< (0.009)
VCC1213	12:29:39.20	+12:32:54.0	dE (d:E)	< (0.020)	< (0.018)	< (0.012)	< (0.015)	< (0.014)
VCC1217	12:29:43.80	+11:24:09.0	Sm	< (0.027)	< (0.017)	< (0.015)	< (0.018)	< (0.013)
VCC1218	12:29:45.20	+05:55:13.0	dE (d:E)	< (0.024)	< (0.016)	< (0.010)	—	—
VCC1222	12:29:44.60	+15:01:29.0	dE/dS0	< (0.025)	< (0.019)	< (0.021)	—	—
VCC1225	12:29:47.30	+06:57:55.0	dE (d:E)	< (0.020)	< (0.014)	< (0.012)	< (0.012)	< (0.010)
VCC1226	12:29:46.70	+08:00:02.0	E - E/S0	< (0.028)*	< (0.019)*	< (0.022)*	< (0.024)*	< (0.017)*
VCC1228	12:29:46.00	+14:37:56.0	dE (d:E)	< (0.020)	< (0.022)	< (0.024)	< (0.043)*	< (0.026)
VCC1231	12:29:48.90	+13:25:46.0	E - E/S0	< (0.023)	< (0.018)*	< (0.018)	< (0.018)	< (0.012)
VCC1235	12:29:50.20	14:13:02.00	dE (d:E)	< (0.019)	< (0.021)	< (0.016)	< (0.020)	< (0.014)
VCC1237	12:29:51.10	+13:52:04.0	?	< (0.024)	< (0.020)	< (0.016)	< (0.018)	< (0.011)
VCC1238	12:29:54.10	+10:20:18.0	dE (d:E)	< (0.020)*	< (0.034)	< (0.027)	< (0.010)	< (0.008)
VCC1239	12:29:53.00	+11:57:44.0	dE (d:E)	< (0.030)	< (0.019)	< (0.013)	< (0.016)	< (0.013)
VCC1240	12:29:54.90	+07:08:26.0	dE (d:E)	< (0.021)	< (0.016)	< (0.011)	< (0.018)	< (0.011)
VCC1242	12:29:53.50	+14:04:07.0	S0	< (0.018)	< (0.021)	< (0.019)	< (0.014)	< (0.015)
VCC1249	12:30:01.00	+07:55:46.0	Im (Im/S)	< (0.020)	< (0.016)	< (0.014)*	< (0.020)	< (0.013)
VCC1250	12:29:59.10	+12:20:55.0	S0	0.111 (0.016)	0.306 (0.028)	0.790 (0.060)	1.480 (0.186)	1.510 (0.185)
VCC1253	12:30:02.20	+13:38:11.0	S0a - S0/Sa	0.051 (0.013)	0.179 (0.025)	0.502 (0.047)	1.082 (0.143)	1.193 (0.156)
VCC1254	12:30:05.10	+08:04:24.0	dE (d:E)	< (0.019)	< (0.013)	< (0.015)*	< (0.013)	< (0.013)
VCC1261	12:30:10.30	+10:46:46.0	dE (d:E)	< (0.020)	< (0.017)	< (0.013)	< (0.012)	< (0.010)
VCC1264	12:30:10.90	+12:11:44.0	dE (d:E)	< (0.019)	< (0.017)*	< (0.011)	< (0.015)	< (0.010)
VCC1268	12:30:13.60	+10:11:02.0	dE (d:E)	< (0.019)	< (0.016)	< (0.012)	< (0.012)	< (0.009)
VCC1273	12:30:16.90	+09:05:06.0	Im (Im/S)	< (0.017)*	0.036 (0.006)	0.063 (0.006)	0.072 (0.021)	0.024 (0.004)
VCC1279	12:30:17.40	+12:19:43.0	E - E/S0	< (0.039)*	< (0.053)*	< (0.039)*	< (0.016)	< (0.014)
VCC1283	12:30:18.40	+13:34:40.0	S0	< (0.024)	< (0.017)	< (0.011)	< (0.014)	< (0.014)
VCC1287	12:30:23.80	+13:58:56.0	Im (Im/S)	< (0.022)	< (0.014)	< (0.015)	< (0.014)	< (0.011)
VCC1290	12:30:26.80	+04:14:48.0	Sb	0.633 (0.052)	1.549 (0.115)	3.319 (0.237)	4.938 (0.599)	3.748 (0.471)
VCC1296	12:30:32.70	+06:31:56.0	dE (d:E)	< (0.020)	< (0.016)	< (0.013)	< (0.019)	< (0.015)
VCC1297	12:30:31.80	+12:29:26.0	E - E/S0	< (0.021)	< (0.016)	< (0.012)	< (0.016)	< (0.013)
VCC1303	12:30:40.60	+09:00:56.0	S0	< (0.024)	< (0.019)	< (0.012)	< (0.012)	< (0.010)
VCC1307	12:30:44.80	13:47:56.00	dE (d:E)	< (0.018)	< (0.016)	< (0.016)	< (0.014)	< (0.011)

OBJECT	RA h:m:s (J2000)	dec. d:m:s (J2000)	Type	S_{500} (σS_{500}) (Jy)	S_{350} (σS_{350}) (Jy)	S_{250} (σS_{250}) (Jy)	S_{160} (σS_{160}) (Jy)	S_{100} (σS_{100}) (Jy)
VCC1308	12:30:45.90	+11:20:35.0	dE (d:E)	< (0.018)	< (0.017)	< (0.011)	< (0.018)	< (0.009)
VCC1311	12:30:47.30	+07:36:19.0	dE (d:E)	< (0.021)	< (0.015)	< (0.013)	< (0.013)	< (0.012)
VCC1313	12:30:48.50	+12:02:42.0	BCD	< (0.018)	< (0.020)*	< (0.013)*	< (0.015)	< (0.015)*
VCC1314	12:30:48.90	+13:13:26.0	dE (d:E)	< (0.019)	< (0.017)	< (0.012)	< (0.014)	< (0.011)
VCC1316	12:30:49.40	+12:23:28.0	E - E/S0	1.430 (0.108)	1.046 (0.082)	0.817 (0.067)	0.641 (0.092)	0.427 (0.067)
VCC1317	12:30:51.00	+12:44:13.0	dE (d:E)	< (0.019)	< (0.016)	< (0.011)	< (0.015)	< (0.010)
VCC1318	12:30:51.40	+08:21:36.0	S0	< (0.019)	< (0.019)	< (0.012)	< (0.017)	< (0.012)
VCC1323	12:30:55.60	+14:46:24.0	dE (d:E)	< (0.027)	< (0.022)	< (0.020)	< (0.034)*	< (0.020)
VCC1326	12:30:57.10	+11:29:01.0	Sa	0.123 (0.023)	0.351 (0.037)	0.885 (0.071)	1.885 (0.231)	2.747 (0.334)
VCC1327	12:30:57.70	+12:16:14.0	E - E/S0	< (0.017)	< (0.018)	0.030 (0.005)	0.100 (0.025)	0.126 (0.026)
VCC1330	12:30:59.70	+08:04:41.0	Sa	0.260 (0.031)	0.663 (0.060)	1.427 (0.113)	1.770 (0.221)	1.076 (0.142)
VCC1331	12:30:58.60	+11:42:28.0	dIm/dE	< (0.027)	< (0.024)	< (0.022)*	< (0.015)	< (0.012)
VCC1333	12:31:01.10	+07:43:25.0	dE (d:E)	< (0.012)	< (0.014)	< (0.013)	< (0.015)	< (0.012)
VCC1336	12:31:04.30	+11:50:08.0	dIm/dE	< (0.027)	< (0.037)*	< (0.045)*	< (0.013)	< (0.012)
VCC1337	12:31:03.80	15:04:14.00	dE (d:E)	< (0.033)	< (0.017)	< (0.014)	—	—
VCC1348	12:31:15.70	+12:19:54.0	dE (d:E)	< (0.017)	< (0.014)	< (0.011)	< (0.016)	< (0.011)
VCC1351	12:31:17.50	+13:49:42.0	dE (d:E)	< (0.022)	< (0.014)	< (0.012)	< (0.016)	< (0.012)
VCC1352	12:31:19.60	+12:36:42.0	dE (d:E)	< (0.020)	< (0.023)*	< (0.017)*	< (0.013)	< (0.012)
VCC1353	12:31:19.30	+12:44:17.0	dE (d:E)	< (0.019)*	< (0.028)*	< (0.015)*	< (0.021)	< (0.010)
VCC1355	12:31:20.00	+14:06:53.0	dE (d:E)	< (0.021)	< (0.013)	< (0.012)	< (0.016)	< (0.013)
VCC1356	12:31:22.90	+11:29:33.0	Sm/BCD	0.038 (0.013)	0.071 (0.016)	0.118 (0.019)	0.165 (0.032)	0.110 (0.030)
VCC1361	12:31:26.80	+09:43:56.0	dE (d:E)	< (0.023)	< (0.016)	< (0.011)	< (0.013)	< (0.009)
VCC1366	12:31:31.70	+11:36:11.0	dE (d:E)	< (0.033)	< (0.021)	< (0.014)	< (0.019)	< (0.014)
VCC1368	12:31:32.50	+11:37:29.0	S0a - S0/Sa	< (0.029)	< (0.019)	< (0.015)	< (0.015)	< (0.015)
VCC1369	12:31:33.30	+12:03:50.0	dE (d:E)	< (0.018)	< (0.014)*	< (0.010)*	< (0.014)	< (0.012)
VCC1370	12:31:36.20	+10:59:57.0	dE (d:E)	< (0.021)	< (0.019)	< (0.012)	< (0.012)	< (0.008)
VCC1373	12:31:36.90	+14:04:15.0	dE (d:E)	< (0.022)	< (0.021)*	< (0.012)	< (0.019)	< (0.010)
VCC1374	12:31:38.00	+14:51:24.0	Im/BCD	0.057 (0.011)	0.108 (0.011)	0.251 (0.030)	0.272 (0.055)	0.174 (0.044)
VCC1375	12:31:39.20	+03:56:22.0	Sc	1.636 (0.122)	4.045 (0.289)	8.429 (0.597)	—	—
VCC1377	12:31:39.00	+10:50:26.0	Im (Im/S)	< (0.020)	< (0.026)	< (0.023)	< (0.011)	< (0.008)
VCC1384	12:31:47.00	+10:40:09.0	dE (d:E)	< (0.021)	< (0.023)	< (0.013)	< (0.011)	< (0.009)
VCC1386	12:31:51.30	+12:39:25.0	dE (d:E)	< (0.026)	< (0.024)	< (0.017)	< (0.014)	< (0.011)
VCC1389	12:31:52.00	+12:28:55.0	dE (d:E)	< (0.015)	< (0.014)	< (0.012)	< (0.016)	< (0.012)
VCC1392	12:31:56.00	+12:10:26.0	dE/dS0	< (0.019)	< (0.021)	< (0.016)	< (0.016)	< (0.012)
VCC1396	12:31:56.40	+11:58:22.0	dE (d:E)	< (0.023)	< (0.017)	< (0.012)*	< (0.017)*	< (0.011)
VCC1399	12:32:00.70	+12:37:13.0	dE (d:E)	< (0.021)	< (0.024)	< (0.012)	< (0.016)	< (0.009)
VCC1400	12:31:53.80	+14:18:24.0	dE (d:E)	< (0.021)	< (0.020)	< (0.016)	< (0.018)	< (0.010)
VCC1401	12:31:59.20	+14:25:14.0	Sbc	9.064 (0.641)	24.628 (1.738)	60.366 (4.243)	96.985 (11.643)	76.043 (9.131)
VCC1402	12:32:00.30	11:01:24.00	dE (d:E)	< (0.024)	< (0.023)	< (0.028)	< (0.010)	< (0.007)
VCC1403	12:31:59.60	+13:05:00.0	Im (Im/S)	< (0.021)	< (0.023)*	< (0.013)	< (0.019)	< (0.011)
VCC1407	12:32:02.70	+11:53:24.0	dE (d:E)	< (0.017)	< (0.017)	< (0.012)*	< (0.018)	< (0.012)
VCC1408	12:32:04.30	7:56:39.00	dIm/dE	< (0.021)	< (0.022)*	< (0.024)*	< (0.014)	< (0.012)
VCC1411	12:32:05.70	+11:49:05.0	Pec	< (0.021)	< (0.018)	< (0.024)*	< (0.020)	< (0.014)
VCC1412	12:32:06.20	+11:10:35.0	Sa	< (0.030)	< (0.028)	< (0.032)	< (0.018)	< (0.010)
VCC1413	12:32:07.70	+12:26:03.0	dIm/dE	< (0.020)	< (0.012)	< (0.012)	< (0.019)	< (0.009)
VCC1414	12:32:09.20	+12:50:21.0	dE (d:E)	< (0.023)	< (0.015)	< (0.010)	< (0.016)	< (0.011)
VCC1418	12:32:11.90	+12:30:43.0	dE (d:E)	< (0.021)	< (0.018)	< (0.015)	< (0.018)	< (0.011)
VCC1419	12:32:10.50	+13:25:11.0	S (dS)	0.085 (0.019)	0.198 (0.029)	0.372 (0.036)	0.572 (0.077)	0.326 (0.049)
VCC1420	12:32:12.20	+12:03:42.0	dE (d:E)	< (0.029)*	< (0.048)*	< (0.048)*	< (0.013)	< (0.013)
VCC1422	12:32:14.20	+10:15:05.0	E - E/S0	< (0.023)	< (0.023)	< (0.015)	< (0.011)	< (0.008)
VCC1426	12:32:23.50	+11:53:36.0	Im (Im/S)	< (0.021)	< (0.017)	< (0.012)	< (0.019)	< (0.011)
VCC1431	12:32:23.40	+11:15:46.0	dE (d:E)	< (0.025)	< (0.025)	< (0.026)	< (0.015)	< (0.012)
VCC1432	12:32:29.70	+10:01:03.0	dE (d:E)	< (0.019)	< (0.016)	< (0.012)	< (0.014)	< (0.008)
VCC1435	12:32:32.40	+08:02:43.0	Im (Im/S)	< (0.019)	< (0.014)	< (0.011)	< (0.021)	< (0.009)
VCC1437	12:32:33.50	+09:10:25.0	BCD	0.030 (0.008)	0.076 (0.009)	0.220 (0.025)	0.426 (0.059)	0.528 (0.076)
VCC1438	12:32:33.50	+12:38:57.0	dE (d:E)	< (0.018)	< (0.018)	< (0.011)	< (0.017)	< (0.010)
VCC1441	12:32:35.80	+08:05:33.0	dE (d:E)	< (0.022)	< (0.017)	< (0.013)	< (0.014)	< (0.009)
VCC1444	12:32:35.90	+09:53:11.0	dE (d:E)	< (0.017)	< (0.015)	< (0.014)	< (0.015)	< (0.011)

OBJECT	RA h:m:s (J2000)	dec. d:m:s (J2000)	Type	S_{500} (σS_{500}) (Jy)	S_{350} (σS_{350}) (Jy)	S_{250} (σS_{250}) (Jy)	S_{160} (σS_{160}) (Jy)	S_{100} (σS_{100}) (Jy)
VCC1446	12:32:39.00	+10:05:31.0	dE (d:E)	< (0.019)	< (0.013)	< (0.014)	< (0.010)	< (0.008)
VCC1448	12:32:41.00	+12:46:16.0	dIm/dE	< (0.019)	< (0.016)	< (0.014)	< (0.023)	< (0.011)
VCC1449	12:32:39.40	13:19:39.00	dE (d:E)	< (0.020)*	< (0.024)*	< (0.016)	< (0.013)	< (0.012)
VCC1450	12:32:41.70	+14:03:06.0	Sc	0.489 (0.048)	1.206 (0.102)	2.439 (0.186)	3.359 (0.410)	2.917 (0.359)
VCC1453	12:32:44.20	+14:11:46.0	dE (d:E)	< (0.025)	< (0.025)	< (0.034)	< (0.013)	< (0.011)
VCC1455	12:32:46.80	+07:47:56.0	Im (Im/S)	< (0.024)	0.019 (0.006)	0.030 (0.008)	< (0.013)	< (0.015)
VCC1464	12:32:53.90	+11:11:29.0	dE (d:E)	< (0.046)	< (0.063)	< (0.026)	< (0.014)	< (0.010)
VCC1479	12:33:07.50	+14:34:30.0	S0	< (0.025)	< (0.021)	< (0.019)*	< (0.024)	< (0.017)
VCC1481	12:33:09.00	+10:50:10.0	dE (d:E)	< (0.024)	< (0.029)*	< (0.019)*	< (0.009)	< (0.010)
VCC1482	12:33:07.70	+12:17:03.0	dE (d:E)	< (0.017)	< (0.017)	< (0.014)	< (0.015)	< (0.011)
VCC1486	12:33:10.00	+11:20:51.0	S (dS)	0.052 (0.009)	0.114 (0.011)	0.254 (0.030)	0.314 (0.060)	0.285 (0.050)
VCC1488	12:33:13.40	+09:23:50.0	E - E/S0	< (0.018)	< (0.017)	< (0.031)*	< (0.021)	< (0.012)
VCC1489	12:33:13.80	+10:55:44.0	dE (d:E)	< (0.019)	< (0.020)	< (0.025)	< (0.012)	< (0.011)
VCC1491	12:33:14.00	+12:51:28.0	dE (d:E)	< (0.020)	< (0.016)	< (0.017)	< (0.014)	< (0.012)
VCC1496	12:33:18.80	+09:07:14.0	dE (d:E)	< (0.015)	< (0.019)	< (0.014)	< (0.012)	< (0.012)
VCC1498	12:33:20.80	+07:51:12.0	dE (d:E)	< (0.019)	< (0.021)	< (0.011)	< (0.016)	< (0.012)
VCC1499	12:33:19.80	+12:51:13.0	E - E/S0	< (0.018)	< (0.017)	< (0.015)	< (0.014)	< (0.014)
VCC1501	12:33:24.80	+08:41:27.0	dS0	< (0.023)	< (0.020)	< (0.017)	< (0.015)	< (0.014)*
VCC1503	12:33:26.60	+06:36:59.0	dE (d:E)	< (0.019)	< (0.017)	< (0.012)	< (0.026)	< (0.021)
VCC1508	12:33:30.30	+08:39:16.0	Sc	1.043 (0.086)	2.520 (0.189)	5.270 (0.376)	8.443 (1.027)	7.297 (0.888)
VCC1509	12:33:31.60	+09:27:33.0	dE (d:E)	< (0.019)	< (0.020)	< (0.014)	< (0.022)	< (0.015)
VCC1512	12:33:34.50	+11:15:43.0	dS0	< (0.030)	< (0.028)	0.036 (0.008)	0.019 (0.006)	< (0.009)
VCC1514	12:33:37.70	+07:52:17.0	dE (d:E)	< (0.026)*	< (0.019)*	< (0.013)	< (0.012)	< (0.012)
VCC1516	12:33:39.70	+09:10:30.0	Sbc	0.620 (0.051)	1.593 (0.119)	3.461 (0.252)	4.415 (0.534)	3.973 (0.482)
VCC1519	12:33:42.20	+07:47:00.0	dE (d:E)	< (0.019)	< (0.020)	< (0.010)	< (0.012)	< (0.012)
VCC1521	12:33:45.00	+10:59:45.0	E - E/S0	< (0.021)	< (0.017)	< (0.017)	< (0.016)	< (0.009)
VCC1523	12:33:48.70	+12:46:48.0	dE (d:E)	< (0.017)	< (0.015)	< (0.017)*	< (0.021)	< (0.012)
VCC1528	12:33:51.60	+13:19:21.0	dE (d:E)	< (0.023)	< (0.020)	< (0.011)	< (0.017)	< (0.012)
VCC1531	12:33:56.50	+10:34:40.0	dE (d:E)	< (0.022)	< (0.023)	< (0.013)	< (0.014)	< (0.010)
VCC1535	12:34:03.00	+07:41:57.0	S0	1.068 (0.082)	3.174 (0.230)	8.143 (0.575)	15.890 (1.910)	15.600 (1.874)
VCC1537	12:34:06.00	+11:19:16.0	S0	< (0.026)	< (0.033)*	< (0.028)	< (0.018)	< (0.011)
VCC1539	12:34:06.70	+12:44:30.0	dE (d:E)	< (0.016)	< (0.017)	< (0.013)	< (0.015)	< (0.011)
VCC1545	12:34:11.50	+12:02:56.0	E - E/S0	< (0.026)*	< (0.027)*	< (0.022)*	< (0.014)	< (0.011)
VCC1549	12:34:14.80	+11:04:18.0	dE (d:E)	< (0.021)	< (0.014)	< (0.010)	< (0.018)	< (0.011)
VCC1552	12:34:15.80	+13:04:32.0	Sa	0.238 (0.027)	0.656 (0.057)	1.631 (0.129)	2.225 (0.273)	1.309 (0.170)
VCC1554	12:34:19.30	+06:28:04.0	Sm	1.263 (0.093)	3.214 (0.229)	6.909 (0.487)	—	—
VCC1555	12:34:20.30	+08:11:52.0	Sc	6.192 (0.469)	15.817 (1.138)	34.767 (2.449)	52.030 (6.251)	37.480 (4.516)
VCC1561	12:34:25.00	+12:54:10.0	dE (d:E)	< (0.021)	< (0.020)	< (0.015)	< (0.017)	< (0.011)
VCC1565	12:34:30.40	+11:44:04.0	dE (d:E)	< (0.028)	< (0.029)	< (0.025)	< (0.011)	< (0.012)
VCC1566	12:34:30.70	+09:09:17.0	Sd	0.071 (0.015)	0.145 (0.022)	0.233 (0.029)	0.183 (0.035)	0.100 (0.024)
VCC1567	12:34:31.30	+09:37:24.0	dE/dS0	< (0.021)	< (0.016)	< (0.015)	< (0.020)	< (0.010)
VCC1569	12:34:31.80	+13:30:13.0	Scd	< (0.021)*	0.035 (0.010)	0.081 (0.017)	0.018 (0.006)	< (0.011)
VCC1573	12:34:32.50	+10:32:54.0	dE (d:E)	< (0.016)	< (0.017)	< (0.013)	< (0.014)	< (0.008)
VCC1575	12:34:39.50	+07:09:37.0	Sm	0.266 (0.032)	0.701 (0.061)	1.614 (0.122)	2.550 (0.314)	2.114 (0.260)
VCC1582	12:34:42.60	+14:13:23.0	dIm/dE	< (0.022)*	< (0.022)*	< (0.016)*	< (0.029)	< (0.014)
VCC1596	12:35:00.90	+09:11:08.0	Im (Im/S)	< (0.020)	< (0.017)	< (0.011)	< (0.021)	< (0.009)
VCC1599	12:35:06.60	+11:54:03.0	dE (d:E)	< (0.021)	< (0.017)	< (0.017)*	< (0.023)*	< (0.011)
VCC1601	12:35:07.50	12:58:05.00	dE (d:E)	< (0.023)	< (0.034)*	< (0.028)*	< (0.017)	< (0.010)
VCC1603	12:35:07.80	13:33:52.00	dE (d:E)	< (0.018)	< (0.016)	< (0.014)*	< (0.019)	< (0.014)
VCC1605	12:35:13.90	+10:25:55.0	Sd	< (0.020)	< (0.023)	< (0.020)	< (0.016)	< (0.008)
VCC1606	12:35:14.70	+12:14:15.0	dE (d:E)	< (0.019)	< (0.015)	< (0.011)	< (0.020)	< (0.016)
VCC1609	12:35:20.30	+11:38:11.0	dE (d:E)	< (0.042)	< (0.020)	< (0.027)	< (0.016)	< (0.010)
VCC1614	12:35:27.20	+12:45:01.0	S0	0.020 (0.007)	< (0.017)	0.035 (0.008)	0.078 (0.025)	0.038 (0.013)
VCC1615	12:35:26.40	+14:29:47.0	Sb	2.373 (0.177)	6.809 (0.536)	15.492 (1.164)	13.538 (1.668)	< (21.431)
VCC1616	12:35:27.90	+14:15:41.0	dE (d:E)	< (0.029)	< (0.024)	< (0.017)	< (0.027)	< (0.023)
VCC1619	12:35:30.60	+12:13:15.0	E - E/S0	< (0.016)	0.041 (0.006)	0.133 (0.018)	0.290 (0.046)	0.225 (0.035)
VCC1627	12:35:37.20	+12:22:55.0	E - E/S0	< (0.022)	< (0.020)	< (0.018)	< (0.017)	< (0.010)
VCC1629	12:35:38.00	+09:35:29.0	dE (d:E)	< (0.019)	< (0.020)	< (0.012)	< (0.018)	< (0.012)

OBJECT	RA h:m:s (J2000)	dec. d:m:s (J2000)	Type	S_{500} (σS_{500}) (Jy)	S_{350} (σS_{350}) (Jy)	S_{250} (σS_{250}) (Jy)	S_{160} (σS_{160}) (Jy)	S_{100} (σS_{100}) (Jy)
VCC1630	12:35:38.00	+12:15:50.0	E - E/S0	< (0.019)*	< (0.017)	< (0.014)	< (0.017)	< (0.015)
VCC1632	12:35:39.80	+12:33:23.0	S0	0.044 (0.007)	0.037 (0.007)	0.034 (0.006)	0.021 (0.006)	0.021 (0.006)
VCC1636	12:35:43.80	+14:24:43.0	Sb	0.054 (0.011)	0.176 (0.023)	0.360 (0.034)	—	—
VCC1642	12:35:53.10	+11:40:55.0	dE (d:E)	< (0.022)	< (0.023)	< (0.016)	< (0.016)	< (0.011)
VCC1644	12:35:51.80	+13:51:33.0	Sm	< (0.027)	< (0.018)	< (0.015)	< (0.027)	< (0.018)
VCC1647	12:35:56.50	+10:56:12.0	dE (d:E)	< (0.025)	< (0.026)	< (0.017)	< (0.015)	< (0.011)
VCC1649	12:36:02.90	+07:12:00.0	dE (d:E)	< (0.020)	< (0.015)	< (0.011)	< (0.022)	< (0.007)
VCC1650	12:36:02.50	+13:29:05.0	dE (d:E)	< (0.016)	< (0.014)	< (0.011)	< (0.026)	< (0.015)
VCC1652	12:36:07.80	+07:35:53.0	dE (d:E)	< (0.019)	< (0.016)	< (0.011)	< (0.016)	< (0.009)
VCC1654	12:36:10.50	+09:55:21.0	Im (Im/S)	0.034 (0.007)	0.027 (0.006)	0.021 (0.006)	< (0.033)	< (0.022)
VCC1657	12:36:15.50	+10:35:48.0	dE (d:E)	< (0.021)	< (0.023)	< (0.012)	< (0.018)	< (0.013)
VCC1661	12:36:24.80	+10:23:05.0	dE (d:E)	< (0.020)	< (0.020)*	< (0.014)*	< (0.021)	< (0.015)
VCC1663	12:36:27.10	+11:53:21.0	dE (d:E)	< (0.026)	< (0.020)	< (0.018)	< (0.014)	< (0.010)
VCC1664	12:36:27.00	+11:26:22.0	E - E/S0	< (0.021)	< (0.017)	< (0.014)	< (0.017)	< (0.011)
VCC1668	12:36:30.10	13:32:33.00	dS0	< (0.025)	< (0.019)	< (0.017)	< (0.024)	< (0.022)
VCC1669	12:36:30.60	+13:38:18.0	dE (d:E)	< (0.026)	< (0.019)	< (0.022)	< (0.024)*	< (0.030)
VCC1673	12:36:32.70	+11:15:29.0	Sc	1.864 (0.305)	4.567 (1.515)	11.408 (2.215)	20.500 (4.100)	16.100 (3.200)
VCC1674	12:36:32.30	+13:44:54.0	dE (d:E)	< (0.027)	< (0.026)	< (0.025)	< (0.044)	< (0.037)
VCC1675	12:36:34.90	+08:03:17.0	Pec	< (0.021)	0.032 (0.010)	0.079 (0.015)	0.102 (0.026)	0.019 (0.006)
VCC1676	12:36:34.20	+11:14:20.0	Sc	4.110 (0.838)	12.317 (2.408)	31.864 (6.226)	51.100 (10.200)	46.100 (9.200)
VCC1682	12:36:36.60	+14:13:32.0	dE (d:E)	< (0.036)	< (0.036)	< (0.027)*	—	—
VCC1683	12:36:38.10	+10:56:15.0	dE (d:E)	< (0.022)	< (0.014)*	< (0.013)	< (0.015)	< (0.012)
VCC1684	12:36:39.40	+11:06:07.0	dS0	< (0.022)	< (0.023)	< (0.020)	< (0.016)*	< (0.011)
VCC1686	12:36:43.50	+13:15:34.0	Sm	0.286 (0.032)	0.646 (0.061)	1.362 (0.109)	1.317 (0.184)	0.845 (0.128)
VCC1689	12:36:51.30	+12:22:09.0	dE (d:E)	< (0.019)	< (0.020)	< (0.018)	< (0.016)	< (0.012)
VCC1690	12:36:49.80	+13:09:46.0	Sab	3.275 (0.241)	9.077 (0.646)	23.070 (1.627)	36.705 (4.416)	27.520 (3.320)
VCC1692	12:36:53.40	+07:14:48.0	E - E/S0	< (0.020)	< (0.015)	< (0.011)	< (0.017)	< (0.013)
VCC1695	12:36:54.80	+12:31:12.0	dS0	< (0.017)	< (0.020)	< (0.012)	< (0.017)	< (0.013)
VCC1696	12:36:56.40	+14:13:02.0	Sc	1.359 (0.118)	3.997 (0.306)	8.916 (0.677)	—	—
VCC1699	12:37:03.00	+06:55:36.0	Sm	0.059 (0.013)	0.131 (0.019)	0.254 (0.031)	0.350 (0.061)	0.522 (0.083)
VCC1702	12:37:07.70	+13:58:54.0	dE (d:E)	< (0.023)	< (0.026)	< (0.021)	—	—
VCC1704	12:37:09.70	+10:16:20.0	dE (d:E)	< (0.018)	< (0.014)	< (0.011)	—	—
VCC1705	12:37:10.40	+09:29:18.0	dE (d:E)	< (0.026)*	< (0.021)*	< (0.021)*	< (0.037)*	< (0.026)*
VCC1710	12:37:17.20	+10:53:16.0	dE (d:E)	< (0.015)	< (0.013)	< (0.015)	< (0.017)	< (0.014)
VCC1711	12:37:22.10	+12:17:13.0	dE (d:E)	< (0.022)	< (0.018)	< (0.014)	< (0.020)	< (0.014)
VCC1715	12:37:28.40	+08:47:39.0	dE (d:E)	< (0.018)	< (0.020)	0.016 (0.004)	< (0.022)	< (0.017)
VCC1717	12:37:28.90	+12:21:11.0	dE (d:E)	< (0.023)	< (0.020)	< (0.017)	< (0.021)	< (0.017)
VCC1720	12:37:30.50	+09:33:18.0	S0	< (0.017)*	< (0.009)*	< (0.014)*	—	—
VCC1725	12:37:41.20	+08:33:33.0	Sm/BCD	0.113 (0.019)	0.199 (0.024)	0.345 (0.032)	0.366 (0.056)	0.479 (0.079)
VCC1726	12:37:45.20	+07:06:12.0	Sdm - Sd/Sm	0.034 (0.006)	0.091 (0.020)	0.143 (0.026)	< (0.024)	< (0.018)
VCC1727	12:37:43.50	+11:49:05.0	Sab	3.307 (0.251)	9.207 (0.684)	21.602 (1.563)	34.066 (4.098)	23.037 (2.783)
VCC1729	12:37:46.00	+10:59:07.0	dE (d:E)	< (0.016)	< (0.015)	< (0.011)	< (0.016)	< (0.010)
VCC1743	12:38:06.80	+10:04:56.0	dE (d:E)	< (0.030)	< (0.024)	< (0.021)	—	—
VCC1744	12:38:06.90	+10:09:56.0	BCD	< (0.024)	< (0.024)	< (0.016)	—	—
VCC1750	12:38:15.50	+06:59:39.0	BCD	< (0.019)	< (0.022)	0.027 (0.005)	< (0.036)	0.023 (0.006)
VCC1755	12:38:18.20	+07:13:02.0	dE (d:E)	< (0.015)*	< (0.013)	< (0.011)	< (0.019)	< (0.015)
VCC1756	12:38:18.80	+09:06:55.0	dIm/dE	< (0.022)	< (0.023)	< (0.016)*	—	—
VCC1757	12:38:17.90	+13:06:36.0	Sa	0.058 (0.010)	0.206 (0.022)	0.478 (0.042)	—	—
VCC1758	12:38:21.00	+07:53:31.0	Sc	0.141 (0.021)	0.285 (0.029)	0.475 (0.041)	0.581 (0.089)	0.245 (0.040)
VCC1762	12:38:32.20	+10:22:36.0	dE (d:E)	< (0.021)	< (0.016)	< (0.014)	—	—
VCC1776	12:38:55.10	+10:14:37.0	dIm/dE	< (0.028)	0.037 (0.008)	0.125 (0.023)	—	—
VCC1785	12:39:15.70	+11:16:11.0	dE (d:E)	< (0.020)	< (0.016)	< (0.015)	< (0.022)	< (0.017)
VCC1791	12:39:25.00	+07:57:57.0	Sm/BCD	0.090 (0.015)	0.169 (0.026)	0.361 (0.044)	0.460 (0.082)	0.225 (0.058)
VCC1794	12:39:27.10	+11:46:35.0	dE (d:E)	< (0.020)	< (0.015)	< (0.019)	< (0.027)	< (0.020)
VCC1803	12:39:37.70	+10:58:33.0	dE (d:E)	< (0.020)	< (0.016)	< (0.013)	< (0.026)	< (0.016)
VCC1831	12:40:18.30	10:59:48.00	dE (d:E)	< (0.020)	< (0.021)	< (0.017)	< (0.020)	< (0.014)
VCC1843	12:40:27.90	+10:50:20.0	dE (d:E)	< (0.021)	< (0.023)	< (0.017)	< (0.027)	< (0.022)

Table B1: 5-band FIR detections and upper limits for the VCC galaxies. Uncertainties on detections are the quadrature sum of the aperture noise and the calibration uncertainty (as described in Section 2.2). Where galaxies are listed undetected, upper limits are given in the error column and are defined as the 3-sigma upper limit, measured from the PSF-convolved map. Galaxies that fell outside of the PACS footprint are unmeasured at 160 and 100 μm . Asterisks denote galaxy measurements that were confused by foreground cirrus or unresolved background sources. VCC881 has been split into multiple components according to Gomez et al. (2010).

**APPENDIX C: TABLE OF DUST MASSES AND TEMPERATURE DERIVED FROM
SINGLE-TEMPERATURE MODIFIED BLACKBODY FITS TO 140 VCC GALAXIES**

Object	RA	dec	Type	Distance (Mpc)	T (K)	$\log(M_D/M_\odot)$	$\chi^2_{dof=3}$
VCC10	12:09:24.90	+13:34:28.0	BCD	32	19.8 (1.0)	6.4 (0.1)	3.3637
VCC25	12:10:37.50	+16:01:59.0	Sc	32	22.5 (0.8)	7.5 (0.1)	1.3392
VCC28	12:10:45.60	+15:51:55.0	Sc	17	17.2 (1.1)	5.7 (0.2)	2.6363
VCC47	12:12:11.80	+13:14:48.0	Sa	32	17.6 (0.6)	7.0 (0.1)	3.4034
VCC58	12:12:32.30	+12:07:26.0	Sb	32	17.5 (0.6)	7.4 (0.1)	2.584
VCC73	12:13:03.00	+07:02:20.0	Sb	32	23.7 (0.8)	7.3 (0.1)	0.9731
VCC89	12:13:47.30	+13:25:29.0	Sc	32	21.5 (0.7)	7.6 (0.1)	1.6889
VCC92	12:13:48.30	+14:54:01.0	Sb	17	19.2 (0.5)	7.9 (0.1)	0.6288
VCC97	12:13:53.60	+13:10:22.0	Sc	32	18.8 (0.6)	7.6 (0.1)	1.0492
VCC99	12:14:02.10	+06:43:23.0	Sa	32	16.8 (0.7)	6.6 (0.1)	0.6295
VCC131	12:15:04.50	+14:01:44.0	Sc	17	17.9 (0.6)	6.7 (0.1)	2.9383
VCC135	12:15:06.70	+12:01:00.0	S/BCD	32	21.4 (1.0)	6.5 (0.1)	1.1282
VCC143	12:15:16.10	+13:28:29.0	Sc	17	14.7 (1.6)	6.0 (0.3)	7.3118
VCC144	12:15:18.30	+05:45:39.0	BCD	32	25.8 (1.5)	6.0 (0.1)	0.8932
VCC157	12:15:39.30	+13:54:05.0	Sc	17	22.0 (0.6)	7.3 (0.1)	2.1474
VCC167	12:15:54.40	+13:08:58.0	Sb	17	18.2 (0.5)	7.8 (0.1)	1.358
VCC172	12:16:00.40	+04:39:03.0	BCD	32	17.9 (1.1)	6.2 (0.1)	2.376
VCC199	12:16:33.70	+07:27:44.0	Sa	32	17.7 (0.5)	7.2 (0.1)	6.273
VCC209	12:16:52.40	+14:30:55.0	dS0	17	16.8 (0.9)	5.9 (0.1)	3.5312
VCC213	12:16:56.00	+13:37:32.0	S/BCD	17	21.7 (0.7)	6.1 (0.1)	2.2274
VCC221	12:17:09.10	+03:40:59.0	Sc	32	22.3 (0.9)	7.1 (0.1)	1.8595
VCC222	12:17:09.90	+07:11:30.0	Sa	32	19.3 (0.7)	6.8 (0.1)	4.0088
VCC226	12:17:11.40	+15:19:26.0	Sc	17	21.3 (0.6)	7.1 (0.1)	2.9546
VCC234	12:17:25.80	+06:41:24.0	Sa	32	16.2 (0.5)	7.3 (0.1)	2.9872
VCC256	12:17:47.30	+04:28:43.0	S (dS)	32	18.1 (0.8)	6.1 (0.1)	2.975
VCC262	12:17:55.80	+05:52:11.0	Sc	17	20.0 (0.9)	5.8 (0.1)	0.0659
VCC267	12:17:59.90	+06:39:15.0	Sbc	23	16.1 (0.8)	7.0 (0.1)	3.2454
VCC281	12:18:15.30	+13:44:57.0	S/BCD	17	12.9 (0.8)	6.0 (0.2)	6.3362
VCC297	12:18:38.60	+06:42:30.0	Sc	23	17.7 (1.1)	5.9 (0.2)	2.2092
VCC307	12:18:49.60	+14:24:59.0	Sc	17	23.0 (0.7)	8.0 (0.1)	2.2539
VCC318	12:19:02.90	+08:51:22.0	Scd	32	17.1 (0.9)	6.8 (0.1)	1.904
VCC323	12:19:06.50	+05:43:33.0	Sa	32	19.3 (0.6)	6.7 (0.1)	1.5232
VCC327	12:19:12.40	+06:22:53.0	S0	32	18.8 (1.5)	6.0 (0.2)	3.9138
VCC341	12:19:22.20	+06:05:55.0	Sa	23	17.3 (0.6)	6.8 (0.1)	2.662
VCC362	12:19:42.30	+05:32:17.0	Sa	32	20.0 (0.5)	7.0 (0.1)	2.9277
VCC382	12:19:56.00	+05:20:36.0	Sc	32	23.8 (0.8)	7.7 (0.1)	1.2549
VCC393	12:20:07.50	+07:41:31.0	Sc	23	19.9 (0.7)	6.8 (0.1)	0.6081
VCC404	12:20:17.30	+04:12:06.0	Scd	17	18.0 (0.6)	6.5 (0.1)	2.9556
VCC406	12:20:18.70	+08:31:59.0	Sbc	17	19.1 (1.0)	5.8 (0.1)	2.3268
VCC408	12:20:21.50	+05:23:11.0	S0	32	23.8 (1.0)	6.5 (0.1)	2.0117
VCC411	12:20:24.30	+05:34:22.0	S0	23	19.2 (1.0)	6.0 (0.1)	3.5458
VCC415	12:20:25.20	+06:54:32.0	Sd	23	16.8 (0.9)	6.3 (0.2)	4.7429
VCC419	12:20:29.50	+10:14:42.0	Sb	17	20.8 (1.5)	5.8 (0.1)	3.564
VCC434	12:20:48.50	+05:38:23.0	S (dS)	23	19.9 (0.6)	6.4 (0.1)	0.0482
VCC449	12:21:02.30	+03:43:19.0	Sbc	17	18.2 (0.6)	6.9 (0.1)	7.636
VCC450	12:21:03.70	+07:04:40.0	S0	23	19.5 (1.0)	6.0 (0.1)	2.7179
VCC462	12:21:16.40	+04:35:44.0	S0a - S0/Sa	17	21.1 (0.8)	6.0 (0.1)	1.3394
VCC479	12:21:29.00	+08:09:03.0	?	23	13.1 (0.7)	6.3 (0.2)	2.0121
VCC483	12:21:32.80	+14:36:22.0	Sc	17	20.7 (0.6)	7.4 (0.1)	2.9491
VCC491	12:21:40.90	+11:30:12.0	Scd	17	21.2 (0.9)	6.7 (0.1)	6.2223
VCC492	12:21:41.50	+05:23:05.0	Sa	23	20.6 (0.7)	6.4 (0.1)	2.64
VCC497	12:21:42.50	+14:35:52.0	Sc	17	19.2 (0.5)	7.7 (0.1)	3.1475
VCC508	12:21:54.90	+04:28:25.0	Sc	17	22.8 (0.7)	7.9 (0.1)	0.289
VCC517	12:22:01.30	+05:06:00.0	Sab	17	20.5 (0.8)	6.1 (0.1)	3.5618
VCC524	12:22:05.60	+09:02:37.0	Sbc	23	19.8 (0.5)	7.3 (0.1)	2.8402
VCC534	12:22:12.40	+07:08:39.0	Sa	23	19.3 (0.8)	6.8 (0.1)	5.9347
VCC552	12:22:27.20	+04:33:59.0	Sc	17	18.4 (1.1)	6.5 (0.1)	6.8967

Object	RA	dec	Type	Distance (Mpc)	T (K)	$\log(M_D/M_\odot)$	$\chi^2_{dof=3}$
VCC559	12:22:31.30	+15:32:17.0	Sab	17	22.4 (0.7)	6.8 (0.1)	5.3575
VCC568	12:22:39.70	+06:13:34.0	S (dS)	23	16.2 (1.0)	6.1 (0.1)	3.5565
VCC570	12:22:38.50	+11:48:03.0	Sab	17	20.3 (0.5)	6.9 (0.1)	3.5497
VCC571	12:22:41.10	+07:57:01.0	S0	23	16.2 (1.0)	5.9 (0.2)	1.0217
VCC576	12:22:42.20	+09:19:57.0	Sbc	23	20.1 (0.6)	7.3 (0.1)	0.6984
VCC596	12:22:54.90	+15:49:21.0	Sc	17	21.5 (0.6)	8.1 (0.1)	2.0706
VCC613	12:23:06.20	+05:15:02.0	Sa	17	19.0 (0.5)	6.7 (0.1)	1.77
VCC630	12:23:17.20	+11:22:05.0	Sd	17	18.2 (0.5)	7.0 (0.1)	1.7
VCC656	12:23:38.70	+06:57:15.0	Sb	23	19.8 (0.6)	7.2 (0.1)	1.1153
VCC664	12:23:44.50	+12:28:42.0	Sc	17	18.1 (0.6)	6.4 (0.1)	3.8602
VCC667	12:23:48.50	+07:11:13.0	Sc	23	17.4 (0.5)	6.8 (0.1)	0.2692
VCC672	12:23:53.50	+07:06:26.0	S0	23	17.3 (0.5)	5.9 (0.1)	1.5383
VCC688	12:24:00.10	+07:47:06.0	Sc	23	18.9 (0.6)	6.5 (0.1)	2.5243
VCC690	12:24:02.20	+05:18:45.0	S (dS)	17	20.8 (1.0)	5.8 (0.1)	4.2232
VCC692	12:24:01.50	+12:12:17.0	Sc	17	19.5 (0.6)	6.6 (0.1)	0.2166
VCC693	12:24:03.20	+05:10:51.0	Sm	17	17.2 (0.7)	5.8 (0.1)	1.6154
VCC697	12:24:05.50	+07:02:29.0	Sc	23	18.6 (0.6)	6.6 (0.1)	1.3084
VCC699	12:24:07.40	+06:36:27.0	Pec	23	21.0 (1.0)	6.5 (0.1)	6.2302
VCC713	12:24:14.50	+08:32:09.0	Sc	23	20.1 (0.7)	6.7 (0.1)	1.6325
VCC734	12:24:33.60	+06:42:44.0	Sbc	17	18.3 (1.1)	5.8 (0.2)	5.8596
VCC737	12:24:39.40	+03:59:44.0	S/BCD	17	16.6 (1.0)	5.9 (0.2)	2.1592
VCC739	12:24:40.00	+03:18:10.0	Sd	17	18.1 (1.1)	6.1 (0.1)	6.5397
VCC741	12:24:41.30	+03:43:17.0	BCD	17	19.7 (2.4)	5.2 (0.3)	4.5118
VCC758	12:24:54.90	+07:26:40.0	S0	23	22.2 (0.7)	6.8 (0.1)	2.7338
VCC781	12:25:15.20	+12:42:53.0	dS0	17	19.0 (1.6)	5.4 (0.2)	1.1692
VCC785	12:25:18.10	+04:55:30.0	Sa	17	16.6 (0.4)	7.1 (0.1)	4.8788
VCC787	12:25:18.00	+05:44:28.0	Scd	23	19.9 (0.8)	6.7 (0.1)	3.6289
VCC792	12:25:22.20	+10:01:01.0	Sab	23	18.2 (0.4)	7.4 (0.1)	5.2217
VCC809	12:25:33.10	+12:15:37.0	Sc	17	15.5 (0.6)	6.5 (0.1)	3.0928
VCC827	12:25:42.60	+07:13:00.0	Sc	23	18.8 (0.6)	7.4 (0.1)	5.7799
VCC834	12:25:46.70	+04:30:35.0	Sc	17	18.3 (0.8)	6.3 (0.1)	5.6106
VCC836	12:25:46.70	+12:39:44.0	Sab	17	23.5 (0.9)	7.1 (0.1)	2.5965
VCC841	12:25:47.40	+14:57:09.0	BCD	17	20.5 (1.4)	5.4 (0.1)	0.5943
VCC849	12:25:50.70	+10:27:33.0	Sbc	23	19.1 (0.7)	7.0 (0.1)	5.468
VCC851	12:25:54.10	+07:33:17.0	Sc	23	18.9 (0.6)	7.0 (0.1)	2.579
VCC859	12:25:58.30	+03:25:49.0	Sc	17	17.4 (0.6)	7.0 (0.1)	6.1862
VCC873	12:26:07.50	+13:06:46.0	Sc	17	21.0 (0.6)	7.4 (0.1)	2.1181
VCC888	12:26:18.50	+08:20:59.0	Im (Im/S)	23	13.8 (2.8)	6.2 (0.5)	6.5656
VCC905	12:26:30.10	+08:52:20.0	Sc	23	17.5 (0.7)	6.9 (0.1)	3.1603
VCC912	12:26:32.20	+12:36:40.0	Sbc	17	19.7 (0.6)	6.8 (0.1)	0.5869
VCC921	12:26:36.10	+03:57:53.0	Sbc	17	23.9 (0.8)	6.6 (0.1)	1.5483
VCC938	12:26:46.70	+07:55:08.0	Sc	17	20.4 (0.6)	6.7 (0.1)	1.4266
VCC979	12:27:11.60	+09:25:14.0	Sa	23	24.5 (0.9)	6.8 (0.1)	1.7719
VCC995	12:27:22.20	+10:52:00.0	Sc	17	14.9 (1.2)	6.0 (0.2)	2.0003
VCC1002	12:27:26.40	+06:15:46.0	Sc	23	19.6 (0.6)	7.2 (0.1)	0.9396
VCC1030	12:27:40.50	+13:04:44.0	S0	17	23.9 (0.9)	6.4 (0.1)	0.9699
VCC1043	12:27:45.60	+13:00:32.0	Sb	17	20.5 (0.6)	7.2 (0.1)	0.9814
VCC1048	12:27:55.40	+05:43:16.0	Scd	23	19.4 (0.8)	6.5 (0.1)	2.495
VCC1086	12:28:15.90	+09:26:11.0	S (dS)	23	19.0 (0.5)	6.8 (0.1)	4.3639
VCC1091	12:28:18.80	+08:43:46.0	Sbc	23	19.3 (0.7)	6.5 (0.1)	4.2775
VCC1118	12:28:40.50	+09:15:32.0	Sc	23	23.0 (0.8)	6.8 (0.1)	1.0827
VCC1154	12:29:00.00	+13:58:43.0	S0	17	25.9 (0.9)	6.3 (0.1)	3.1325
VCC1189	12:29:28.80	+06:46:18.0	Sc	17	17.0 (0.6)	6.5 (0.1)	1.0915
VCC1190	12:29:28.00	+08:45:00.0	Sa	23	21.9 (0.7)	6.8 (0.1)	1.9899
VCC1193	12:29:30.60	+07:41:48.0	Sc	17	18.6 (0.8)	6.4 (0.1)	6.9848
VCC1200	12:29:35.20	+10:47:35.0	Im (Im/S)	17	13.5 (0.8)	5.8 (0.2)	0.9605
VCC1205	12:29:37.80	+07:49:27.0	Sc	17	22.2 (0.8)	6.6 (0.1)	0.7719
VCC1250	12:29:59.10	+12:20:55.0	S0	17	23.5 (0.9)	6.0 (0.1)	0.9502
VCC1253	12:30:02.20	+13:38:11.0	S0a - S0/Sa	17	25.5 (1.2)	5.7 (0.1)	1.8314
VCC1290	12:30:26.80	+04:14:48.0	Sb	17	19.7 (0.6)	6.9 (0.1)	1.7848

Object	RA	dec	Type	Distance (Mpc)	T (K)	$\log(M_D/M_\odot)$	$\chi^2_{dof=3}$
VCC1326	12:30:57.10	+11:29:01.0	Sa	17	26.4 (1.4)	6.0 (0.1)	1.0426
VCC1330	12:30:59.70	+08:04:41.0	Sa	17	18.4 (0.6)	6.6 (0.1)	1.1004
VCC1356	12:31:22.90	+11:29:33.0	Sm/BCD	17	18.1 (1.7)	5.6 (0.2)	1.8336
VCC1374	12:31:38.00	+14:51:24.0	Im/BCD	17	18.1 (1.0)	5.9 (0.1)	3.009
VCC1401	12:31:59.20	+14:25:14.0	Sbc	17	21.3 (0.6)	8.0 (0.1)	2.1846
VCC1419	12:32:10.50	+13:25:11.0	S (dS)	17	18.5 (0.8)	6.1 (0.1)	0.7018
VCC1437	12:32:33.50	+09:10:25.0	BCD	17	25.3 (1.4)	5.4 (0.1)	1.4448
VCC1450	12:32:41.70	+14:03:06.0	Sc	17	19.4 (0.7)	6.8 (0.1)	4.0079
VCC1486	12:33:10.00	+11:20:51.0	S (dS)	17	19.5 (1.0)	5.8 (0.1)	2.7726
VCC1508	12:33:30.30	+08:39:16.0	Sc	17	20.2 (0.8)	7.1 (0.1)	4.2483
VCC1516	12:33:39.70	+09:10:30.0	Sbc	17	19.7 (0.7)	6.9 (0.1)	3.9513
VCC1535	12:34:03.00	+07:41:57.0	S0	17	23.8 (0.8)	7.0 (0.1)	1.6852
VCC1552	12:34:15.80	+13:04:32.0	Sa	17	19.3 (0.6)	6.6 (0.1)	5.1485
VCC1555	12:34:20.30	+08:11:52.0	Sc	17	19.8 (0.6)	7.9 (0.1)	0.679
VCC1566	12:34:30.70	+09:09:17.0	Sd	17	14.9 (1.0)	6.2 (0.2)	3.506
VCC1575	12:34:39.50	+07:09:37.0	Sm	17	20.8 (0.7)	6.5 (0.1)	0.5833
VCC1673	12:36:32.70	+11:15:29.0	Sc	17	21.5 (0.9)	7.3 (0.1)	3.9681
VCC1676	12:36:34.20	+11:14:20.0	Sc	17	23.1 (0.9)	7.6 (0.1)	5.0486
VCC1686	12:36:43.50	+13:15:34.0	Sm	17	17.2 (0.6)	6.7 (0.1)	4.2347
VCC1690	12:36:49.80	+13:09:46.0	Sab	17	21.2 (0.6)	7.6 (0.1)	4.488
VCC1727	12:37:43.50	+11:49:05.0	Sab	17	20.5 (0.6)	7.6 (0.1)	2.2168
VCC1758	12:38:21.00	+07:53:31.0	Sc	17	16.3 (0.7)	6.4 (0.1)	2.6176
VCC1791	12:39:25.00	+07:57:57.0	Sm/BCD	17	17.4 (1.0)	6.1 (0.1)	1.8751

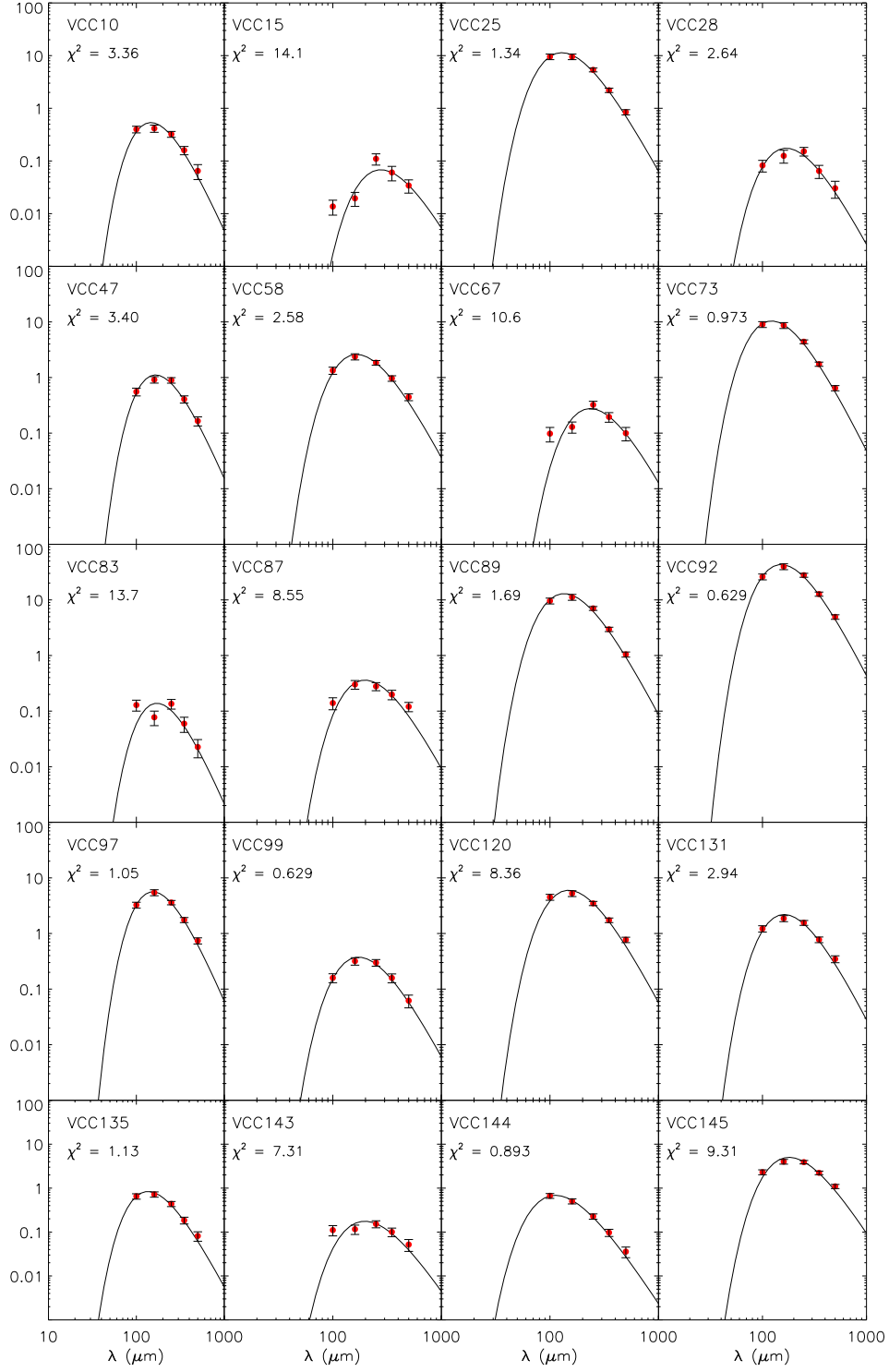
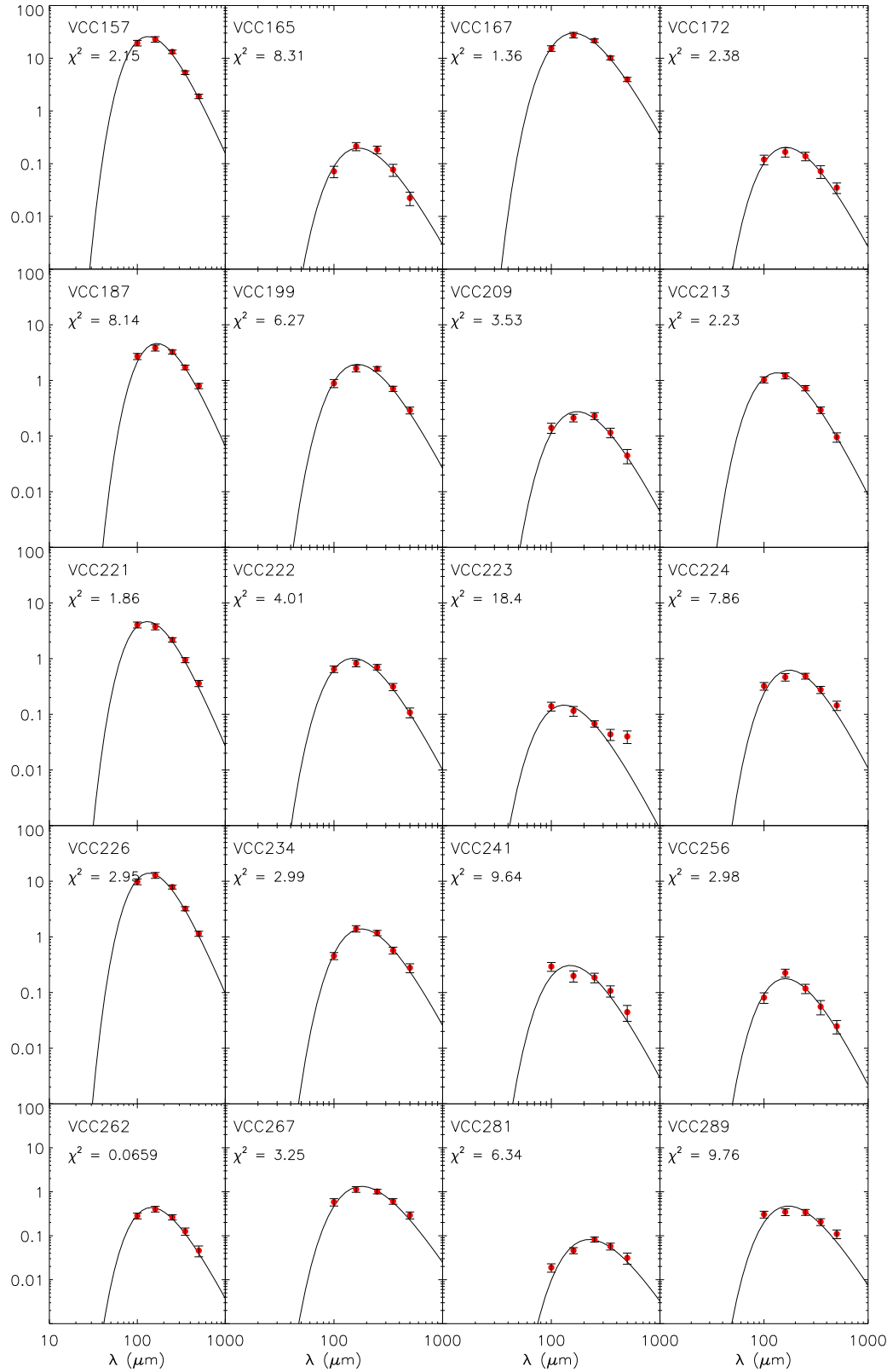


Figure D1. FIR SED plots for the VCC galaxies with 5-band FIR detections. Also shown are the single-temperature modified blackbody fits (solid black line).

APPENDIX D: FIR SED PLOTS WITH SINGLE-TEMPERATURE MODIFIED BLACKBODY FITS

**Figure D1** – *continued* FIR SED plots with single-temperature modified blackbody fits

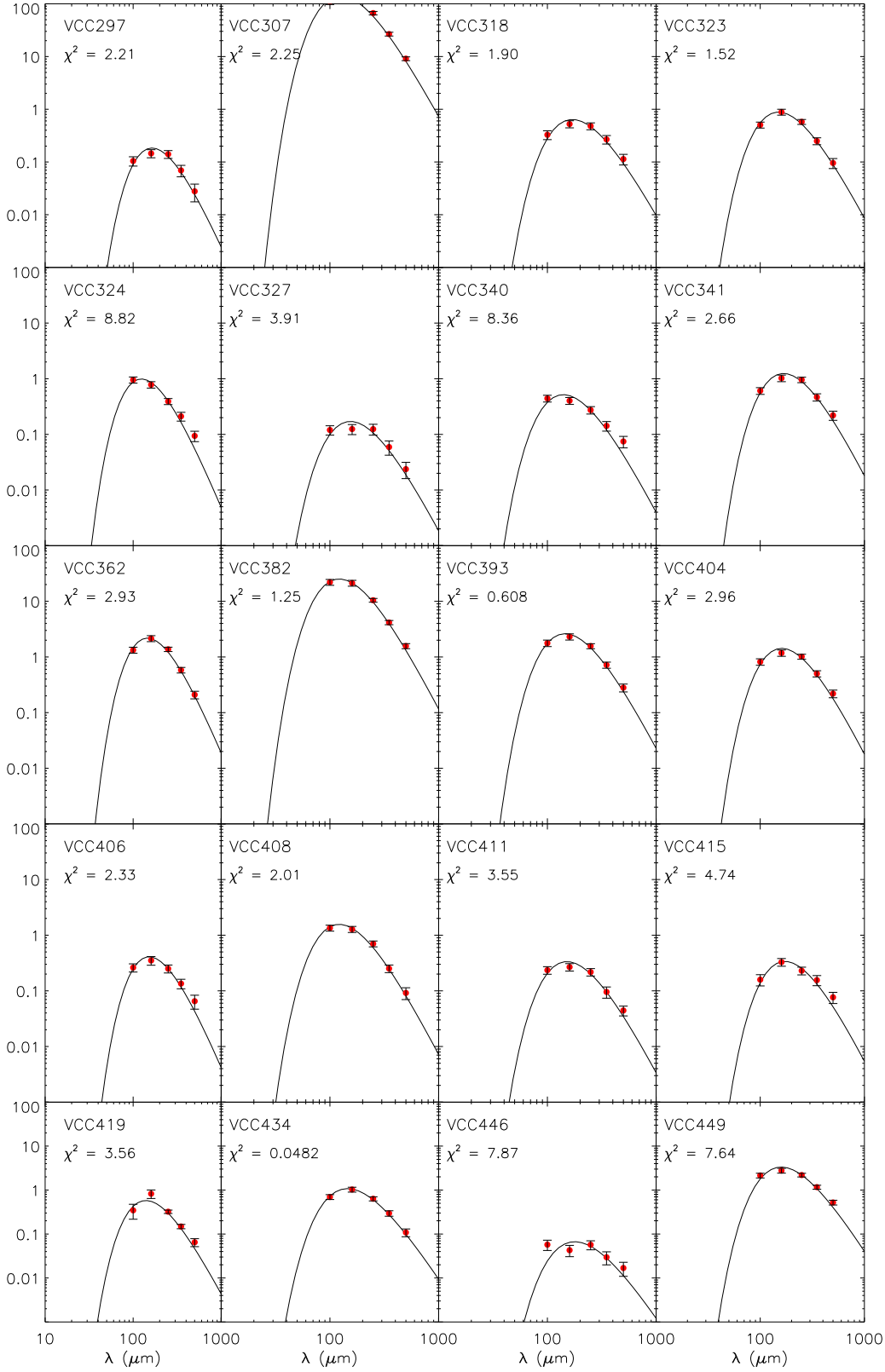


Figure D1 – *continued* FIR SED plots with single-temperature modified blackbody fits

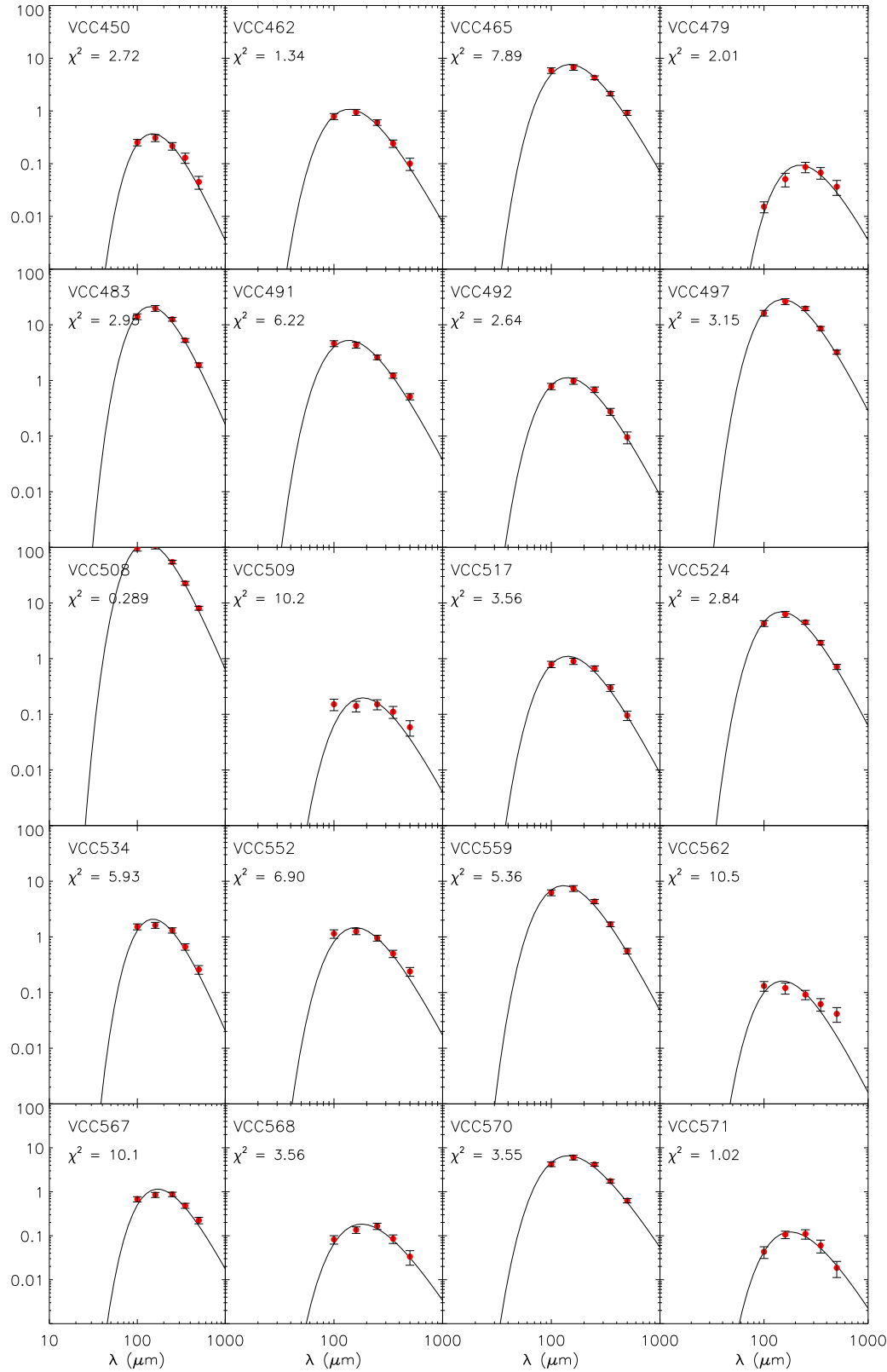


Figure D1 – *continued* FIR SED plots with single-temperature modified blackbody fits

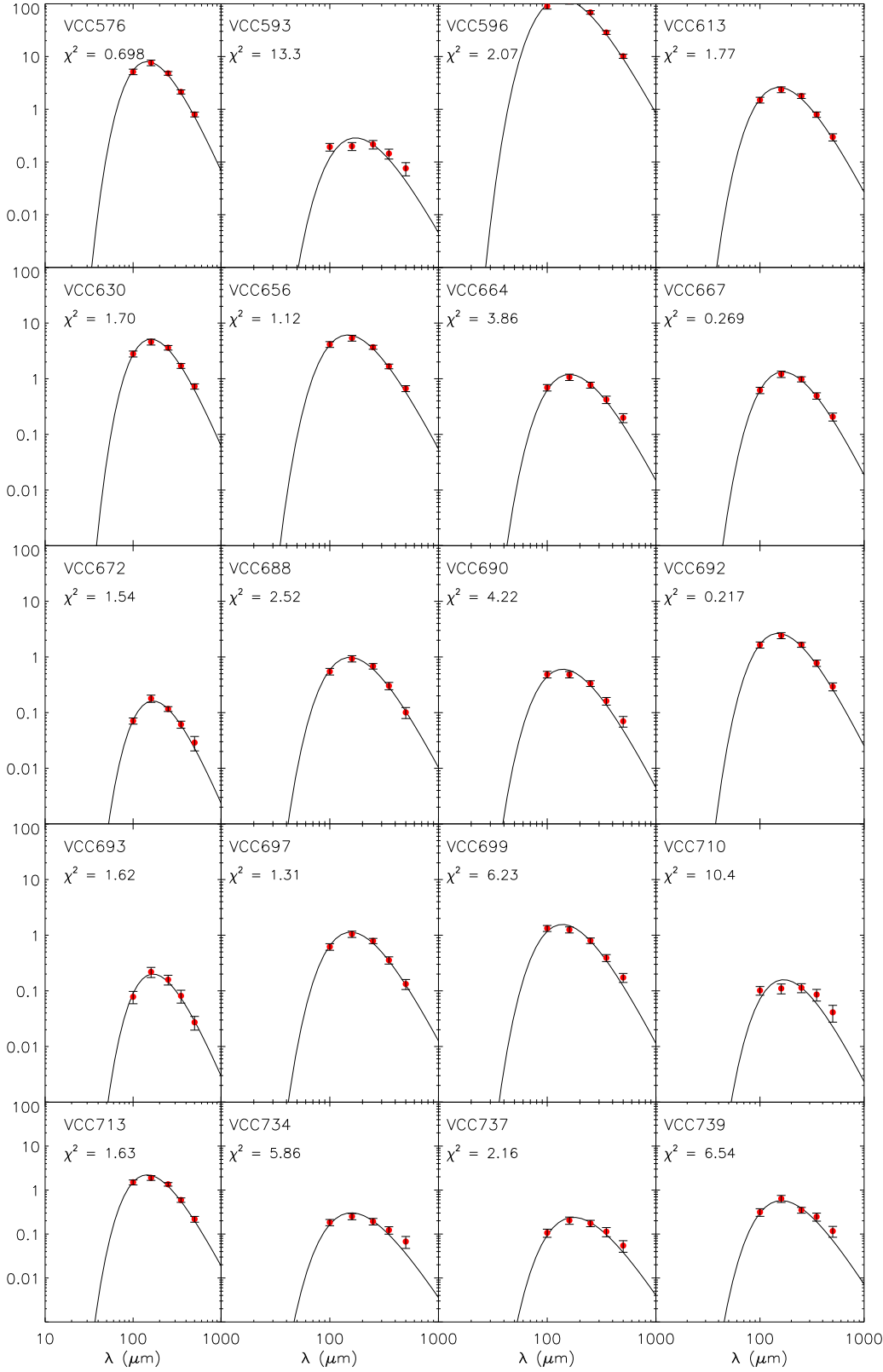
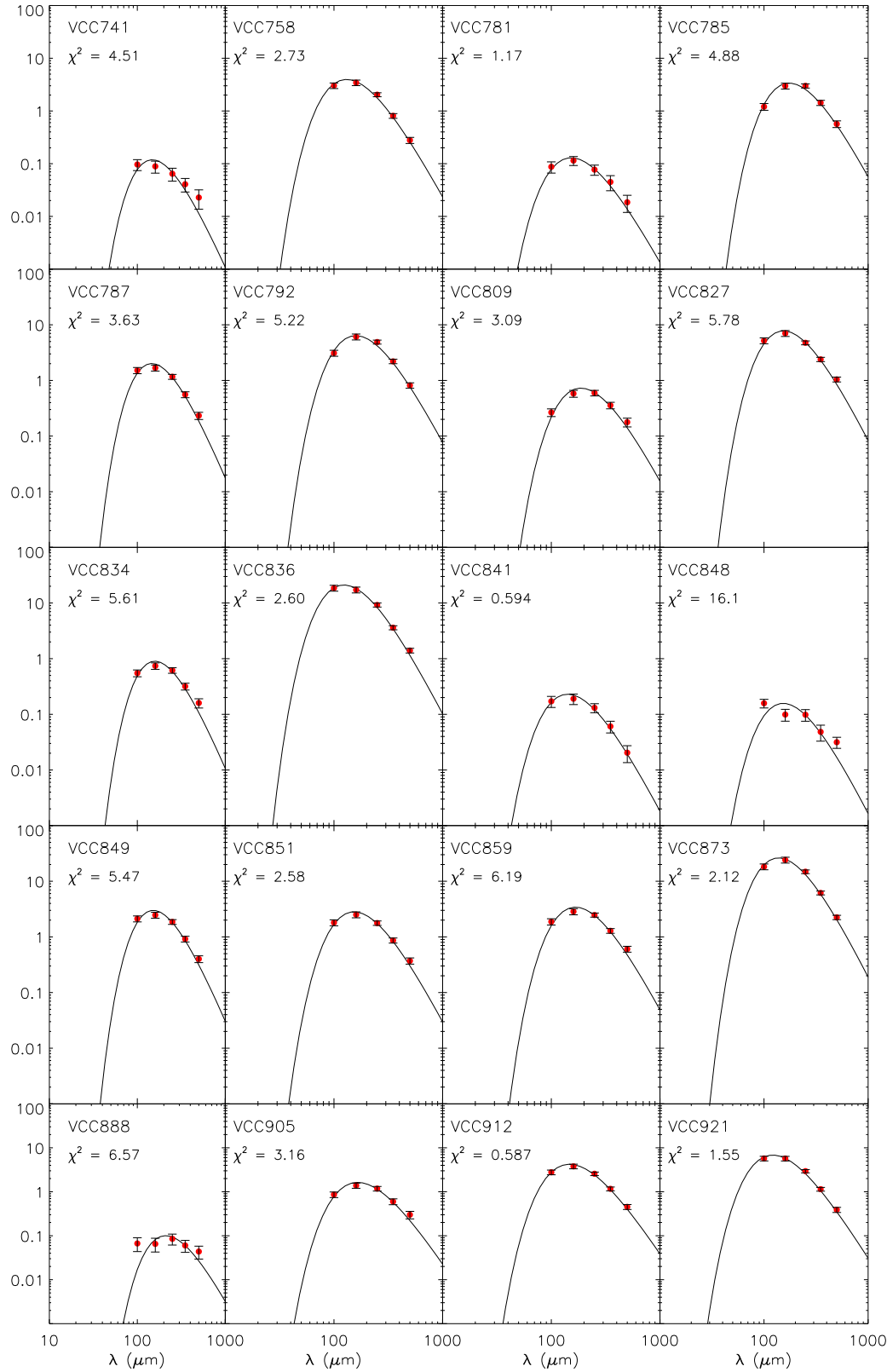


Figure D1 – *continued* FIR SED plots with single-temperature modified blackbody fits

**Figure D1** – *continued* FIR SED plots with single-temperature modified blackbody fits

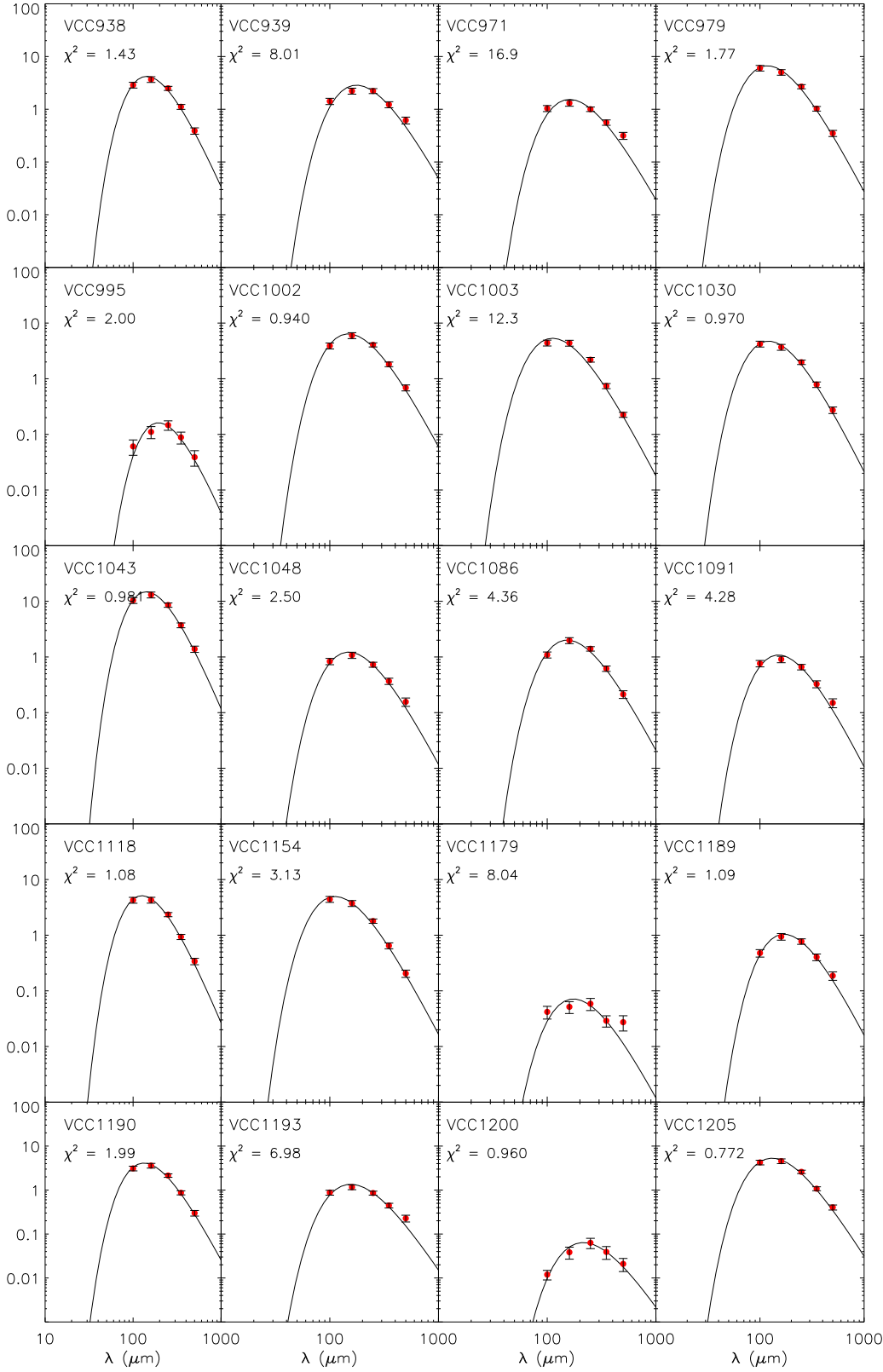


Figure D1 – *continued* FIR SED plots with single-temperature modified blackbody fits

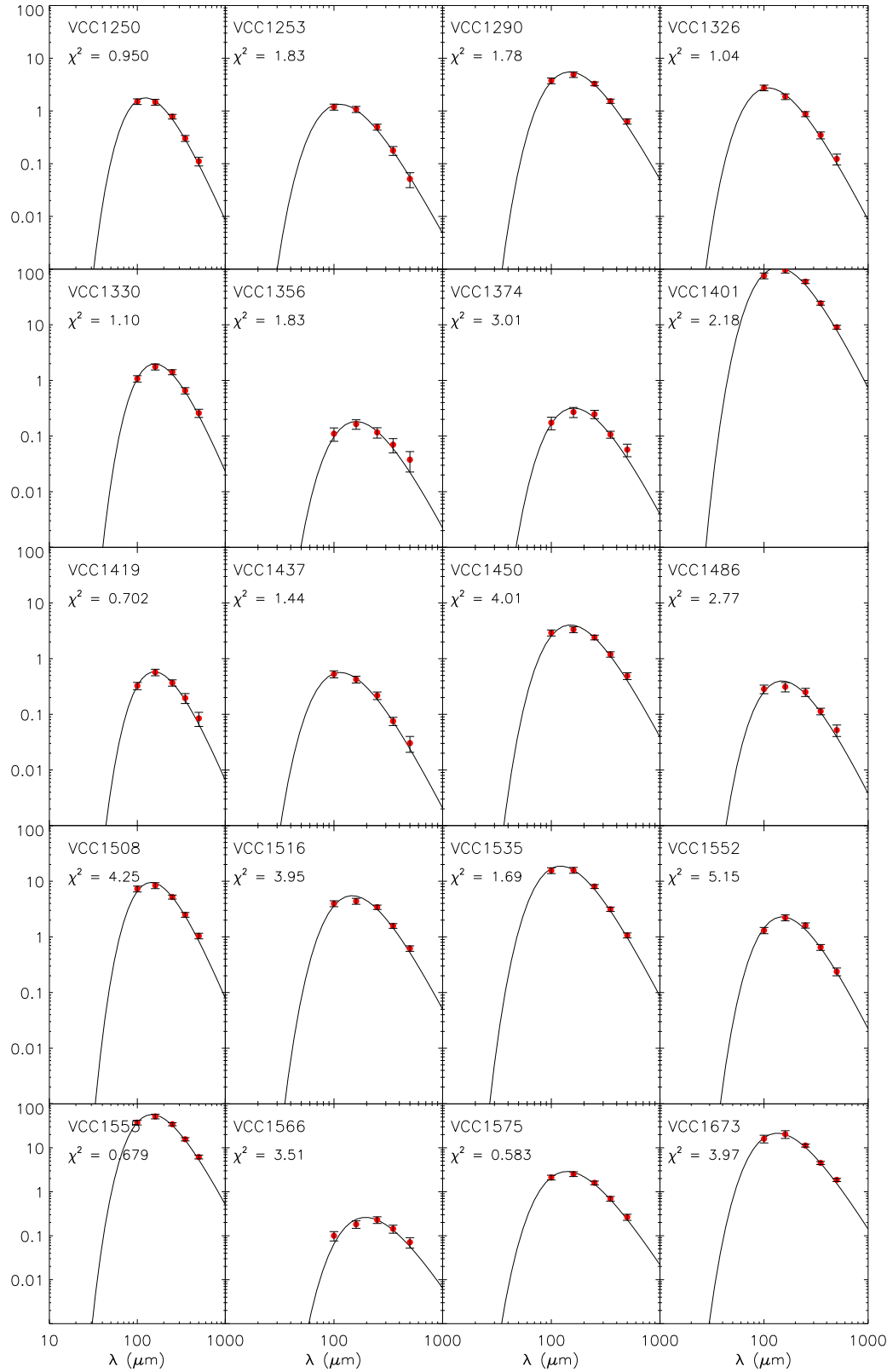


Figure D1 – *continued* FIR SED plots with single-temperature modified blackbody fits

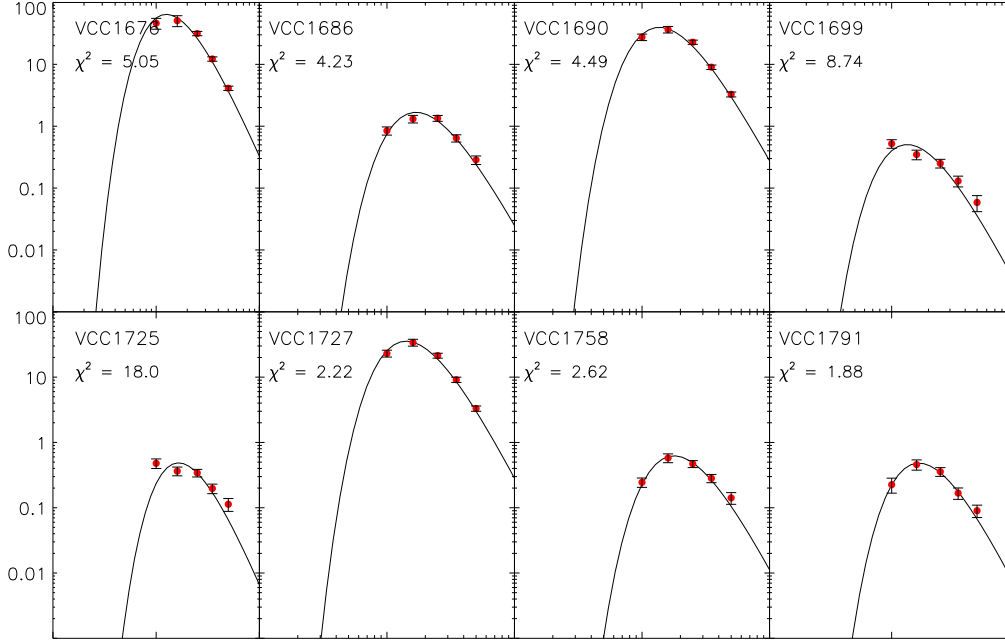


Figure D1 – *continued* FIR SED plots with single-temperature modified blackbody fits